

Frequency reconfigurable impedance matching networks
based on LTCC, fluidic and MEMS technologies for agile RF
amplifiers

by

Dorra BAHLOUL

THESIS PRESENTED TO ÉCOLE DE TECHNOLOGIE SUPÉRIEURE
IN PARTIAL FULFILLMENT FOR THE DEGREE OF
DOCTOR PHILOSOPHY
Ph. D.

MONTREAL, FEBRUARY 14, 2022

ÉCOLE DE TECHNOLOGIE SUPÉRIEURE
UNIVERSITÉ DU QUÉBEC

© Copyright reserved

It is forbidden to reproduce, save or share the content of this document either in whole or in parts. The reader who wishes to print or save this document on any media must first get the permission of the author.

BOARD OF EXAMINERS
THIS THESIS HAS BEEN EVALUATED
BY THE FOLLOWING BOARD OF EXAMINERS

Mr. Ammar Kouki, Thesis Supervisor
Department of Electrical Engineering, École de technologie supérieure

Mr. James Lapalme, President of the Board of Examiners
Department of Software and IT Engineering, École de technologie supérieure

Mr. Nicolas Constantin, Member of the jury
Department of Electrical Engineering, École de technologie supérieure

Mr. Ke Wu, External Evaluator
Department of Electrical Engineering, École Polytechnique Montreal

THIS THESIS WAS PRESENTED AND DEFENDED
IN THE PRESENCE OF A BOARD OF EXAMINERS AND PUBLIC
JANUARY 13, 2022
AT ÉCOLE DE TECHNOLOGIE SUPÉRIEURE

ACKNOWLEDGMENT

First and foremost, I wish to express my gratitude to my supervisor Professor Ammar Kouki for providing me the opportunity to accomplish this research project. He offers me invaluable assistance, appropriate support and precious advice. His wide knowledge and logical way of thinking have been of great value for me.

Besides, I would like to thank my PhD committee members: Professor James Lapalme, Professor Nicolas Constantin and Professor Ke Wu, for accepting evaluating my work and providing me with their valuable feedbacks.

Next, my thanks and appreciations go to our technical staff, particularly Normand Gravel, Alexandre Robichaud, André Zalzal, Christian Talbot, Youssef Bekbouti and Rigoberto Avelar for their help in the fabrication and measurement of my circuits. They assisted me in the use of different machines and equipment.

I'm grateful to all my colleagues in ÉTS: Madiha, Sana, Hana, Ines, Khawla, Maria, Taher, Riadh, Ahmed, Achraf, Chokri, Muzzammel, Mohamed Amine, Aref, Aria, Mohsen and Cina, for the happy and hard time we shared. Their friendly and technical discussions were valuable for me.

Last but not least, I would like to thank my father Samir, my mother Noura, my sister Marwa and my brothers Bilel and Mohamed Aziz for their faithful encouragement, unceasing support and unconditional help. I acknowledge the role of my husband Ismail for his love, patience and understanding. I apologize to my little daughter Yasmine for being busy in her first months. I'm also grateful to my friends and sisters Nesrine and Fatma for their continuous support and precious assistance.

Réseaux d'adaptation d'impédance reconfigurables en fréquence basés sur les technologies LTCC, fluidic et MEMS pour les amplificateurs RF agiles

Dorra BAHLOUL

RÉSUMÉ

De nouveaux réseaux d'adaptation (RA) d'impédance reconfigurables en fréquence, ou syntoniseurs, qui peuvent être utilisés pour réaliser divers dispositifs RF programmables, tels que des amplificateurs, sont proposés. En promouvant la reconfigurabilité des dispositifs RF, les RA proposés permettent de réduire considérablement le nombre de composants dans une chaîne RF multi-standard et de maximiser la réutilisation du matériel. Les technologies fluidiques et MEMS (MicroElectroMechanical Systems) sont envisagées pour concevoir des RA couvrant différentes bandes de fréquences. Dans les deux cas, la technologie LTCC (Low Temperature Co-fired Ceramics) est utilisée comme substrat 3D à faible perte dans la réalisation de ces RA pour offrir, simultanément, une miniaturisation supplémentaire, un niveau d'intégration élevé et des solutions d'emballage à faible coût.

D'abord, l'architecture et le principe de fonctionnement des RA d'impédance RF proposés, qui sont communs aux solutions fluidiques et MEMS, sont présentés et discutés. L'architecture sélectionnée est basée sur une cascade de huit cellules à 2 états, où les paramètres électriques de chaque cellule alternent entre deux ensembles de valeurs en passant d'un état à l'autre. Dans l'approche fluidique, les cellules sont constituées de cavités formées sur un guide d'onde coplanaire et les deux états correspondent aux scénarios où la cavité est vide ou est remplie d'eau déionisée (DI). Dans l'approche MEMS, les cellules sont des commutateurs capacitifs, et les positions des commutateurs haut et bas fournissant les deux états souhaités. La conception des cellules individuelles et de l'ensemble du syntoniseur est ensuite faite. Des équations analytiques sont développées et utilisées pour fixer les dimensions initiales des cellules individuelles, c'est-à-dire la cellule fluidique et le commutateur MEMS. Des simulations de champ 3D sont utilisées pour compléter la conception des cellules et de l'ensemble des syntoniseurs. Des approches alternatives de miniaturisation pour le syntoniseur MEMS sont également étudiées. Les résultats de la simulation montrent qu'il est possible d'obtenir une bonne couverture de l'abaque de Smith avec le syntoniseur fluidique pour les fréquences comprises entre 0,8 GHz et 2,4 GHz avec un tuner mesurant 26 mm × 10 mm × 1,5 mm, tandis que le syntoniseur MEMS offre une couverture comparable pour les fréquences entre 2 GHz et 7 GHz avec un tuner miniaturisé jusqu'à 5,51 mm × 2,54 mm × 1,19 mm.

Ensuite, la fabrication et les tests des cellules et des syntoniseurs conçus sont entrepris. Pour les cellules et le syntoniseur fluidiques, le processus LTCC standard est adéquat pour le prototypage et a été utilisé pour fabriquer et tester plusieurs cellules et syntoniseurs. Un bon accord entre les simulations et les mesures est observé pour les cellules individuelles et l'ensemble du syntoniseur, confirmant la couverture prédite. Pour la solution MEMS, un nouveau procédé MEMS-on-LTCC, nécessaire à la fabrication du syntoniseur MEMS est

d'abord développé pour prendre en compte les spécificités du substrat LTCC. Des détails sur toutes les étapes de processus nécessaires pour construire un commutateur capacitif sur LTCC sont élaborés. Les défis rencontrés sont mis en évidence et des moyens de les contourner sont proposés. Comme application, des amplificateurs RF reconfigurables utilisant les RA fluidiques et MEMS développés sont conçus. Ils montrent un gain variant autour le gain maximum disponible à différents points dans les bandes de fréquences d'intérêt, c'est-à-dire [0,9 GHz-2,4 GHz] et [2 GHz-7 GHz] pour les architectures fluide et MEMS respectivement.

Enfin, des perspectives pour améliorer les performances des syntoniseurs d'impédances sont discutées. D'une part, l'introduction de lignes de transmission remplies d'air permet de réduire les pertes diélectriques dans le syntoniseur MEMS-sur-LTCC. Aussi, utiliser du métal liquide à la place de l'eau DI dans le syntoniseur fluide permet d'éliminer les problèmes des pertes diélectriques et d'offrir une reconfigurabilité à des fréquences plus élevées. D'autre part, des modules de commande et d'activation automatiques de ces réseaux d'adaptation d'impédances reconfigurables sont également proposés.

Mots-clés: cavités, eau dé-ionisée, fluide, réseau d'adaptation d'impédance reconfigurables, LTCC, MEMS, MEMS-sur-LTCC, amplificateur RF, commutateurs RF, lignes de transmission.

Frequency reconfigurable impedance matching networks based on LTCC, fluidic and MEMS technologies for agile RF amplifiers

Dorra BAHLOUL

ABSTRACT

New frequency reconfigurable impedance matching networks (MNs), or tuners, which can be used to realize various field programmable RF devices, such as amplifiers, are proposed. By enabling field programmability of RF devices, the proposed MNs make it possible to reduce considerably the component count in a multi-standard RF chain and to maximize hardware re-use. Both fluidic and MEMS (MicroElectroMechanical Systems) technologies are considered for designing alternative MNs covering different frequency bands. In both cases, Low Temperature Co-fired Ceramics (LTCC) technology is used as a low-loss 3D substrate in the MN realization in order to simultaneously achieve miniaturization, high integration levels and low-cost packaging solutions.

First, the architecture and operation principle of the proposed RF impedance MNs, which are common to both fluidic and MEMS solutions, are introduced and discussed. The selected architecture is based on eight cascaded 2-state cells where each cell's electric parameters alternate between two sets of values from one state to the other. In the fluidic approach, the cells are made of cavities over a coplanar waveguide and the two states correspond to when the cavity is empty and when the cavity is filled with deionized (DI) water. In the MEMS approach the cells are made of capacitive switches, with the up and down switch positions providing the two desired states. The design of the individual cells and entire cascaded tuner are then undertaken. Analytical equations are developed and used to establish the initial dimensions of the individual cells, i.e., the fluidic cell and the MEMS switch and 3D field simulations are used to complete the design of the cells and the entire tuners. Alternative miniaturization approaches for the MEMS-based tuner are also investigated. Simulation results show that it is possible to achieve good Smith chart coverage with the fluidic tuner for frequencies between 0.8 GHz and 2.4 GHz with a tuner that measures $26 \text{ mm} \times 10 \text{ mm} \times 1.5 \text{ mm}$, while the MEMS-based tuner provides comparable coverage for frequencies between 2 GHz and 7 GHz with a tuner that can be miniaturized down to $5.51 \text{ mm} \times 2.54 \text{ mm} \times 1.19 \text{ mm}$.

Second, the fabrication and testing of the designed cells and tuners is undertaken. For the fluidic cells and tuner, the standard LTCC process is adequate for prototyping and has been used to fabricate and test multiple cells and tuners. Good agreement between simulations and measurements are observed for the individual cells and the entire tuner, confirming the predicted coverage. For MEMS solution, a new MEMS-on-LTCC process, necessary for fabricating the MEMS-based tuner is first developed to take into account the specificities of the LTCC substrate. Details about all process steps needed to build a capacitive switch on LTCC are elaborated. The encountered challenges are highlighted and some means to circumvent them are proposed. As an application, reconfigurable RF amplifiers using the developed fluidic and MEMS MNs are built. They show a gain varying around the maximum

available gain at different points in the frequency bands of interest, i.e. [0.9GHz- 2.4 GHz] and [2 GHz- 7GHz] for the fluidic and MEMS based architectures respectively.

Finally, perspectives for enhanced RF tuners are discussed. Introducing air- filled transmission lines in the MEMS based tuner as a way to reduce dielectric losses may improve the overall performances. Employing liquid metal instead of DI-water in fluidic tuner allows removing concerns about dielectric losses and enabling reconfigurability at higher frequencies. Modules for tuners' automatic control and activation are also proposed.

Keywords: cavities, deionized water, fluidics, impedance tuners, LTCC, MEMS, MEMS-on-LTCC, reconfigurable RF matching networks, RF amplifier, switches, transmission lines.

TABLE OF CONTENTS

| | Page |
|--|------|
| INTRODUCTION | 1 |
| CHAPTER 1 LITERATURE REVIEW | 7 |
| 1.1 Introduction..... | 7 |
| 1.2 Frequency reconfigurable RF amplifier architectures | 7 |
| 1.2.1 Unit selection amplifiers..... | 8 |
| 1.2.2 Broadband amplifiers..... | 9 |
| 1.2.3 Variable impedance-matching amplifiers..... | 9 |
| 1.2.4 Frequency reconfigurable RF amplifiers summary | 14 |
| 1.3 Frequency reconfigurable impedance-matching networks | 14 |
| 1.3.1 Semiconductor reconfigurable matching networks | 15 |
| 1.3.2 Ferroelectric reconfigurable matching networks | 17 |
| 1.3.3 MEMS reconfigurable matching networks..... | 18 |
| 1.3.4 Fluidics reconfigurable matching networks..... | 22 |
| 1.3.5 Frequency reconfigurable matching networks summary | 24 |
| 1.4 MEMS-on-LTCC substrate..... | 25 |
| 1.4.1 Laser micro-machined MEMS process..... | 26 |
| 1.4.2 Surface micromachining MEMS process | 26 |
| 1.4.3 MEMS-on-LTCC summary | 29 |
| 1.5 Low loss RF transmission lines | 30 |
| 1.5.1 Waveguides..... | 31 |
| 1.5.2 Substrate Integrated Waveguides (SIW)..... | 31 |
| 1.5.3 Air-filled planar transmission lines..... | 32 |
| 1.5.4 Low loss RF transmission lines summary | 34 |
| 1.6 Conclusion | 35 |
| CHAPTER 2 LTCC FABRICATION TECHNOLOGY | 37 |
| 2.1 Introduction..... | 37 |
| 2.2 LTCC technology description..... | 37 |
| 2.2.1 Overview..... | 37 |
| 2.2.2 LACIME in-house LTCC process | 38 |
| 2.2.3 LTCC technology benefits..... | 39 |
| 2.2.4 LTCC technology limitations | 40 |
| 2.3 LTCC for reconfigurable RF components | 41 |
| 2.3.1 LTCC for fluidic reconfigurable RF components..... | 41 |
| 2.3.2 LTCC for MEMS reconfigurable RF components | 42 |
| 2.3.3 Fluidic and MEMS tuners and RF amplifiers in LTCC technology..... | 44 |
| 2.4 Conclusion | 45 |
| CHAPTER 3 FLUIDIC AND MEMS RECONFIGURABLE RF IMPEDANCE TUNERS' DESIGN | 47 |

| | | |
|---|--|-----|
| 3.1 | Introduction..... | 47 |
| 3.2 | Impedance tuners' design approach..... | 47 |
| 3.3 | LTCC based fluidic tuner..... | 51 |
| 3.3.1 | Fluidic RF cell design..... | 51 |
| 3.3.2 | Fluidic tuner..... | 57 |
| 3.4 | MEMS-on-LTCC tuner..... | 61 |
| 3.4.1 | MEMS-on-LTCC RF switch..... | 61 |
| 3.4.2 | MEMS-on-LTCC planar tuner..... | 66 |
| 3.4.3 | MEMS-on-LTCC 3D tuner..... | 70 |
| 3.5 | Comparison of fluidic and MEMS-on-LTCC tuners..... | 76 |
| 3.6 | Conclusion..... | 77 |
| CHAPTER 4 MEMS-ON-LTCC PROCESS..... | | 79 |
| 4.1 | Introduction..... | 79 |
| 4.2 | MEMS-on-LTCC process development..... | 79 |
| 4.2.1 | Process flow overview..... | 79 |
| 4.2.2 | Fabrication challenges and considerations..... | 82 |
| 4.3 | Application: Capacitive RF MEMS-on-LTCC switch..... | 90 |
| 4.3.1 | Electromechanical analysis..... | 90 |
| 4.3.2 | RF MEMS-on-LTCC switch fabrication..... | 97 |
| 4.4 | Conclusion..... | 99 |
| CHAPTER 5 EXPERIMENTAL RESULTS AND APPLICATIONS..... | | 101 |
| 5.1 | Introduction..... | 101 |
| 5.2 | Fabrication and measurements..... | 101 |
| 5.2.1 | Measurement setups..... | 101 |
| 5.2.2 | Fluidic circuits..... | 103 |
| 5.3 | Application: frequency reconfigurable RF amplifiers..... | 108 |
| 5.3.1 | Reconfigurable fluidic RF amplifier..... | 108 |
| 5.3.2 | Reconfigurable MEMS-on-LTCC RF amplifier..... | 113 |
| 5.4 | Conclusion..... | 116 |
| CHAPTER 6 PERSPECTIVES FOR ENHANCED PERFORMANCE RF TUNERS..... | | 119 |
| 6.1 | Introduction..... | 119 |
| 6.2 | Air-filled 3D MEMS-on-LTCC tuner..... | 119 |
| 6.2.1 | Air-filled stripline design..... | 120 |
| 6.2.2 | Air-filled MEMS-on-LTCC 3D tuner..... | 124 |
| 6.3 | LTCC based liquid metal RF tuner..... | 129 |
| 6.3.1 | Liquid metal choice..... | 129 |
| 6.3.2 | Liquid metal RF cell..... | 130 |
| 6.3.3 | Liquid metal RF tuner..... | 131 |
| 6.4 | LTCC based RF tuners adaptive control..... | 133 |
| 6.4.1 | Sensing module..... | 134 |
| 6.4.2 | Control modules..... | 134 |
| 6.5 | Conclusion..... | 136 |

CONCLUSION AND RECOMMANDATIONS139

JOURNAL AND CONFERENCES ARTICLES143

APPENDIX I ADS SCHEMATIC FOR RF TUNERS SIMULATIONS145

APPENDIX II MEMS-ON-LTCC PROCESS149

APPENDIX III COMSOL SETUP.....153

BIBLIOGRAPHY155

LIST OF TABLES

| | | Page |
|-----------|--|------|
| Table 1.1 | Comparison of reconfigurable matching networks technologies..... | 25 |
| Table 1.2 | MEMS-on-LTCC process summary | 30 |
| Table 1.3 | RF guiding structures summary | 35 |
| Table 3.1 | DuPont 951 characteristics | 54 |
| Table 3.2 | CPWG sections initial dimensions..... | 55 |
| Table 3.3 | Characteristics for S3 when empty and filled with DI water | 55 |
| Table 3.4 | RF MEMS-on-LTCC switch initial dimensions | 65 |
| Table 3.5 | MEMS-on-LTCC switch electrical parameters | 65 |
| Table 3.6 | Vertical transitions geometrical dimensions | 71 |
| Table 3.7 | Stripline geometrical features | 72 |
| Table 3.8 | RF tuner's comparison..... | 76 |
| Table 4.1 | Stress on MEMS-on-LTCC membrane | 88 |
| Table 4.2 | Stress on MEMS-on-LTCC membrane (continued)..... | 89 |
| Table 4.3 | RF MEMS-on-LTCC switch mechanical characteristics | 93 |
| Table 5.1 | Optimal source impedances and tuner's selected impedances | 110 |
| Table 5.2 | Optimal source, load and MEMS-on-LTCC tuner's selected impedances | 115 |
| Table 6.1 | Air-filled and dielectric-filled stripline parameters | 121 |

LIST OF FIGURES

| | | Page |
|-------------|--|------|
| Figure 0.1 | Classical multi-standards transmitter with parallel RF chains..... | 1 |
| Figure 0.2 | Multi-standard RF transceiver implemented: a) in parallel RF chains architecture and b) based on reconfigurable RF components..... | 2 |
| Figure 1.1 | Unit selection type multi-band amplifier | 8 |
| Figure 1.2 | Broadband matching type amplifier..... | 9 |
| Figure 1.3 | Variable matching type amplifier | 10 |
| Figure 1.4 | 900MHz/ 1900 MHz dual band amplifier..... | 10 |
| Figure 1.5 | 900MHz/ 1900 MHz power amplifier performance | 11 |
| Figure 1.6 | Tri-band power amplifier simplified circuit | 12 |
| Figure 1.7 | Tri-band power amplifier measured performances a) Gain, and b) Output power, power added efficiency and drain efficiency..... | 12 |
| Figure 1.8 | Tunable power amplifier scheme..... | 13 |
| Figure 1.9 | Tunable power amplifier performance a) Gain and b) Reflection coefficient | 13 |
| Figure 1.10 | PIN diodes automatic matching system: a) equivalent circuit, b) tunable capacitor replacement structure and c) fabricated prototype | 15 |
| Figure 1.11 | PIN diodes automatic matching system: a) simulated coverage and b) measured coverage | 16 |
| Figure 1.12 | Varactor diodes based variable matching network | 16 |
| Figure 1.13 | Varactor diodes based variable matching network simulated coverage | 17 |
| Figure 1.14 | Ferroelectric varactors based variable matching network: a) equivalent circuit, and b) fabricated circuit | 17 |
| Figure 1.15 | Ferroelectric varactors based variable matching network: a) simulated coverage and b) measured coverage..... | 18 |
| Figure 1.16 | Double stub variable matching network based on MEMS switches..... | 19 |

| | | |
|-------------|--|----|
| Figure 1.17 | Double stub variable matching network simulated (o) and measured (x) coverage at: a) 20 GHz, b) 15 GHz and c) 10 GHz | 19 |
| Figure 1.18 | Triple stub loaded with MEMS switches tuner: a) equivalent circuit and b) fabricated circuit | 20 |
| Figure 1.19 | Triple stub loaded with MEMS switches tuner impedance coverage..... | 21 |
| Figure 1.20 | SW-DMTL tuner..... | 21 |
| Figure 1.21 | SW-DMTL tuner coverage | 22 |
| Figure 1.22 | Liquid-metal double stub tuner | 23 |
| Figure 1.23 | Liquid-metal double stub tuner coverage at 3.725 GHz | 23 |
| Figure 1.24 | Fluidic dielectric double stub tuner..... | 24 |
| Figure 1.25 | MEMS on LTCC based on laser bending | 26 |
| Figure 1.26 | Capacitive MEMS on LTCC process | 27 |
| Figure 1.27 | Capacitive MEMS on high-k LTCC substrate..... | 28 |
| Figure 1.28 | Ohmic MEMS on LTCC: a) SPST switch and b) SPDT switch..... | 29 |
| Figure 1.29 | Empty LTCC SIW | 32 |
| Figure 1.30 | Empty LTCC SIW simulated and measured S parameters..... | 32 |
| Figure 1.31 | Micro-machined air gap: a) stripline and b) rectangular coaxial line..... | 33 |
| Figure 1.32 | Performance of the micro-machined air gap: a) stripline and b) rectangular coaxial line..... | 34 |
| Figure 2.1 | Representative scheme of an LTCC substrate | 38 |
| Figure 2.2 | LTCC@ÉTS process flow | 39 |
| Figure 2.3 | Microstrip transmission line with a fluidic channel..... | 41 |
| Figure 2.4 | RF MEMS switch view..... | 43 |
| Figure 2.5 | Exploded 3D view of a reconfigurable RF amplifiers with tunable matching networks realized with: a) fluidic architecture and b) MEMS architecture..... | 45 |

| | | |
|-------------|--|----|
| Figure 3.1 | Impedance tuner operation principle: a) 2-state RF cell illustrative scheme, b) 2-state RF cell illustrative Smith chart coverage, c) two 2-state RF cell illustrative scheme, d) two 2-state RF cell illustrative Smith chart coverage, e) N 2-state RF cell illustrative scheme, f) N 2-state RF cell illustrative Smith chart coverage..... | 49 |
| Figure 3.2 | Two-state RF fluidic cell: a) 3D view, b) cross section view and c) transmission lines model..... | 52 |
| Figure 3.3 | RF fluidic cell simulated: a) Insertion loss and b) reflection coefficient | 56 |
| Figure 3.4 | Fluidic tuner 3D view | 57 |
| Figure 3.5 | Fluidic tuner simulated Smith chart coverage at different frequencies between 0.9 GHz and 2.4 GHz | 59 |
| Figure 3.6 | Fluidic tuner simulated reflection coefficient over the gamma plane at different frequencies between 0.9 GHz and 2.4 GHz | 60 |
| Figure 3.7 | RF MEMS-on-LTCC switch: a) 3D view, b) top view, c) side view and d) model | 62 |
| Figure 3.8 | Field simulation of the MEMS-on-LTCC switch: a) insertion loss and b) reflection coefficient | 66 |
| Figure 3.9 | MEMS-on-LTCC planer tuner 3D view | 67 |
| Figure 3.10 | MEMS-on-LTCC tuner simulated Smith chart coverage at different frequencies between 2 GHz and 7 GHz..... | 68 |
| Figure 3.11 | MEMS-on-LTCC tuner simulated reflection coefficient over the gamma plane at different frequencies between 2 GHz and 7 GHz..... | 69 |
| Figure 3.12 | Vertical transitions: a) Q-coax, b) modified Q-coax and c) CPW | 70 |
| Figure 3.13 | Vertical transitions attenuation's factors | 71 |
| Figure 3.14 | RF MEMS-on-LTCC 3D switch..... | 72 |
| Figure 3.15 | Field simulation of the planar and 3D MEMS-on LTCC switches: a) insertion loss, b) phase shift and c) reflection coefficient | 73 |
| Figure 3.16 | RF MEMS-on-LTCC 3D tuner (1st iteration) | 74 |
| Figure 3.17 | RF MEMS-on-LTCC 3D tuner (2nd iteration)..... | 74 |

| | | |
|-------------|--|-----|
| Figure 3.18 | MEMS-on-LTCC planar and 3D tuners simulated Smith chart coverage at different frequencies between 2 GHz and 7 GHz..... | 75 |
| Figure 4.1 | MEMS-on-LTCC process flow..... | 82 |
| Figure 4.2 | CMP process | 83 |
| Figure 4.3 | LTCC surface roughness: a) without via before polishing, b) without via after polishing, c) with via before polishing and d) with via after polishing..... | 85 |
| Figure 4.4 | RF MEMS switch short circuits due to pinholes | 86 |
| Figure 4.5 | RF MEMS-on-LTCC switch longitudinal view | 90 |
| Figure 4.6 | Simulated pull-in voltage..... | 95 |
| Figure 4.7 | Applied DC voltage | 96 |
| Figure 4.8 | Membrane collapse | 96 |
| Figure 4.9 | RF MEMS switch capacitance..... | 97 |
| Figure 4.10 | MEMS-on-LTCC switch fabrication steps | 98 |
| Figure 4.11 | 3D view of the MEMS-on-LTCC switch central part | 98 |
| Figure 5.1 | Measurement setups: a) PNA-X probe station and b) VNA test bench... | 102 |
| Figure 5.2 | Fabricated fluidic: a) single cell and b) complete tuner..... | 103 |
| Figure 5.3 | Fluidic circuits' fabrication issues: a) cell layer's misalignment (optical microscopy view) and b) tuner vertical transition's misalignment (X-ray view)..... | 104 |
| Figure 5.4 | Fluidic cell measured and simulated: a) Insertion loss and b) reflection coefficient..... | 105 |
| Figure 5.5 | Fluidic tuner measured and simulated impedance coverage..... | 106 |
| Figure 5.6 | Fluidic tuner simulated and measured insertion loss and reflection coefficient when some cells are DI-water filled | 107 |
| Figure 5.7 | Reconfigurable amplifier block diagram | 108 |
| Figure 5.8 | Required impedances in the ATF-58143 transistor: a) input and b) output | 109 |

| | | |
|-------------|---|-----|
| Figure 5.9 | Tuner impedance coverage, optimal source impedance and selected impedance at different frequencies | 110 |
| Figure 5.10 | Reconfigurable RF fluidic amplifier: a) 3D view and b) fabricated circuit | 111 |
| Figure 5.11 | Reconfigurable fluidic RF amplifier simulated and measured: a) gain, b) group delay, c) input return loss and d) output return loss | 112 |
| Figure 5.12 | Required impedances for simultaneous conjugate matching of the SGA8343Z transistor: a) input and b) output | 113 |
| Figure 5.13 | MEMS-on-LTCC tuner impedance coverage, optimal source and load impedances and selected impedances at 3GHz, 4GHz, 5 GHz and 6 GHz | 114 |
| Figure 5.14 | Reconfigurable RF MEMS-on-LTCC fluidic amplifier 3D view..... | 115 |
| Figure 5.15 | Reconfigurable MEMS-on-LTCC RF amplifier simulated: a) gain, b) group delay, c) input return loss and d) output return loss | 116 |
| Figure 6.1 | Stripline: a) dielectric-filled 3D view, b) air-filled 3D view, c) dielectric-filled side-view and d) air-filled side-view..... | 120 |
| Figure 6.2 | Stripline physical parameters and fields' distribution | 121 |
| Figure 6.3 | Simulated attenuation coefficients (dB/cm) of air-filled and dielectric-filled striplines | 122 |
| Figure 6.4 | CPW vertical transition from CPW upper transmission line to buried: a) dielectric-filled stripline and b) air-filled stripline | 123 |
| Figure 6.5 | Simulated performance of air-filled and dielectric-filled structures with CPW transitions to CPWG lines: a) total attenuations and b) reflection coefficients | 123 |
| Figure 6.6 | Simulated attenuation coefficients (dB/ λ) of air-filled and dielectric-filled striplines | 124 |
| Figure 6.7 | Air-filled 3D MEMS-on-LTCC switch | 125 |
| Figure 6.8 | Field simulation of the dielectric-filled and air-filled 3D MEMS-on-LTCC switches: a) insertion loss, b) phase shift and c) reflection coefficient..... | 126 |
| Figure 6.9 | Air-filled 3D MEMS-on LTCC tuner | 127 |

| | | |
|-------------|---|-----|
| Figure 6.10 | Air-filled and dielectric-filled 3DMEMS-on-LTCC tuners simulated Smith chart coverage and maximum Γ at different frequencies between 2 GHz and 7 GHz | 128 |
| Figure 6.11 | Two-state RF liquid metal cell: a) 3D view and b) cross section view..... | 130 |
| Figure 6.12 | RF liquid metal cell simulated: a) Insertion loss and b) reflection coefficient | 131 |
| Figure 6.13 | Liquid metal tuner 3D view | 131 |
| Figure 6.14 | Liquid metal tuner simulated Smith chart coverage at different frequencies between 2 GHz and 7 GHz..... | 132 |
| Figure 6.15 | RF amplifier smart model | 134 |
| Figure 6.16 | Fluidic circuits control module 3 D view | 135 |
| Figure 6.17 | MEMS circuits' fabricated control module | 136 |

LIST OF ABBREVIATIONS

| | |
|-------|--|
| 3D | Three dimensional |
| ADS | Advanced Design Simulators |
| Al | Aluminium |
| a-Si | Amorphous Silicon |
| CMP | Chemical Mechanical Polishing |
| CPW | Coplanar Waveguide |
| CPWG | Grounded Coplanar Waveguide |
| Cr | Chromium |
| CR | Cognitive Radio |
| Cu | Copper |
| DC | Direct Current |
| DCS | Digital Communication System |
| DI | DeIonized |
| DPDT | Double Pole Double Throw |
| EDGE | Enhanced Data rates for GSM Evolution |
| EGSM | Extended Global System for Mobile Communications |
| EM | Electromagnetic |
| ESIW | Empty Substrate Integrated Waveguide |
| FET | Field Effect Transistor |
| GaAs | Gallium Arsenide |
| GaN | Gallium Nitride |
| GSM | Global System for Mobile communications |
| HFSS | High frequency structure simulator |
| LTCC | Low Temperature Co-fired Ceramic |
| MEMS | MicroElectroMechanical Systems |
| MN | Matching Network |
| PA | Power Amplifier |
| PIN | Positive Intrinsic Negative |
| PAE | Power Added Efficiency |
| PCS | Personal Communications Service |
| Q-TEM | Quasi-Transverse ElectroMagnetic |
| RF | Radio Frequency |
| RPM | Rotation Per Minute |
| SDR | Software Defined Radio |

| | |
|------------------|--|
| SEM | Scanning Electron Microscopy |
| Si | Silicon |
| SIW | Substrate Integrated Waveguide |
| SiO ₂ | Silicon dioxide |
| SPDT | Single Pole Double Throw |
| SPST | Single Pole Single Throw |
| SW-DMTL | Slow-Wave Distributed MEMS Transmission Line |
| UV | UltraViolet |
| VNA | Vector Network Analyzer |

LIST OF SYMBOLS

| | |
|------------------|-------------------------------|
| ϵ_0 | Vacuum permittivity |
| ϵ_r | Relative permittivity |
| ϵ_{eff} | Effective dielectric constant |
| Z_0 | Characteristic impedance |
| E_L | Electrical length |
| Z_{in} | Input impedance |
| λ | Wavelength |
| β | Propagation constant |
| Γ | Reflection coefficient |
| $Tan \delta$ | Dielectric tangent loss |
| c | Light speed |
| σ_r | Residual stress |
| E | Young's modulus |
| α | Damping factor |
| ρ | Material density |
| ν | Material Poisson's ratio |

INTRODUCTION

Following the strategic technology trends, operators worldwide are upgrading their networks to offer various wireless data services and applications to different subscriber categories. They are competing to offer wireless telecommunication systems with higher functionalities and lower costs. Multi-standards multi-bands transceivers that can operate on several coexisting networks have therefore been deployed. Enabling this field prosperity are advances on both software and hardware fronts. In this context, Software Defined Radio (SDR) and Cognitive Radio (CR) have been implemented to promote real time programmable transceivers based on algorithms and software control platforms (Jondral, 2005). This is simply achieved using programmable digital platforms. On the hardware side, a front-end for almost every covered standard or service is defined in the RF front end, resulting in a parallel RF chains transceiver. Figure 0.1 shows a commonly used architecture of a switched multi-standard transmitter (Rodriguez et al., 2013). This topology, built based on parallelised RF components, results in higher hardware complexity, an increase in the numbered required devices, higher energy consumption and higher cost.

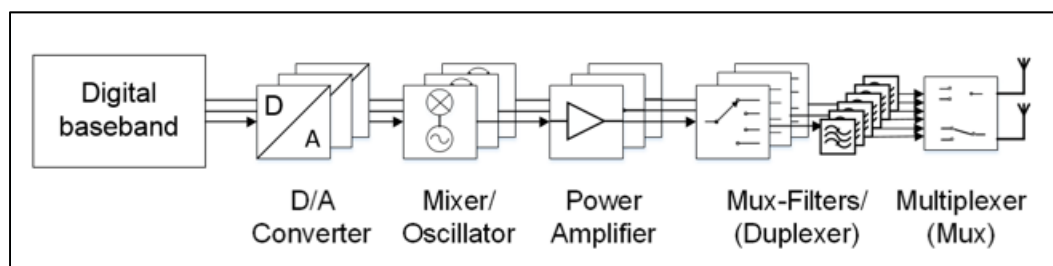


Figure 0.1 Classical multi-standards transmitter with parallel RF chains
Taken from Rodriguez et al. (2013)

As wireless communications get smarter, there is an increasing need for enhanced performances with reduction in size, cost, and energy consumption. Hence, higher constraints on analog circuits and systems, like requiring wideband and/or multiband components, arise. In this context, recent advances that have targeted some of these challenges have been demonstrated. For instance, providing RF and microwave reconfigurable components may offer a promising solution to overcome the common multi-standards architecture limits. Based

on their adaptive capability, these tunable components enable the development of agile front-ends through maximum hardware sharing and smooth switching between the supported standards and applications (Rodriguez, 2015). Heinen et Wunderlich (2011) demonstrated that a reduction in the number of devices of a classical multi-bands transceiver, covering GSM, EDGE and UMTS standards (figure 0.2-a) can be achieved by replacing the parallelized components by shared tunable blocks (figure 0.2-b). In this scenario, a filter, a duplexer, or an amplifier that operate under various requirements and specifications may replace multiple ones. Such wide tunability simplifies the complex multi-standard classical architectures and improves the overall RF performances.

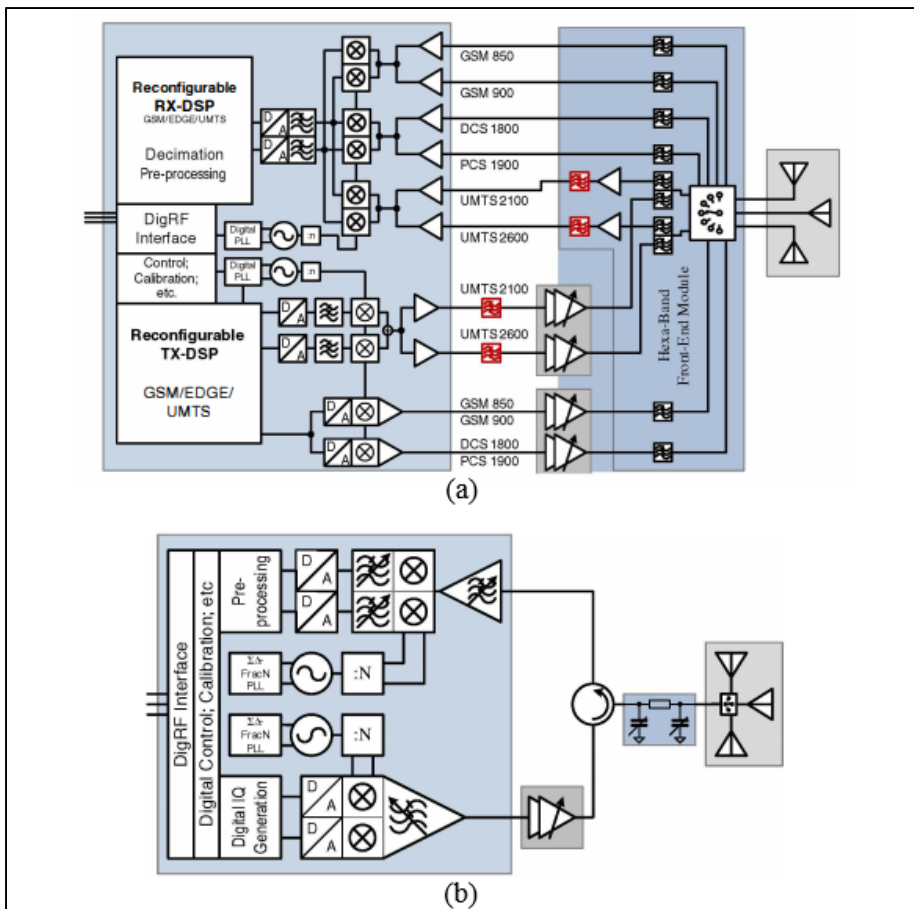


Figure 0.2 Multi-standard RF transceiver implemented: a) in parallel RF chains architecture and b) based on reconfigurable RF components
 Taken from Heinen & Wunderlich (2011)

Reconfigurability in RF and microwave devices is often introduced using MEMS (MicroElectroMechanical Systems) switches, solid-state components like varactors, PIN diodes and transistors or ferroelectrics (Hary, Barton, & Ebel, 2016; Rodriguez, 2015). In these cases, the impedances of these elements are tuned based on an external electrical DC source to alter the circuit's operation. Fluidic metals and dielectrics have also been used to fabricate tunable devices for RF applications (Entesari & Saghati, 2016; Gough et al., 2014). They allow altering a component's response by varying conductors or dielectrics physical properties (dimensions, permittivity, etc.), based on fluids injection into pre-formed channels. Feeding methods like electrostatic or hydraulic actuation are deployed for this purpose.

Problem statement

The concrete advances in the above-mentioned technologies and techniques proved that the development of tunable devices with auto-adjust capability to meet the requirements of emerging communication systems is achievable. For instance, reconfigurable impedance tuners (Domingue, Fouladi, Kouki, & Mansour, 2009), amplifiers (Chen & Peroulis, 2012; Chlieh & Papapolymerou, 2017), filters (Pinon et al., 2012), antennas (Tang & Chen, 2017) and other RF and microwave circuits have been demonstrated. The technology used to tune these devices is always chosen based on the targeted specifications, i.e. RF performances (frequency, loss, power, linearity, efficiency, etc.), tuning speed, size, costs, etc. (Rodriguez, 2015). The existing technologies suffer from two main limitations: (i) they operate mainly at high frequencies, (ii) they request heterogeneous integration which can be sensitive assemblies' precision and tolerance. Therefore, the problem of achieving low and high frequency coverage and higher integration to eliminate some assembly steps may open area of research and will be addressed in this thesis.

Thesis objectives

The main objective of this thesis is to develop, design and fabricate innovative reconfigurable matching networks that can provide a large coverage of the Smith chart over multiple

frequency bands. To do so, will explore two possible approaches: one based on fluidic and the other one on MEMS. We set thereby primary and secondary sub-objectives.

Primary sub-objectives:

- Propose an LTCC (Low Temperature Co-fired Ceramic) fluidic based cell, and frequency reconfigurable impedance tuner;
- Develop a MEMS on LTCC process. To validate this process, we intend to build an RF MEMS switches on an LTCC substrate. This later is used in the design of a planar frequency reconfigurable impedance tuner;
- Generate 3D MEMS-on-LTCC switches and impedance tuners, based on the planar architecture.

Secondary sub-objectives:

- Use the fluidic and the MEMS-on-LTCC tuners in the design of frequency reconfigurable RF amplifiers;
- Enhance MEMS-on-LTCC tuners' performance through loss reduction techniques: integrate air-filled low loss transmission lines in the 3D MEMS tuner and study the effect of low loss liquid metals injection into the fluidic tuner;
- Develop automatic control modules to enable smart operation of the impedance tuners and the reconfigurable RF amplifiers.

Thesis organisation

This thesis, composed of six chapters, explains the feasibility of reconfigurable impedance tuners and RF amplifiers for low and high frequency applications, leveraging the benefits of combining various technologies. It is composed of six chapters:

In chapter 1, an overview about the technologies enabling reconfigurability in RF amplifiers is first detailed. Then, proposed research related to RF tuners and agile amplifiers built based

on fluidic or MEMS architectures are covered. Recent advances in MEMS-on-LTCC process and employed techniques to reduce loss in RF circuits are also presented.

Chapter 2 introduces the LTCC as fabrication technology. It highlights the fabrication steps and details its benefits as a candidate for a variety of applications, including reconfigurable RF circuits.

Chapter 3 details the implementation of fluidic and MEMS based matching networks (or tuners) on LTCC substrate. A general overview of the tuners' operation is first explained. Then, the required dimensioning and design steps of the elementary cells and the tuners developed in both technologies (i.e., fluidic and MEMS) are introduced. Electromagnetic simulations are also exposed. 3D iterations of the MEMS tuner are presented.

Chapter 4 introduces the developed MEMS-on-LTCC process. It details the different steps, and their related challenges and considerations. As a proof of concept, a capacitive RF MEMS-on-LTCC switch with lateral actuation is considered. Simulated electromechanical performance are illustrated.

In chapter 5, measurement experiments and results of the fabricated circuits are presented. Measurements setups are introduced and obtained results are discussed. As application, agile RF amplifiers realised based on the fluidic and MEMS-on-LTCC tuners are then introduced.

Chapter 6 demonstrates the ability to enhance the performance of the proposed reconfigurable components. Here, we suggest integrating air-filled low loss transmission lines in the design of the MEMS-on-LTCC tuner and to replace the content of the fluidic tuner by liquid metals. We also recommend the use of sensing and control modules to promote the tuners automatic operation.

Thesis scientific contributions

This thesis exposes various scientific contributions in the domain of reconfigurable RF circuits, specifically tuners and reconfigurable amplifiers. These latter are intended to be used mainly in low and high frequency applications, where few research have been done. We dealt with theoretical and practical aspects in this context. The major contributions of this thesis are:

- Develop an in-house MEMS-on-LTCC process to be exploited in the fabrication of RF switches and switches'-based RF circuits. All the steps required for the fabrication of these components can be performed in LACIME laboratory: from preparing the LTCC sheets to inspecting and debugging the final component.
- Introduce a general approach for the design of RF tuners based on a limited number of two-state cells. This approach may be applied to several technologies to synthesize tuners with different specifications. For instance, we propose, for the first time, fluidic and MEMS tuners built directly on LTCC substrate with wide coverage at the frequency bands [0.9 GHz, 2.4 GHz] and [2 GHz, 7 GHz], respectively.
- Develop reconfigurable RF amplifiers. Better performance higher integration and smaller size are achieved thanks to an efficient integration of LTCC and fluidic or MEMS technologies.
- Explore the effect of replacing liquid dielectric by liquid metal in fluidic tuners. Leveraging its low loss potential, liquid metal tuner may offer good coverage at higher frequencies, where liquid dielectrics are not recommended.
- Explore the effect of loss reduction techniques in the tuners' functioning. Air-filled transmission lines have been developed. They allow an expansion of the tuner coverage, which even limited, still beneficial for applications where precision is required.

Some of these contributions have been the subject of four papers introduced at the end of thesis.

LITERATURE REVIEW

1.1 Introduction

Achieving reconfigurability of entire RF/microwave chains and subsystems requires that all components of their individual circuits and component be reconfigurable. Arguably, the most challenging components of an RF/microwave chain to make reconfigurable are amplifiers. In this chapter, we focus on the state of the art of frequency reconfigurability of amplifiers. We start by surveying the various alternative architectures that can be used to this end. Next, focusing on amplifier reconfigurability through variable matching networks, we discuss the various technologies and techniques that are used for realizing such networks. Since we aim at combining LTCC and MEMS as a promising solution for achieving matching network tunability improvement, we present the state of the art related to the MEMS-on-LTCC developed processes in the following section. Finally, given that loss in matching networks is critical, we conclude this chapter by detailing some reported low loss transmission lines that can be considered in our research to improve matching networks' performance and amplifier reconfigurability.

1.2 Frequency reconfigurable RF amplifier architectures

An RF amplifier is composed of a transistor, biasing networks, and impedance matching networks. At a fixed frequency point, the biasing point of an unmatched transistor and its required input and output impedances are set to satisfy a particular performance metrics (gain, efficiency, power, noise, etc.). Since transistors' operation and the matching networks behaviour are frequency dependent, designing an amplifier able to operate over multiple frequency bands is challenging. In fact, even if the matching networks are designed to optimize the amplifier's functioning at certain frequency bands, it is hard to reach the targeted performance at other bands. In this section, we present reported methods for designing multi-band/ broadband RF amplifiers.

1.2.1 Unit selection amplifiers

The unit selection type is the most popular method to implement multi-band amplifiers. It consists of N amplifier units, each corresponding to a frequency band (Okazaki, Fukuda, & Nar, 2005). As shown in figure 1.1, the input and output matching networks of each amplifier unit are intended to operate at a single frequency band. When required, a particular amplifier unit is activated by means of two switches.

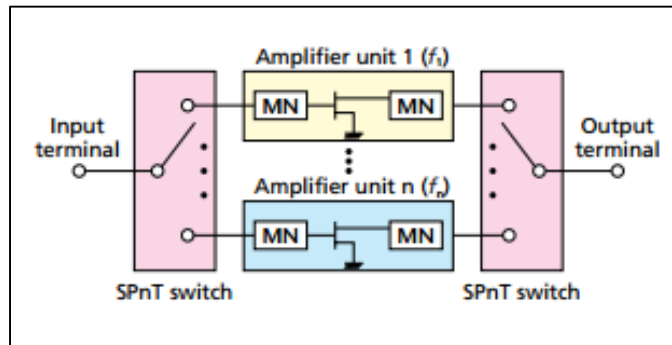


Figure 1.1 Unit selection type multi-band amplifier
Taken from Okazaki et al. (2005)

This amplifier type is commonly used in industry. For instance, Samsung proposed a quad-band power amplifier module covering the GSM850, EGSM, DCS, PCS standards (C.-H. Lee et al., 2009). It uses two parallel stages for the GSM/EGSM low bands, and two parallel stages for the DCS/PCS high bands. At 1dB compression point, it presents an output power higher than 32 dBm and a PAE higher than 55% in the four different frequency bands.

The unit selection multi-band amplifiers are high-performance amplifiers since each stage operates at a particular narrowband frequency. However, the circuit count increases considerably with the covered bands. It also requires very high isolation between different branches to ensure proper functioning of the different units.

1.2.2 Broadband amplifiers

A broadband amplifier is another way to provide multi-band functioning (Okazaki et al., 2005). In this case, the input and output matching networks should present flat frequency response among a large frequency band as shown in figure 1.2.

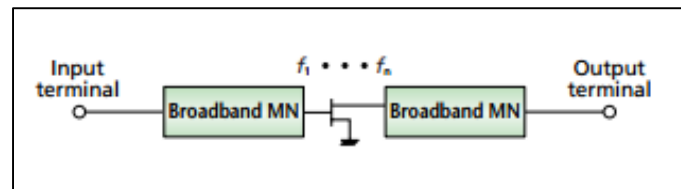


Figure 1.2 Broadband matching type amplifier
Taken from Okazaki et al. (2005)

Ultra-wideband power amplifiers were reported based on broadband RLC matching networks (Hsu, Wang, & Ma, 2005), wideband impedance transformers (Chung, Hsu, Yang, Wei, & Chuang, 2008) or current-reused technique (Murad et al., 2010). These amplifiers operate in the frequency bands of [3.1GHz-10.6GHz], [6GHz-10GHz] and [3GHz-7GHz] respectively.

These amplifiers require large implementation area and are often characterised with bad gain flatness, low output power and/or high power dissipation (Okazaki et al., 2005). Moreover, since the lower and upper limits of the frequency band are farther apart, it is always tricky to build such broadband amplifiers without compromising some performance.

1.2.3 Variable impedance-matching amplifiers

Variable impedance-matching amplifiers can provide multi-band operation. One such amplifier is composed of a single transistor with reconfigurable input and/or output matching networks (figure 1.3) (Okazaki et al., 2005). Tunable components such as varactors, ferroelectrics, MEMS and fluidic channels are used in these matching networks (MNs) designs. Therefore, this architecture's performance depends directly on the characteristics of these components.

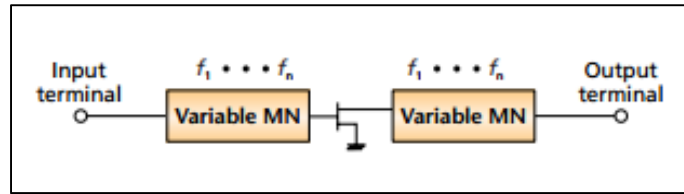


Figure 1.3 Variable matching type amplifier
Taken from Okazaki et al. (2005)

Based on different technologies and topologies, several variable impedance-matching amplifiers have been reported in the literature. Okazaki et al. (2005) proposed a 900 MHz/1900 MHz dual band variable type amplifier using commercial MEMS switches. As shown in figure 1.4, it is composed of a FET transistor and variable matching networks. Sub matching networks, each composed of a transmission line and an open stub, are added at the transistor input and output to provide the required impedances for proper operation around the frequency of 900 MHz (f_1). A transmission line, a shunt switch connected to another matching block are then connected to each port of the pre-matched amplifier. These second sub-MNs are designed to present to the transistor the required impedances around 1900 MHz (f_2), and to take into account the first sub-MNs. This way, when the input and output switches are in the OFF state, the second sub-MNs have no effect and the amplifier operates around f_1 . When they are activated, the PA (Power amplifier) operates around f_2 .

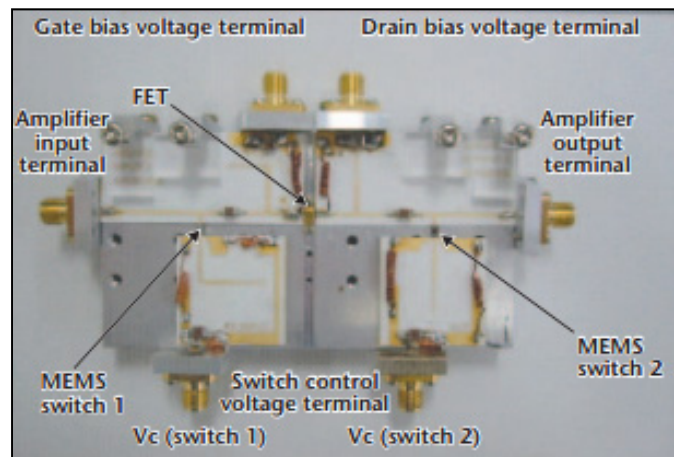


Figure 1.4 900MHz/ 1900 MHz dual band amplifier
Taken from Okazaki et al. (2005)

Figure 1.5 illustrates the output power and the power added efficiency (PAE) relative to the input power at the frequencies 875 MHz and 1875 MHz respectively. In both cases, a PAE higher than 60 % and an output power higher than 30 dBm are obtained.

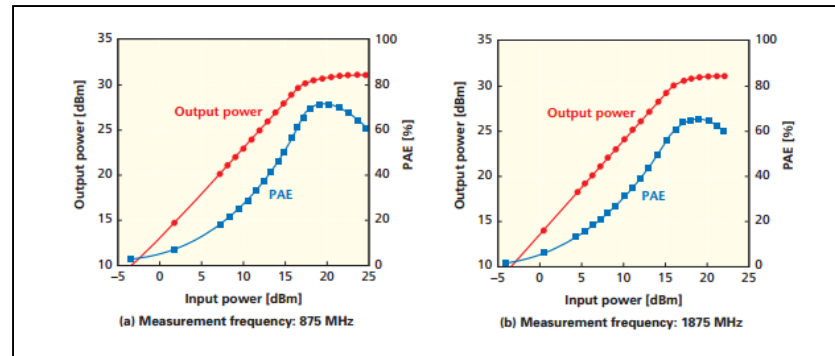


Figure 1.5 900MHz/ 1900 MHz power amplifier performance
Taken from Okazaki et al. (2005)

This technique, known as band switchable configuration, can be extended to cover more frequency bands, through adding several sub-MNs. Each couple of input and output sub-MNs should deliver, based on simple switch control, the required source and load impedances at a particular frequency band. For example, a quad-band power amplifier was reported in (Fukuda, Okazaki, & Narahashi, 2006). The size of the final amplifier is proportional to the covered frequency bands, as two sub-MNs are added for each band. Generally, band switchable amplifiers may cover only limited number of frequency bands, often less than four bands.

A tri-band power amplifier based on GaN-on-Si transistor and RF MEMS device was introduced in (R. Liu, Schreurs, Raedt, Vanaverbeke, & Mertens, 2011). A reconfigurable input impedance matching network and a broadband output impedance matching network were used. As shown in figure 1.6, one commercial RF MEMS switch and a two-stage distributed output network were employed to cover three different frequency bands.

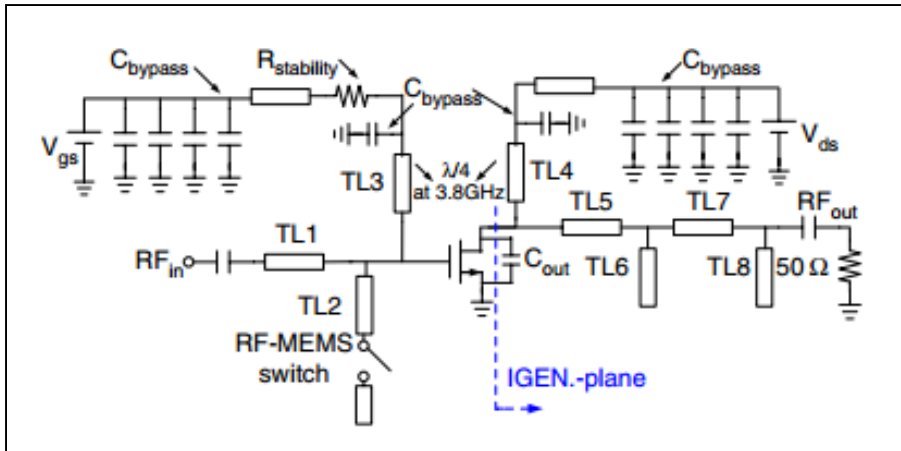


Figure 1.6 Tri-band power amplifier simplified circuit
Taken from Liu et al. (2011)

Measured small signal gain (figure 1.7-a) is approximately equal to 22 dB, 14 dB and 15 dB around the frequencies 1.4 GHz, 2.5 GHz and 3.6 GHz respectively. The amplifier exhibits a high measured power added efficiency of 48, 30 and 52 respectively and provides an output power of more than 3 W at the designed frequencies (figure 1.7-b). However, this architecture cannot cover more than three frequency bands.

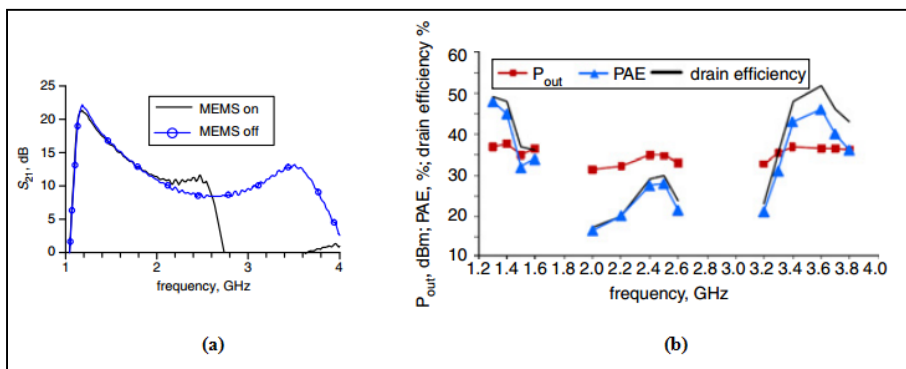


Figure 1.7 Tri-band power amplifier measured performances a) Gain, and b) Output power, power added efficiency and drain efficiency
Taken from Liu et al. (2011)

Domingue, Kouki, et Mansour (2009) proposed a reconfigurable RF amplifier using a tunable MEMS impedance matching network. As illustrated in figure 1.8, a hybrid integration of a GaAs transistor with a tunable input MN and a fixed MN was performed. A slow-wave

distributed MEMS transmission line (SW-DMTL), with 256 states, was used as an input tuner to provide wide impedance coverage even at medium frequency bands.

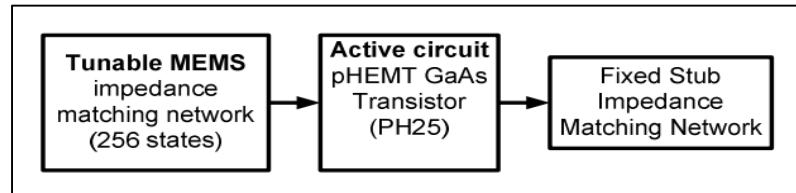


Figure 1.8 Tunable power amplifier scheme
Taken from Domingue et al. (2009)

Figure 1.9 shows good performance of the proposed tunable amplifier over a large frequency bandwidth. Based on a proper choice of the actuated switches, a gain close to the maximum available stable gain is obtained for several frequency bands between 3.5 GHz and 9 GHz (figure 1.9-a). The amplifier is also well matched through the entire frequency band (figure 1.9-b). Clearly, the SW-DMTL-based architecture can insure continuous operation over a wide band while maintaining the same size, i.e., without adding any additional elements or blocs. However, it could not cover lower frequencies ($f < 3.5$ GHz), due to capacitive RF MEMS switches' lower frequency constraint.

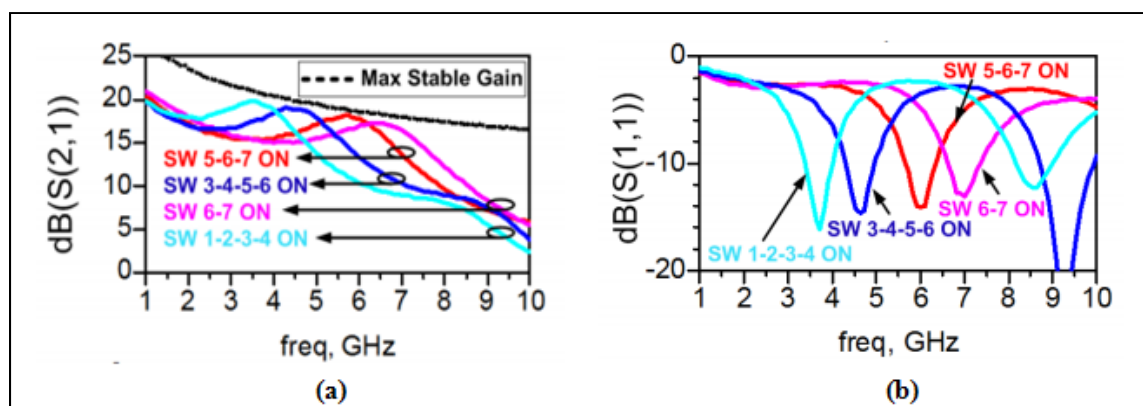


Figure 1.9 Tunable power amplifier performance a) Gain and b) Reflection coefficient
Taken from Domingue et al. (2009)

As explained in the above examples, variable impedance-matching amplifiers are based on presenting reconfigurable impedance MNs to the transistor's input and output, allowing thus

to alter the amplifier's response with a simple architecture. As reconfigurable circuits, tunable impedance matching networks may offer outstanding RF performance while maintaining miniaturised size and low cost.

1.2.4 Frequency reconfigurable RF amplifiers summary

Multiband/broadband RF amplifiers are a necessity for the current and next generation of telecommunication systems. Parallelised amplifier architectures, where a set of narrow-band stages are used, result in components redundancy and have associated issues (complexity, leakage, size, costs, etc.). Wideband amplifiers, while eliminating the redundancy and related issues, are hard to design, and are often limited to few hundreds of MHz in bandwidth. Variable impedance-matching RF amplifiers are promising architectures for wideband frequency reconfigurability. Since they employ tunable MNs instead of the fixed ones, they may provide adjustable operation while maintaining high performance, compact size, and low cost. In fact, reconfigurable MNs are intended to operate for different standards and spectra to enable adaptive operation over a large frequency band without redundant circuitry nor strict design constraints on circuits' level. Hence, variable impedance-matching amplifiers outstand the unit selection and broadband amplifier types, and they are therefore considered in this thesis.

1.3 Frequency reconfigurable impedance-matching networks

Advances in reconfigurable RF amplifiers based on variable impedance-matching network depend on the ability of the used impedance tuner (variable matching network) to present a large number of different impedances. For an optimal operation, these impedance tuners should offer maximum coverage of the Smith chart at different frequency bands. Solid-state components, MEMS switches, ferroelectrics and fluidics have been used to enable such reconfigurability. Here, we enumerate the benefits and limitations of these four technologies in the realization of variable matching networks.

1.3.1 Semiconductor reconfigurable matching networks

A variety of reconfigurable matching networks based on solid state circuits like PIN (Positive Intrinsic Negative) diodes and varactors were developed. Mingo, Valdovinos, Crespo, Navarro, et García (2004) proposed an automatic matching system using a well-designed control method. Instead of using tunable capacitors, as shown in figure 1.10-a, they employed a set of fixed capacitors controlled by PIN diodes (figure 1.10-b). The capacitors' values and numbers are then selected carefully to obtain a uniform impedances distribution over the Smith chart. A particular impedance is therefore a combination of capacitors selected through the activation of the correspondent diodes. Figure 1.10-c illustrates the fabricated tuner.

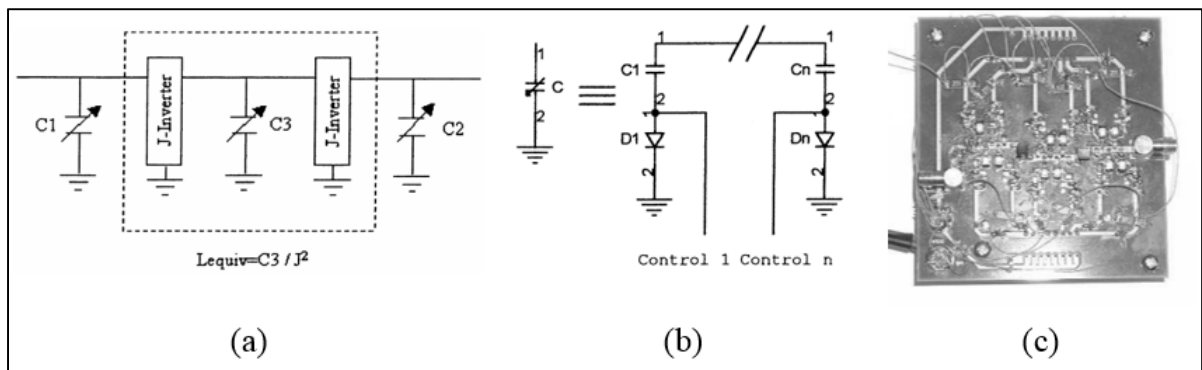


Figure 1.10 PIN diodes automatic matching system: a) equivalent circuit, b) tunable capacitor replacement structure and c) fabricated prototype
Taken from Mingo et al. (2004)

Simulation demonstrates that a uniformly distributed impedances may be synthesized through 12 capacitors at 390 MHz, as shown in figure 1.11-a. However, measured results show a considerably contracted coverage (figure 1.11-b). This major disagreement is due to the PIN diodes' parasitic effects (small resistance and small capacitance) which introduce losses and alter the tuner's operation.

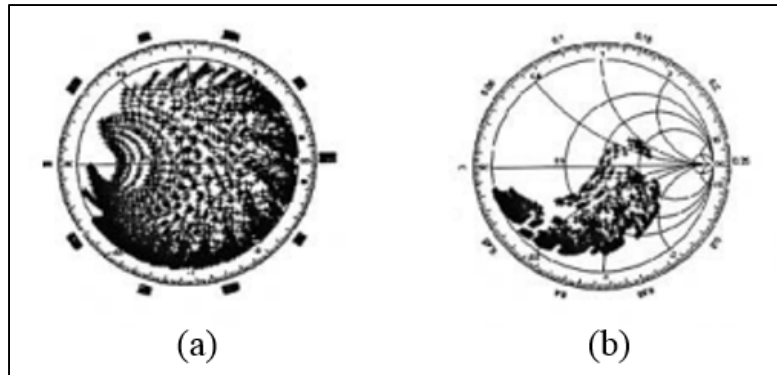


Figure 1.11 PIN diodes automatic matching system:
 a) simulated coverage and b) measured coverage
 Taken from Mingo et al. (2004)

Added et Boulejfen (2015) proposed another variable impedance-matching network using varactor diodes. The network is composed of a high impedance microstrip transmission line, two shunt capacitors and two shunt varactor diodes in Π topology (figure 1.12). The diodes were chosen to generate the maximum coverage between 2.2 GHz and 2.6 GHz. According to the authors, diodes with wide capacitance variation and low parasitic were used. The fixed capacitors were added to compensate the packaging parasitic effect that results in significant contraction of the expected coverage.

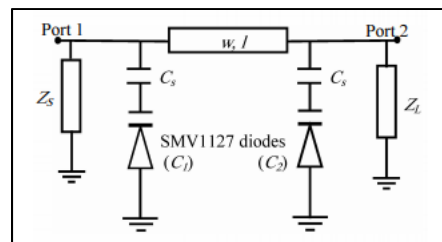


Figure 1.12 Varactor diodes
 based variable matching network
 Taken from Added et al. (2004)

Figure 1.13 shows that the variable matching network, depicted in figure 1.12, has a wide simulated coverage at 2.4 GHz. However, we notice that impedances within the Smith chart borders cannot be synthesised. This topology can operate only over a narrow frequency range and cannot be exploited at high frequencies as it is made from discrete capacitors. Due to the

parastatics associated to the capacitors' packaging, it is expected that measurements, not presented in the paper, would show a contracted coverage.

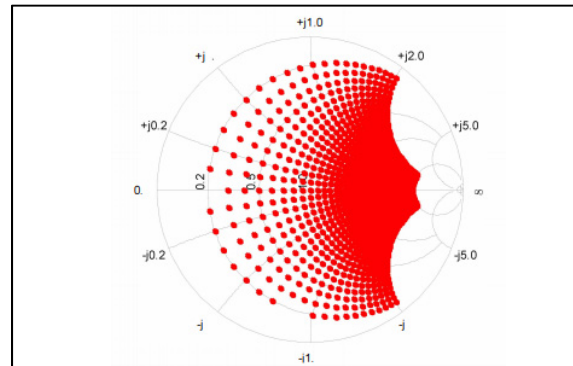


Figure 1.13 Varactor diodes based variable matching network simulated coverage
Taken from Added et al. (2004)

1.3.2 Ferroelectric reconfigurable matching networks

Ferroelectrics may change their permittivity in the presence of an external DC biasing source. They offer therefore tunable devices like ferroelectric varactors. It was proven that such component may bring reconfigurability to RF circuits (Rodriguez, 2015). For instance, a continuously tunable impedance MN was reported (Scheele, Goelden, Giere, Mueller, & Jakoby, 2005). Two ferroelectric varactors, an inductor and a transmission line were mounted in T topology, as illustrated in figure 1.14.

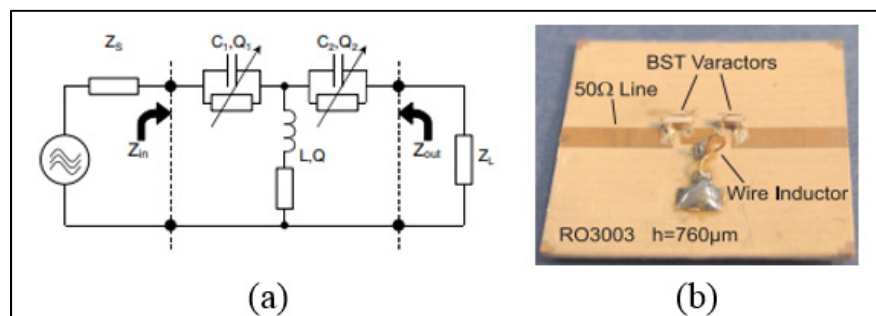


Figure 1.14 Ferroelectric varactors based variable matching network:
a) equivalent circuit, and b) fabricated circuit
Taken from Scheele et al. (2005)

Simulated and measured results at 1.95 GHz are shown in figure 1.15- a and b respectively. Red regions represent the perfect synthesized impedances while the green ones represent those impedances with high input reflection, i.e., return loss higher than 10 dB. The measured covered region with optimum impedances is retraced compared to the simulated one. Ferroelectric varactors are always associated with substrate heating, which results in a capacitance drop. Despite their low power consumption characteristics, they require high DC tuning voltage.

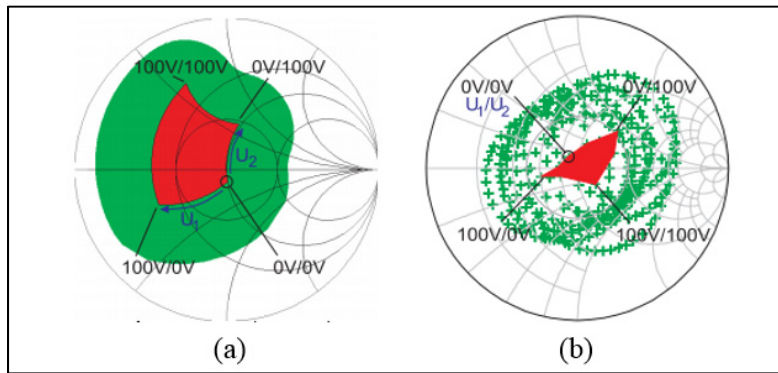


Figure 1.15 Ferroelectric varactors based variable matching network: a) simulated coverage and b) measured coverage
Taken from Scheele et al. (2005)

1.3.3 MEMS reconfigurable matching networks

RF MEMS switches have been a promising solution to develop reconfigurable RF circuits (Rodriguez, 2015). Based on their switching ability, they were used to implement either two states or multi states impedance matching networks. Papapolymerou, Lange, Goldsmith, Malczewski, et Kleber (2003) proposed a double-stub tuner based on MEMS switches (figure 1-16). A set of fixed capacitors and MEMS switches was added to each stub, resulting in a variable-susceptance stub. In this case, the role of the MEMS switches is to activate the required capacitance(s).

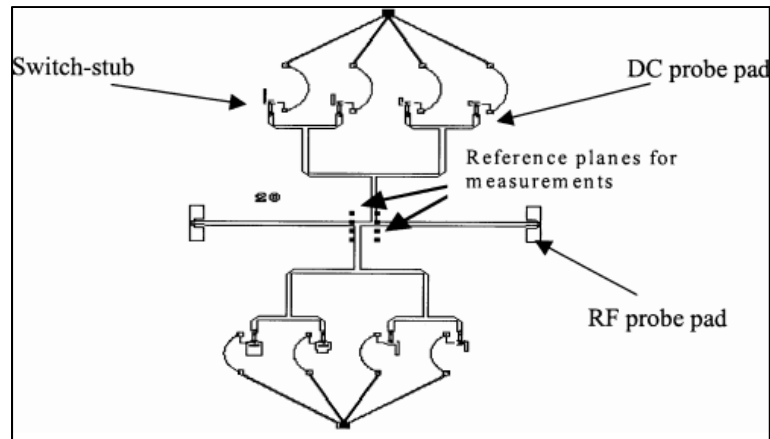


Figure 1.16 Double stub variable matching network based on MEMS switches
Taken from Papapolymerou et al. (2003)

Figure 1.17 illustrates the simulated and measured coverages of a 4×4 bit tuner at 20 GHz, 15 GHz and 10 GHz (Papapolymerou et al., 2003). A good agreement is obtained between both results. This tuner presents a good impedance distribution at high frequencies (20 GHz) thanks to the low loss of the MEMS switches. However, its performance degrades at lower frequencies, where the fixed capacitors values are not optimized. In fact, all the impedances are concentrated within small areas.

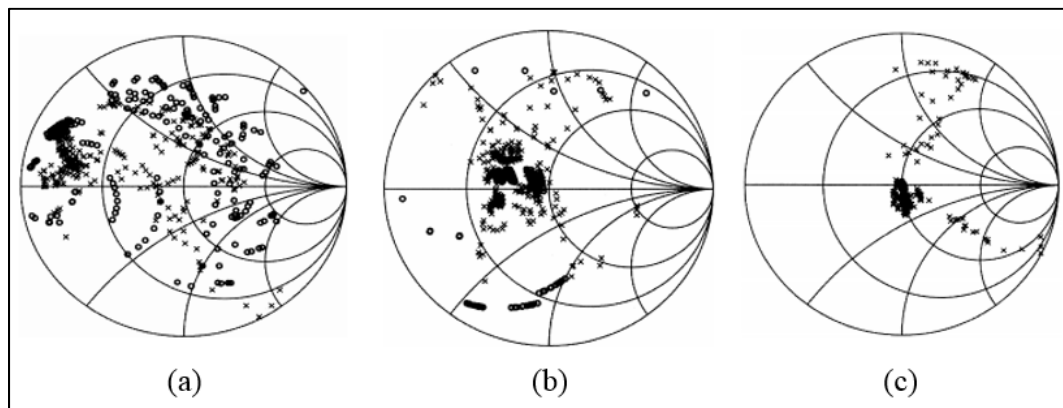


Figure 1.17 Double stub variable matching network simulated (o) and measured (x) coverage at: a) 20 GHz, b) 15 GHz and c) 10 GHz
Taken from Papapolymerou et al. (2003)

Single, double and triple stubs topologies loaded with MEMS switches, as variable capacitors, were also developed as reconfigurable MNs (H.-T. Kim et al., 2001; Tauno Vähä-Heikkilä, Van Caekenberghe, Varis, Tuovinen, & Rebeiz, 2007; Vaha-Heikkila, Varis, Tuovinen, & Rebeiz, 2004). For example, a triple-stub tuner loaded with 13 RF MEMS switches was introduced in (Tauno Vähä-Heikkilä et al., 2007). As shown in figure 1.18-a, several switches are added at different locations between the stubs and along them. Figure 1.18-b shows the fabricated tuner with the DC control circuits.

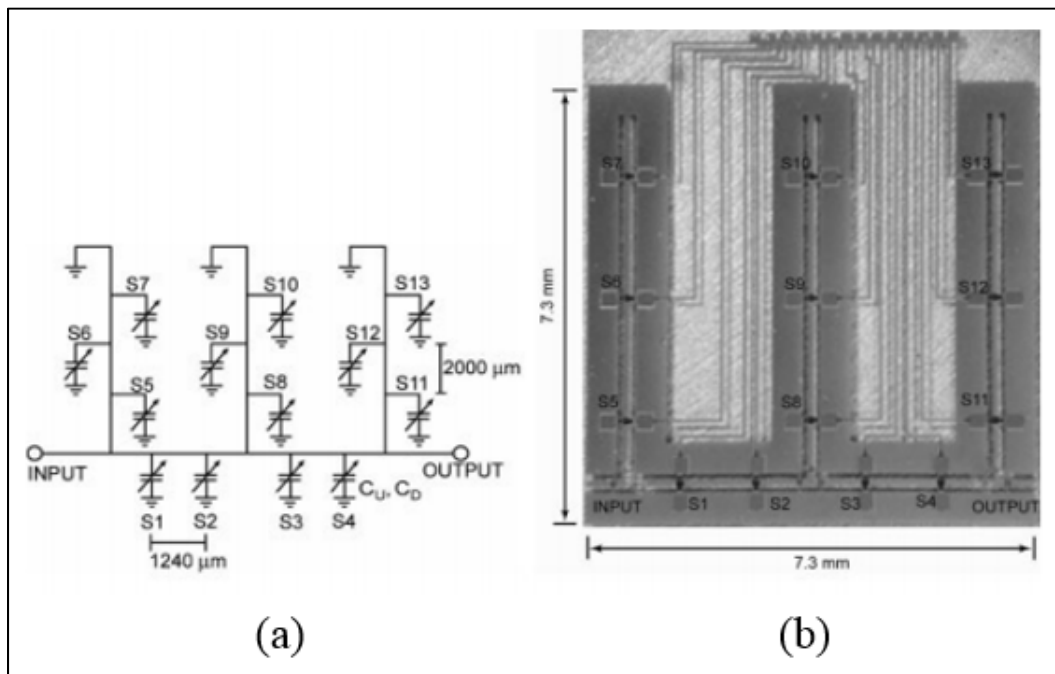


Figure 1.18 Triple stub loaded with MEMS switches tuner: a) equivalent circuit and b) fabricated circuit
Taken from Vähä-Heikkilä et al. (2007)

Using 13 switches, this tuner results in 8192 impedances. Figure 1.19 shows the simulated impedances (8192 points), and a sample of the measured impedances (160 points only) between 6 GHz and 20 GHz. A wide coverage was obtained, particularly for frequencies lower than 16 GHz. It should be noted that several combinations generate the same or nearly the same impedances and therefore, a simpler circuit with less MEMS switches and smaller size may yield to similar impedances coverage.

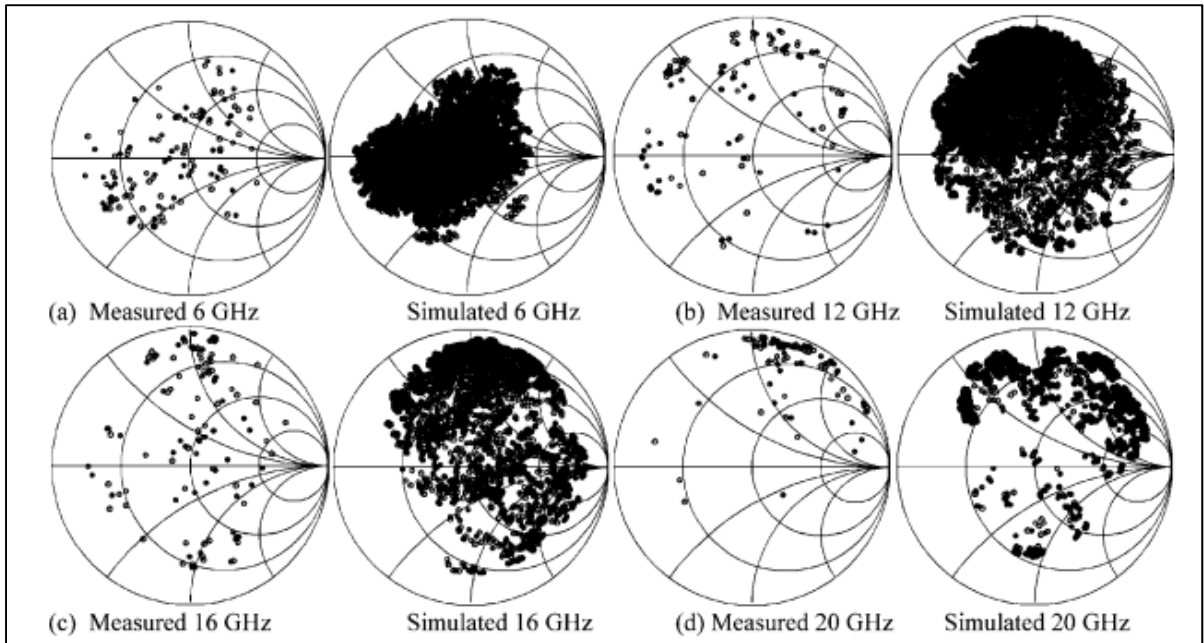


Figure 1.19 Triple stub loaded with MEMS switches tuner impedance coverage
Taken from Vähä-Heikkilä et al. (2007)

Slow-wave distributed MEMS transmission line (SW-DMTL) was used as an RF tuner to provide wide impedance coverage at medium frequency bands (Domingue, Fouladi, et al., 2009). It consists of RF MEMS switches distributed over a non-uniform transmission line (Figure 1.20). This technique increases artificially the substrate dielectric coefficient and so decreases the required size for reconfigurable MNs. The MEMS switches dimensions and their positions were designed carefully for optimum operation.

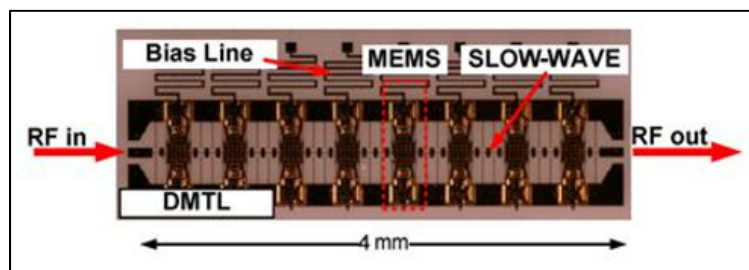


Figure 1.20 SW-DMTL tuner
Taken from Domingue et al. (2007)

Unlike other MEMS based tuners where frequencies are often higher than 6 GHz, sufficient impedance coverage was obtained with this DMTL design even at frequencies lower than 5 GHz as shown in figure 1.21. For wider coverage at lower frequencies, the tuner cells' length should be made electrically larger, while maintaining small size. Additionally, the implementation of the used slow wave structure is complicated.

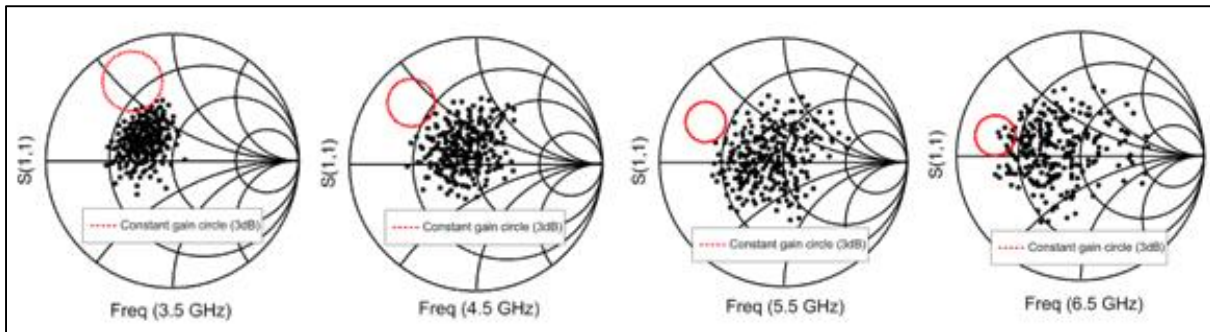


Figure 1.21 SW-DMTL tuner coverage
Taken from Domingue et al. (2007)

1.3.4 Fluidics reconfigurable matching networks

Fluidic dielectrics and metals have also been used to fabricate adaptive RF circuits (Entesari & Saghati, 2016). As demonstrated in (Lei, Hu, Ohta, & Shiroma, 2012), liquid metals, with their ability to vary conductors' physical dimensions based on external actuation methods, can be injected into double-stub matching network to alter its functioning. Each stub length can be changed (figure 1.22) through a control of the liquid metal amount inside the fluidic channel, and thereby generating various synthesized impedances.

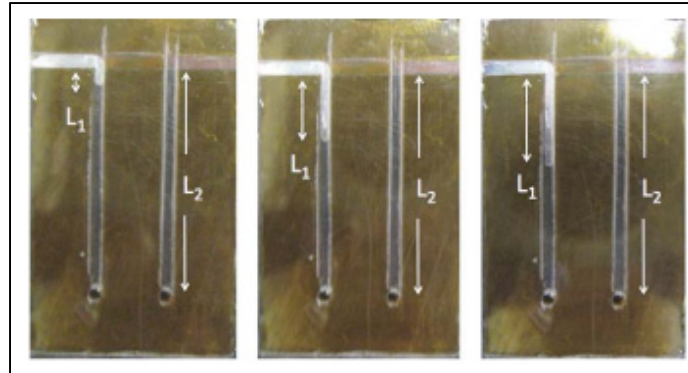


Figure 1.22 Liquid-metal double stub tuner
Taken from Lei et al. (2012)

Figure 1.23 shows the measured coverage for 75 combinations of stub lengths at 3.275 GHz. A non-uniform impedances distribution is obtained all over the Smith chart. Although a wider coverage may be obtained for continuously tuned stubs, monitoring the liquid's shapes precisely remains challenging and requires high voltage or high pressure. Fluid metals, like Gallium based ones, oxidise rapidly (McClung, Saeedi, & Sigmarsson, 2018). Residues may remain on the fluidic channels' surfaces (Watson et al., 2019), resulting in distorted operation.

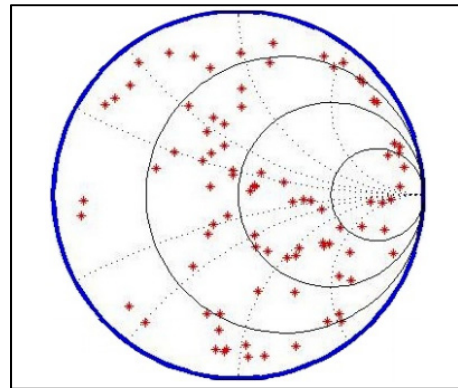


Figure 1.23 Liquid-metal double stub tuner coverage at 3.275 GHz
Taken from Lei et al. (2012)

As for fluidic dielectrics, i.e., fluids, with typically high relative permittivity, may be injected into pre-formed channels inside the solid dielectric substrate supporting the RF circuit. This allows the control of the resulting structure's permittivity, and thereby enabling

reconfigurability of tuners (Entesari & Saghati, 2016). To our knowledge, multi-state reconfigurable MNs covering many impedances on the Smith chart have not yet been reported. Only a two-state MN was introduced as in (Chlieh & Papapolymerou, 2017). It consists of a double-stub MN formed from microstrip transmission lines as shown in figure 1.24-a. It is designed on a multilayer substrate composed of a ground plane, a cavity on a thick RO3003 dielectric, an LCP layer and a copper conductor layer, as illustrated in the stack-up of figure 1.24-b. Filling the cavity with air ($\epsilon_r=1$) or acetone ($\epsilon_r=20$), results in varying impedances at different frequencies.

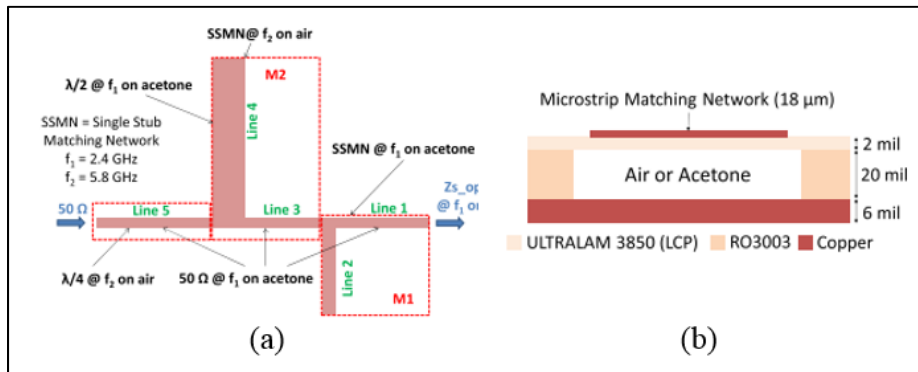


Figure 1.24 Fluidic dielectric double stub tuner
Taken from Chlieh et al. (2017)

Other few states MNs based on micromachining techniques were also presented. (Pinon et al., 2012; Tang & Chen, 2017) proposed a resonator operating at 25 GHz and 18 GHz based a microfluidic channel, where air and water were used. Here, microfabrication techniques are limited to small size channels. They are therefore not useable at low to high microwave frequencies.

1.3.5 Frequency reconfigurable matching networks summary

The four technologies presented in the previous sections have demonstrated their potential to provide reconfigurable MNs through several studies. However, as explained, some issues have to be considered for each one. Table 1.1 gives a summary of these technologies when used in reconfigurable matching networks.

Table 1.1 Comparison of reconfigurable matching networks technologies

| | Semiconductor | Ferroelectric | MEMS | Fluidic |
|------------------------------|--|--|---|--|
| Frequency range | <ul style="list-style-type: none"> • Low frequencies • Limited number of frequency bands | <ul style="list-style-type: none"> • Low frequencies • Limited number of frequency bands | <ul style="list-style-type: none"> • Low/ high frequencies • Many frequency bands | <ul style="list-style-type: none"> • Low/ high frequencies • Limited number of frequency bands |
| Coverage | Poor | Poor | Wide | Poor/ Wide |
| Integration level | Poor | Poor | Poor | Poor |
| Loss | Very high | High | Low | Low/ High |
| Actuation method | Electrostatic: low voltage | Electrostatic: high voltage | Electrostatic: medium voltage | Electrostatic: high voltage/ hydraulic: high pressure |
| Fabrication procedure | Complex | Complex | Complex | Complex |
| Tuning speed | Fast | Fast | Slow | Slow |
| Power handling | High | High | Low | High |

1.4 MEMS-on-LTCC substrate

As explained in section 1.3, RF MEMS switches are among the most popular elements used in the design of reconfigurable RF matching networks and amplifiers. Planar substrates like silicon (Si) and alumina are commonly used in this context. In this project however, we aim to build more sophisticated, more compact and lower loss integrable MEMS impedance tuners. To this end, we seek to use LTCC as a low-loss multilayer functional substrate for MEMS devices' integration instead of the conventional silicon and alumina. Despite its potential, MEMS-on-LTCC does present challenges, which explain in large part the thin open literature on this subject. In the following sub-sections, we present reported works on MEMS-on-LTCC processes and highlight the key challenges faced.

1.4.1 Laser micro-machined MEMS process

D'Auria, Sunday, Hazell, Robertson, et Lucyszyn (2014) have reported a novel process for the development of ultra-low cost MEMS-on-LTCC process. Following the screen-printing of the RF transmission lines and DC electrodes, they replaced the spacer layer, commonly used in MEMS processes as suspended beam (figure 1.25-a), by a well-controlled laser-induced stressed layer (figure 1.25-b). This way, the thin aluminium cantilever bent, resulting on creating the required gap (figure 1.25-c). Switches with different cantilever shapes based on this process were developed and tested.

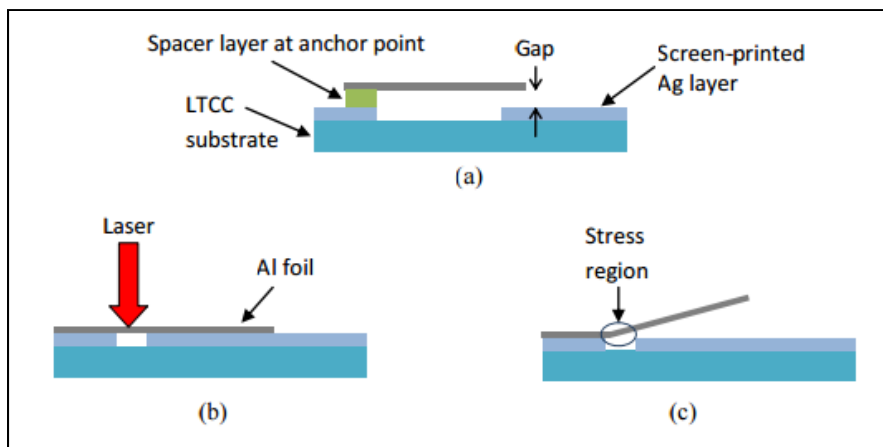


Figure 1.25 MEMS on LTCC based on laser bending
 Taken from D'Auria et al. (2014)

The simulated switches present adequate mechanical (displacement, stiffness, etc.) and RF performance (isolation, insertion loss, etc.). However, they require very high voltage to operate. In fact, the actuation voltage varies between 255 V and 505 V depending on the cantilever shape. These high voltages are the main drawback of this process.

1.4.2 Surface micromachining MEMS process

Capacitive MEMS-on-LTCC RF switches were first introduced by Cianci et al. (2007). They were built using surface micromachining technique on LTCC substrate. In the proposed

process, the substrate was polished to decrease its roughness to less than 10 nm. When the required smoothness of the substrate was reached, the following steps, as illustrated in figure 1.26, were performed:

- Biasing lines and pull-down electrodes patterning (a);
- Amorphous silicon (a-Si) deposition as sacrificial layer (b);
- Anchors and dimples patterning and etching (b);
- Bridge deposition (sputtering and patterning) (c);
- Sacrificial layer removal (dry etching) (d).

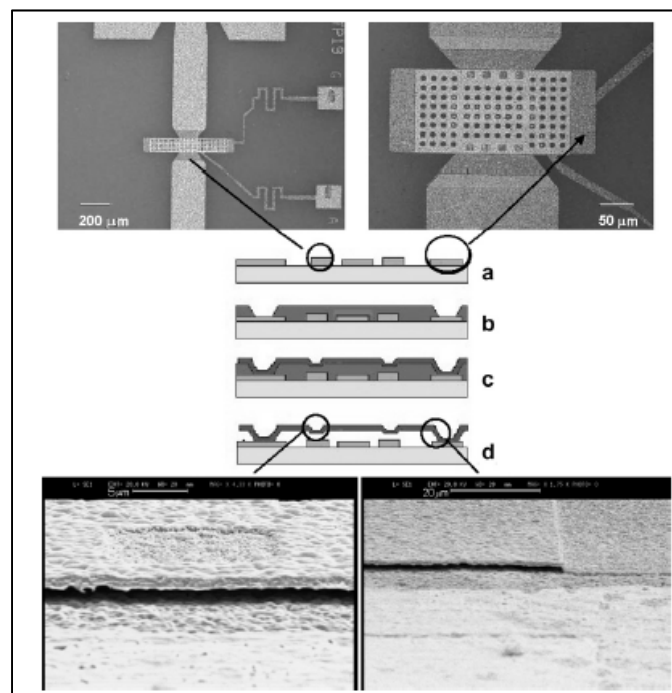


Figure 1.26 Capacitive MEMS on LTCC process
Taken from Cianci et al. (2007)

The proposed switch presents good performance with low actuation voltage ($<15\text{V}$) in vacuum. However, it suffers from stiction phenomena when tested in air due to humidity. Moreover, it presents an unpredicted contact resistance of about $10\ \Omega$. The authors argued this large resistance to the low contact force between the bridge and the RF line. As a solution, they

suggested to increase the dimples area and to use a dielectric layer (SiO₂) on the LTCC substrate to further decrease its roughness.

Few works were then published on surface micromachining MEMS-on-LTCC process. For example, Xiaoyu, Osamu, et Satoshi (2010) proposed an RF MEMS switch on high-k LTCC substrate. An LTCC wafer with inner vias and interconnects was formed as a first step of the process. Then, MEMS components were directly designed on the wafer surface following the process detailed in figure 1.27. The proposed switch served to build a tunable RF filter. Therefore, a successful MEMS-on-LTCC process able to be used in the design of operational devices is finally developed. However, only few details about the steps and fabrication requirements are published.

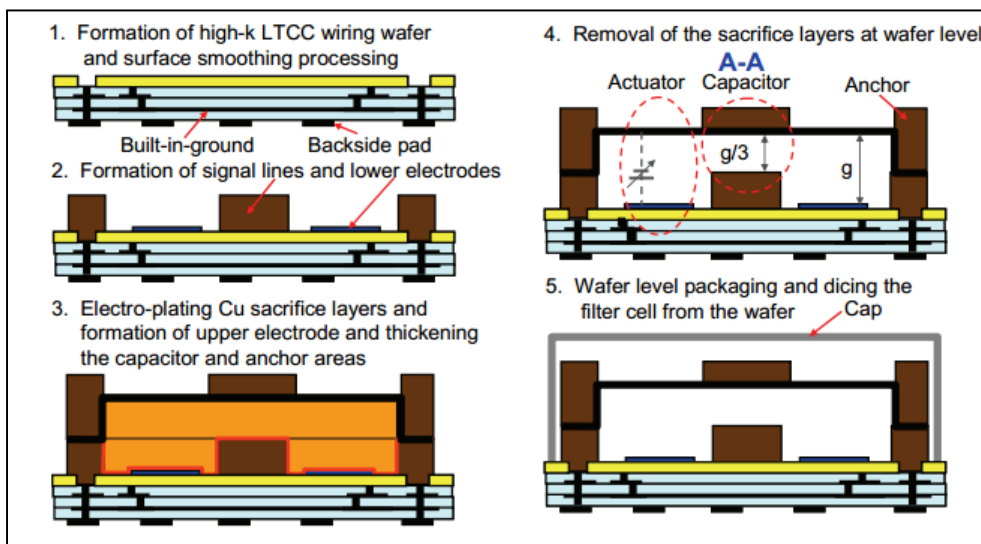


Figure 1.27 Capacitive MEMS on high-k LTCC substrate
Taken from Xiaoyu et al. (2010)

Recently, Thales Alenia Space proposed an SPST (single-pole-single-throw) (figure 1.28-a) and a SPDT (single-pole double throw) (figure 1.28-b) RF MEMS switches developed directly on LTCC substrate (Lucibello et al., 2018). They exhibit promising performance in term of RF characteristics (insertion loss lower than 1.5 dB and isolation higher than 15 dB up to 26 GHz), mechanical reliability (more than 10^6 cycles), and DC behavior (contact quality). Thales Alenia

Space decided also to keep its process secret and no details were disclosed about the followed steps and the used recipes.

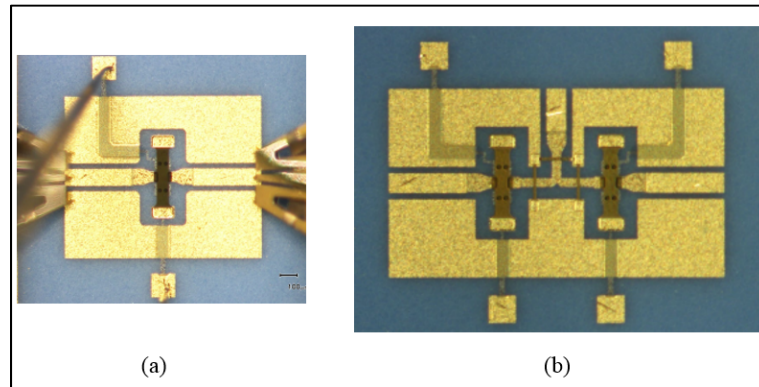


Figure 1.28 MEMS on LTCC: a) SPST switch and b) SPDT switch

Taken from Lucibello et al. (2018)

1.4.3 MEMS-on-LTCC summary

Leveraging the LTCC capabilities, MEMS-on-LTCC process promises enhanced electrostatic RF MEMS switches. Further to maintain silicon based MEMS benefits, it offers enhanced performances, mainly better RF characteristics, full integration and further miniaturisation. However, few researchers and industries are interested to these switches, probably due to the challenges associated to the process development. In addition to the access requirement to both technologies, this process involves intensive investigations about MEMS layers and LTCC surfaces compatibility. Although few works have been reported in this area, as summarized in table 1.2, functional processes have been developed, and are in use for the development of reconfigurable RF circuits as in (Xiaoyu et al., 2010).

Table 1.2 MEMS-on-LTCC process summary

| | Ref | Strengths | Limits |
|---|--------------------------|--|--|
| Laser based process | (D'Auria et al., 2014) | <ul style="list-style-type: none"> • Good RF performance • Good mechanical performance • Low cost • Easy process | <ul style="list-style-type: none"> • Very high actuation voltages |
| Surface micromachining based process | (Cianci et al., 2007) | <ul style="list-style-type: none"> • Good RF performance in vacuum • Low actuation voltage | <ul style="list-style-type: none"> • Stiction problem in vacuum • Low contact force between the bridge and the RF signal line. • Complicated fabrication process. |
| | (Xiaoyu et al., 2010) | <ul style="list-style-type: none"> • Operational process • Integrated in the design of a tunable RF filter | <ul style="list-style-type: none"> • Few details are published about the process development (insufficient information to reproduce the process) |
| | (Lucibello et al., 2018) | <ul style="list-style-type: none"> • Operational process • Integrated in the design of SPST, SPDT and DPDT | |

1.5 Low loss RF transmission lines

Transmission lines are commonly used in microwave applications as they are required to guide electromagnetic (EM) waves from one point to another (Teixeira, Radhakrishnan, & Chew, 2005). However, their inherent dielectric, conductor and radiation losses have always been a research and discussion issue since they may cause significant power dissipation and signal distortion. For high frequency devices where long lines are required, reducing signal attenuation of such guiding structures results in better performance. Therefore, there has been an increasing interest in providing low-loss transmission lines while maintaining small size, low cost and easy integration. In this section, we introduce some reported low loss transmission lines and guiding structures.

1.5.1 Waveguides

Waveguides, hollow metallic tubes, are among the first guiding structures used in signal routing at microwave frequencies (Pozar, 2012). They are still used, particularly for very high frequency applications due to their unique characteristics. Formed from free space surrounded by one conductor wall, they are generally immune to signal interferences and may handle extremely high power. They often have lower losses compared to other transmission lines, since they use only air as a dielectric (Pozar, 2012). They are known to operate above a cut-off frequency, which depends on their cross-sectional shape and dimensions, i.e., radius in case of a cylindrical waveguide and width and height in case of a rectangular one. Therefore, they are often recommended for millimeter wave application. However, at lower frequencies, they tend to become bulky and heavy. They are also relatively expensive and requires complex transitions to other circuits.

1.5.2 Substrate Integrated Waveguides (SIW)

SIWs composed of a dielectric layer in between two metal plates connected through two rows of metallic vias holes, is a promising alternative to conventional waveguides (Deslandes & Wu, 2006). As a planar structure, it is easily fabricated and is highly integrated with both conventional waveguides and planar printed transmission lines. Considered as a laminated waveguide, it maintains the shielded environment with long metallic walls. Therefore, it is protected from interferences and has low conductor and radiation losses. For further loss reduction, Empty SIW (ESIW) are introduced as in (Isapour & Kouki, 2017). As shown in figure 1.29, it consists of replacing the solid dielectric, responsible of dielectric losses, by air.

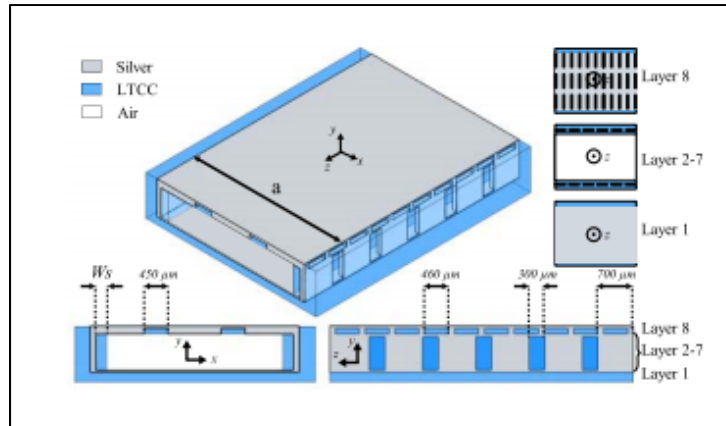


Figure 1.29 Empty LTCC SIW
Taken from Isapour et al. (2017)

Both simulation and measurement demonstrate an insertion loss lower than 0.5 dB, with better than 20 dB of return loss from 57 GHz to 66 GHz (figure 1.30). This SIW is also suitable for very high frequency applications, where the wavelength is still small. Despite dielectric loss reduction with dielectric suppression in ESIW, conductor losses still present. Moreover, these SIWs require well designed transitions to other transmission lines to avoid performance degradation.

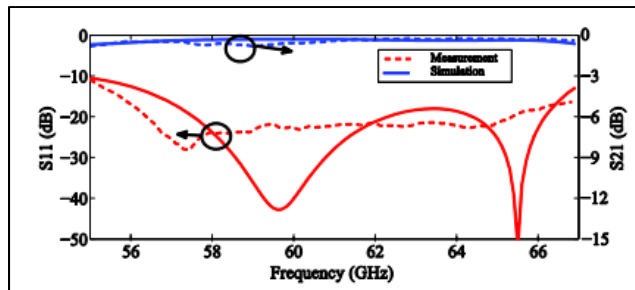


Figure 1.30 Empty LTCC SIW simulated and
measured S parameters
Taken from Isapour et al. (2017)

1.5.3 Air-filled planar transmission lines

A micromachining technique has been exploited in the implementation of suspended transmission lines to offer low loss guiding structures. Numerous structures have been

presented in the literature. For example, a multilayered air gap stripline and a rectangular coaxial line were proposed by Jeong et al. (2002), as shown in the SEM (Scanning Electron Microscopy) photograph depicted in figure 1.31. The different layers were fabricated using several lithography and Cu (Copper) plating steps to form a 50Ω low loss transmission lines. To enable the signal line release, some holes were added to the top layers. According to the authors, they were carefully designed to reduce losses and prevent radiation.

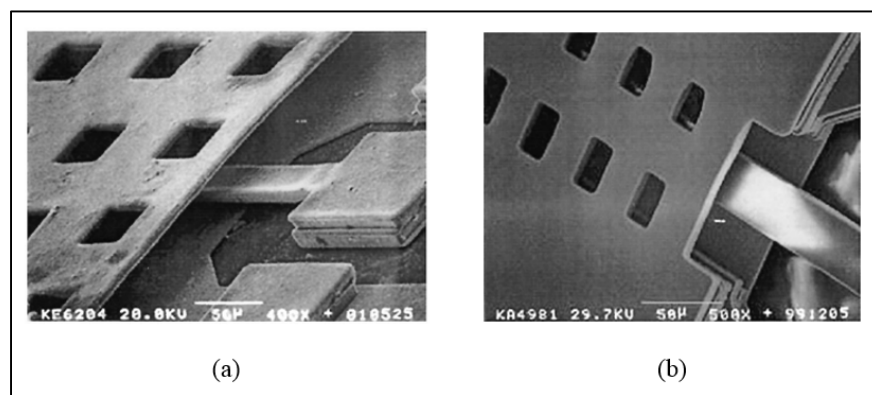


Figure 1.31 Micro-machined air gap: a) stripline and b) rectangular coaxial line
Taken from Jeong et al. (2002)

Jeong et al. (2002) demonstrated that high performance may be reached when solid dielectrics are replaced by air (i.e., dielectric losses are removed) in guiding structures. In fact, the proposed air gap stripline and coaxial line are well matched from 2 GHz to 40 GHz and their attenuation coefficients are lower than 0.2 dB/mm (figure 1.32-a) and 0.08 dB/mm (figure 1.32-b) respectively. They may be integrated easily with other circuits. However, a deflection of the suspended line during the release step may result in an impaired operation. Transitions to other structures may also affect their expected performance. For example, Vanhille, Lukic, Rondineau, Filipovic, et Popovic (2007) developed another copper air-filled rectangular micro-coaxial line for antenna applications based on a surface micromachining technique. While simulated attenuation is very low, the measured one degrades significantly. Therefore, such micro-machined air-filled transmission lines are sensitive to inner conductor offset, layer alignment and sacrificial layer etching. Fabricating operational air gap planar transmission lines is still challenging.

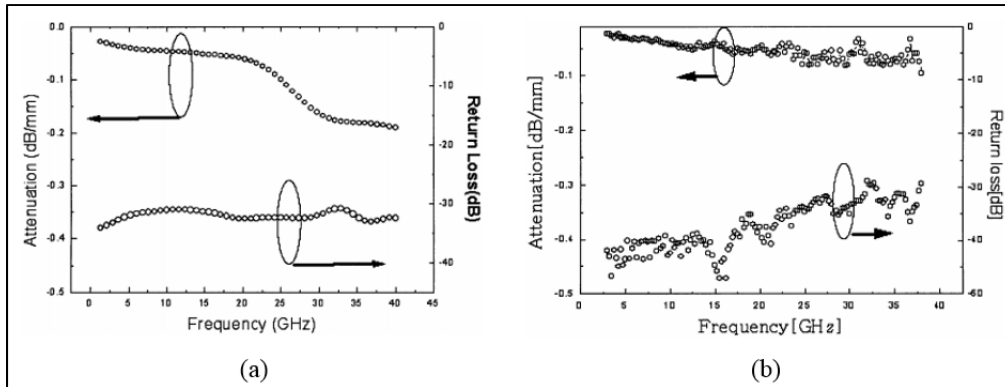


Figure 1.32 Performance of the micro-machined air gap: a) stripline and b) rectangular coaxial line
Taken from Jeong et al. (2002)

1.5.4 Low loss RF transmission lines summary

Numerous low loss guiding structures such as waveguides, SIW and air-filled planar transmission lines have been reported. Table 1.3 summarizes their main benefits and limitations. Waveguides are the best choice as low loss mediums at high frequencies. However, being voluminous and bulky, they require complicated transitions to other interconnects and components. SIW, and ESIW as a hybrid between waveguides and planar transmission lines demonstrated that they can provide low loss performance as waveguides, with miniaturized size and easy integration with printed circuits. They offer promising performance for millimeter wave applications, but still suffer from big sizes at low frequencies. Known by their ease of fabrication and complete integration, planar transmission lines have been commonly used in microwave circuits' design. Their major issue is their attenuation coefficient. Air-filled transmission lines have been developed to reduce losses in such planar guiding structures. Indeed, using air as a dielectric enable eliminating solid dielectric related losses, an important attenuation source. Microfabrication techniques, used in the development of such lines, are complicated, and performance of the fabricated structures depends widely on the fabrication process maturity.

Table 1.3 RF guiding structures summary

| Reported works | Benefits | Limits |
|---|---|--|
| Waveguides | <ul style="list-style-type: none"> • Very low losses • No crosstalk | <ul style="list-style-type: none"> • Large size • Very large size at low frequencies • Non-planar structure → difficult integration |
| Substrate Integrated Waveguides (SIW) | <ul style="list-style-type: none"> • Low losses • Miniaturised structures relative to waveguide | <ul style="list-style-type: none"> • Loss generated from vias and dielectric • Large size at low frequencies • Challenging transition to planar interconnect circuits |
| Air-filled micro-machined planar transmission lines | <ul style="list-style-type: none"> • Low losses • Miniaturised structures | <ul style="list-style-type: none"> • Difficult fabrication process • Non-planar structure → challenging transition dielectric-filled planar interconnect circuits |

1.6 Conclusion

Different approaches for introducing reconfigurability in RF amplifiers based on impedance tuners have been surveyed, presented and discussed. This literature survey shows that reconfigurability is often achieved through solid-state components, ferroelectrics, MEMS switches or fluidics. In all cases, the impedances of these elements are tuned based on an external excitation (electrical DC bias, pressure, etc.) to alter the circuit's operation. Each of the technologies used to enable such tunability has its own set of benefits and drawbacks. Unlike solid-state components and ferroelectrics, both known to have relatively high losses, MEMS and fluidics seems to be more suitable to build RF tuners with wide coverage through large frequency band. Performance of such components can be further enhanced by a proper choice of the used substrate and/or the introduction of low loss techniques. LTCC as a substrate for fluidic and MEMS circuits is a good candidate for this application. It may also support low loss guiding structures. However, only few works have been reported in this context, hence the proposed focus of this thesis. In the next chapter, we give a detailed presentation of LTCC technology and how it can be leveraged for developing reconfigurable RF circuits.

LTCC FABRICATION TECHNOLOGY

2.1 Introduction

Low temperature co-fired ceramic is a 3D ceramic substrate. Known with its reliable electrical performance at both low and high frequencies, and its compatibility with various processes and materials, LTCC is considered as an excellent substrate for many applications. In this chapter, we present a general overview of LTCC as fabrication technology, and we detail its advantages and drawbacks. We also describe the steps of the fabrication process. Then, we demonstrate its compatibility with fluidic and MEMS technologies and explain how it can be used to build reconfigurable RF circuits and amplifiers.

2.2 LTCC technology description

2.2.1 Overview

LTCC is a multilayer technology. It allows realizing compact circuits by embedding passive and active elements in a 3D layered structure. As shown in figure 2.1 (Khodor, 2013), an LTCC structure is typically composed of several ceramic layers, interconnection and thermal vias, conductors and mounted components. Passive devices like resistors, inductors and capacitors can be buried into the internal layers or printed on the surface, whereas active components are mounted on the surface. Also, open and closed cavities can be realized in this substrate.

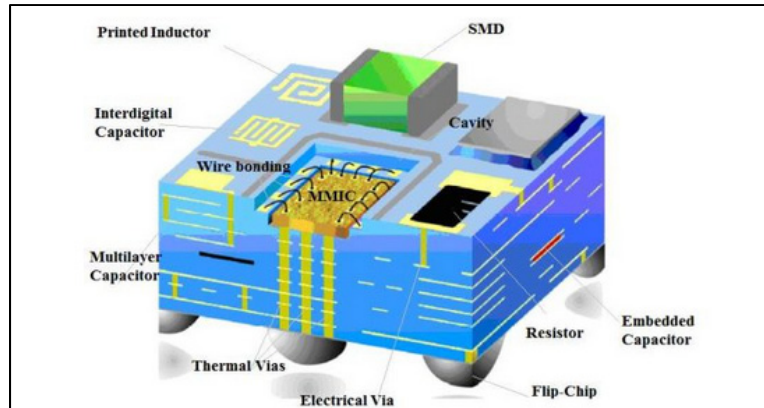


Figure 2.1 Representative scheme of an LTCC substrate
Taken from Khodor (2013)

2.2.2 LACIME in-house LTCC process

At LACIME laboratory, we have an in-house LTCC process. It is a well-established process and its standard guidelines are shown in figure 2.2 as described in (LTCC@ÉTS, 2018). First, green tape layers are blanked from a roll. Then, via holes are punched and filled with conductive material. Inner and outer layers are printed with the appropriate pattern using screen printing. All layers are then stacked and laminated. After cutting, circuits are ready for the sintering step which is carried out following a specific temperature profile where the maximum temperature reaches 850°C in several heating sub-steps. As post treatment, additional elements can be printed on the top layer. Surface mount components (like transistors, capacitors, resistances, etc.) can be mounted on the outer surfaces. Specific inspections are carried out during the different steps, to avoid potential irreversible failures. The final circuit is inspected and tested. Indeed, optical microscopy and X-rays are used to inspect the outer and inner layers respectively. RF and DC tests are also performed through VNAs (Vector Network Analyzers), multi-meters, power supplies, etc. Some imperfections can be corrected if they are located in the outer faces. Extra steps can be added to this regular process, bringing therefore more flexibility to this multilayer technology. They may be performed between the basic steps and/or as a post-treatment step. For example, inner and outer cavities can be formed in LTCC substrate. They should be drilled in the required layers before the collating (or stacking) step. Surface micro-machined structures can be realized on a post-treated co-fired LTCC surface.

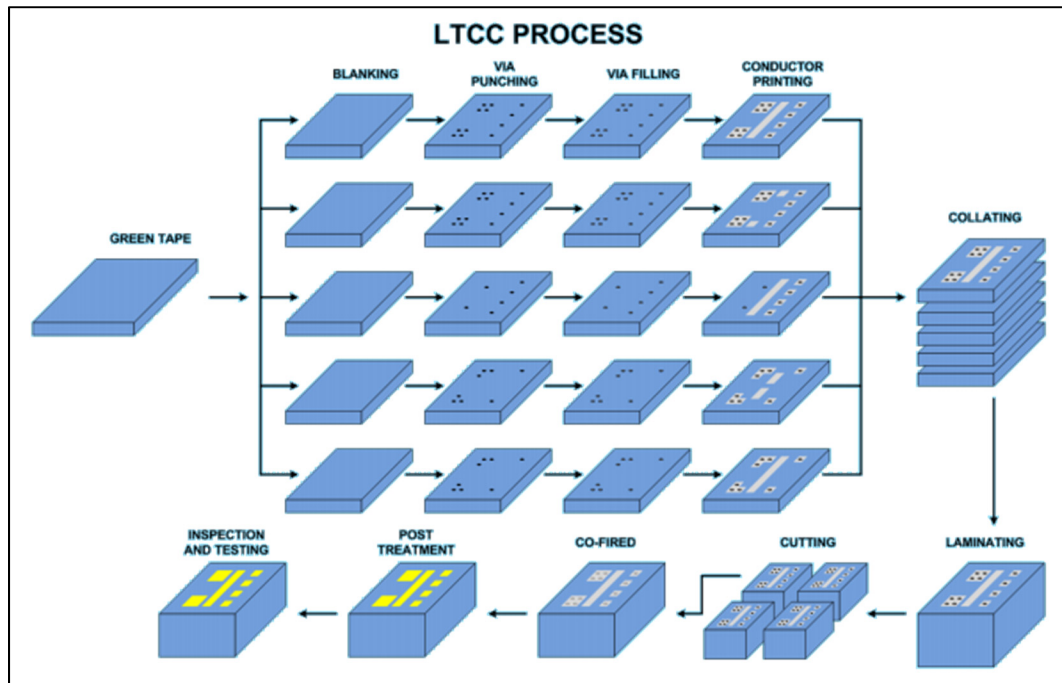


Figure 2.2 LTCC@ÉTS process flow
Taken from LTCC@ÉTS (2018)

2.2.3 LTCC technology benefits

In light of its electrical mechanical and thermal properties, LTCC have been used even in harsh environment. It is still among the best choices for most demanding applications in telecommunication, aerospace, radar, automotive, etc. This is due mainly to its advantages detailed in the following:

- **Low loss:** LTCC technology provides low dielectric dissipation factor and low conductor resistances. The dielectric dissipation factor of most LTCC green tapes varies generally between 0.001 and 0.006, a very low value compared to other substrate types. Gold and silver, known with their low resistivity, are the metals generally used in this technology.
- **High integration density:** an LTCC single stack-up may integrate several components without the need of external connections. This simplifies the circuit's architecture, reduces

the components' number, and eliminates certain assembly tasks. Lower losses, less failures, smaller sizes, and lower costs are thereby ensured.

- **Non-uniform shapes:** due to its multilayer nature, different shapes of dielectrics, and conductors are possible in the LTCC technology.
- **High thermo-mechanical stability:** the coefficient of thermal expansion (CTE) of most LTCCs varies between 5 and 8 ppm/°C. This low coefficient prevents important expansion of the substrate. It thereby allows LTCC based circuits to maintain their integration and reliability in the presence of heat stress which may occur during the different steps of the circuit life cycle (fabrication, post-treatment, test, assembly, etc.).

2.2.4 LTCC technology limitations

As any fabrication technology, LTCC has some limitations which should be highlighted and addressed, when possible, to obtain the best functional RF circuits. Among the known problems that may occur in an LTCC fabrication, we mention:

- **Bad conductor screen printing:** Printed shapes may be different of the desired lines. This occurs often for the thinnest ones (less than 100 μm). It results on wrong size (and so wrong impedance and electrical length) and/or potential open or short circuits. Machine parameters should be set properly to avoid such problem. Laser ablation may also present a solution to correct the lines' shapes.
- **Bad via filling:** Depending on the vias' diameter, layer thickness, and the conductor paste viscosity, some vias may still be empty or only partially filled after via filling. To avoid such problems, an inspection of the important vias should be performed for each layer. If some vias hole are empty, we may change the filling parameters (time, vacuum, paste viscosity, etc.) or proceed with a manual filling.
- **Shrinkage:** After lamination and sintering, LTCC material shrink in the x, y and z directions. Shrinkage factors vary according to the ceramic used and they are always provided by the manufacturer. However, small variation may occur between rolls and lots

of material. Precise measurement of sample prototypes before the final fabrication can be used to adjust the shrinkage values and generate the exact circuit's dimensions.

- **Layer misalignments:** Layer to layer misalignment is a typical problem in LTCC technology. It is due to misalignment errors during the screen printing, layers rotation and manual stacking. It can result in bad via connections or discontinuous interconnections. Good alignment patterns, sophisticated stacking tools and experienced operator are required to reduce misalignment errors.
- **Substrate deformation:** geometry deformation may result during the co-firing step. A bad temperature profile or non-compatible materials, like those with large expansion coefficients, are generally the origin of such deformation.

2.3 LTCC for reconfigurable RF components

2.3.1 LTCC for fluidic reconfigurable RF components

As electromagnetic waves are sensitive to the propagation environment, it is possible to alter the responses of RF and microwave circuits by changing their surrounding material. Integrating fluidic channels around these structures with the ability to inject/ extract different dielectric liquids having high permittivity results in a change of the overall effective dielectric constant (Entesari & Saghati, 2016). Hence, the same circuit may generate multiple responses leading to a reconfigurable functioning. Figure 2.3 illustrates an example of a microstrip transmission line loaded with a fluidic channel underneath (Brown, Goode, & Saavedra, 2018).

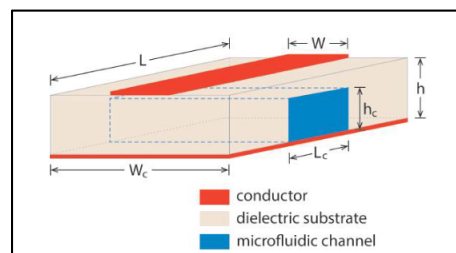


Figure 2.3 Microstrip transmission line with a fluidic channel
Taken from Brown et al (2018)

Fluidic channels are integrated into solid substrates using complex methods and techniques as etching, molding, lamination, etc. (Pinon et al., 2012). LTCC, with its inherent 3D nature and its ability to realize buried cavities, allows adding fluidic cavities (or channels) to RF structures through few and easy standard fabrication steps. Unlike the commonly used techniques which are limited to form small size and standard profile channels, numerous channels with varying shapes, sizes and positions are feasible in a LTCC process. Hence, reconfigurability of RF circuits down to low frequencies is possible with this technology. Furthermore, since the ceramic is fired at a temperature of around 850 °C, liquids injected into the preformed channels are immune to permeability and chemical reaction issues.

As any emerging technology, issues and concerns raised while integrating fluidics into electronics components, should be resolved. The fabrication process, and particularly steps related to forming cavities, should be adjusted to match the targeted fluidic channels design and integrity. Moreover, employed dielectric fluids have to be selected carefully with respect to their electronics characteristics to avoid degrading reconfigurable microwave circuits' performance. For example, liquids with dielectric constants close to that of the solid substrate lead to limited reconfigurability. Also, high loss liquids significantly degrade circuits' performance, specifically at microwave frequencies. Due to their chemical nature, low loss liquids with a specific range of dielectric constants are sometimes hard to find.

2.3.2 LTCC for MEMS reconfigurable RF components

RF-MEMS are micro elements that perform mechanical movements to realize RF functionality based on external actuation (electrostatic, magnetostatic, piezoelectric or thermal). Although it is a relatively recent technology, it has become very useful in realizing tunable RF and microwave devices (Rebeiz, 2004). MEMS devices are manufactured using surface or bulk micromachining techniques (Rebeiz, 2004). They can be built on planar or multilayer substrates. They are linear devices with low distortion. They also provide low insertion loss, high isolation and low power consumption up to very high frequencies (Rebeiz, 2004). Figure 2.4 shows a generic view of an RF MEMS switch (Haghshenas, Ghobadi, Nourinia, Ahmadian,

& Soltani, 2011). It consists of a suspended bridge over an RF transmission line, a coplanar waveguide in this case.

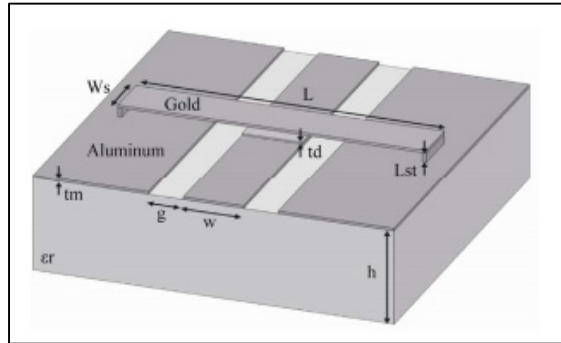


Figure 2.4 RF MEMS switch view
Taken from Haghshenas et al. (2011)

LTCC as a substrate for RF MEMS switches is of a great interest since it allows the development of a new generation of reconfigurable, and potentially smart RF circuits and systems. Indeed, known with its low thermal expansion coefficient and high mechanical strength, LTCC's mechanical and thermal properties are therefore compatible with several materials including most of those employed in MEMS technology. Consequently, in the addition to the LTCC advantages listed in section 2.2.2, we predict that many goals can be gained from combining these two technologies, mainly:

- LTCC technology is a high dielectric constant, 3D technology where most of the passive structures are buried on a multilayer stack-up substrate. Therefore, the fabricated circuits are miniaturised compared to their counterparts built on planar substrate.
- DC control circuits for MEMS devices can be integrated in the inner LTCC layers, leading to simplified design and further miniaturization.
- Highly integrated RF-MEMS-based tunable components with reduced number of external interconnections and transitions are feasible. Consequently, losses related to assembly techniques are reduced and the obtained RF performance are enhanced accordingly.
- LTCC can be used as both a substrate and a package for MEMS based tunable devices. This way, no additional protection is required for MEMS movable elements.

However, taking advantage of combining LTCC and MEMS technologies is not easily feasible, due in large part to three main factors. First, it requires access to both LTCC and MEMS processes, which is not readily available for most researchers. Second, there are inherent challenges posed by the sintered LTCC substrate's planarity, roughness and uniformity, which prohibit the growth of continuous thin layers needed for the development of MEMS elements. Third, the effects of the materials and chemicals used in MEMS processes on LTCC substrates are still ambiguous and require intensive investigations for the choice of the most compatible and appropriate ones.

2.3.3 Fluidic and MEMS tuners and RF amplifiers in LTCC technology

Leveraging LTCC capabilities and its compatibility with fluidic and MEMS technologies, we propose employing this technology to build novel types of fluidic and MEMS tunable devices. In this context, we propose two different solutions to produce reconfigurable impedance tuners, and thereby flexible amplifiers with enhanced RF performances. While the first one exploits the LTCC ability to integrate fluidic cells (realized with transmission lines and fluidic channels) inside the substrate (figure 2.5-a), the second uses RF MEMS switches developed directly on the LTCC surface (figure 2.5-b). Each fluidic cell and RF MEMS switch provides at least two different responses thus enabling reconfigurability. As shown in figure 2.5, mounted components (transistors, capacitors, resistors, etc.) and control circuits (bias, inlets/outlets, etc.) are supported by the same LTCC substrate, and they can be added either on the outer or inner layers. With these architectures, we may reach the overall objective of this thesis, i.e., demonstrate the feasibility of reconfigurable impedance tuners that serves as flexible matching networks for RF amplifiers. Unlike most of the published works targeting high frequency reconfigurable RF circuits, we focus on medium and high frequency applications, and we target frequencies down to 0.9 GHz and 2GHz for the fluidic and the MEMS solutions, respectively.

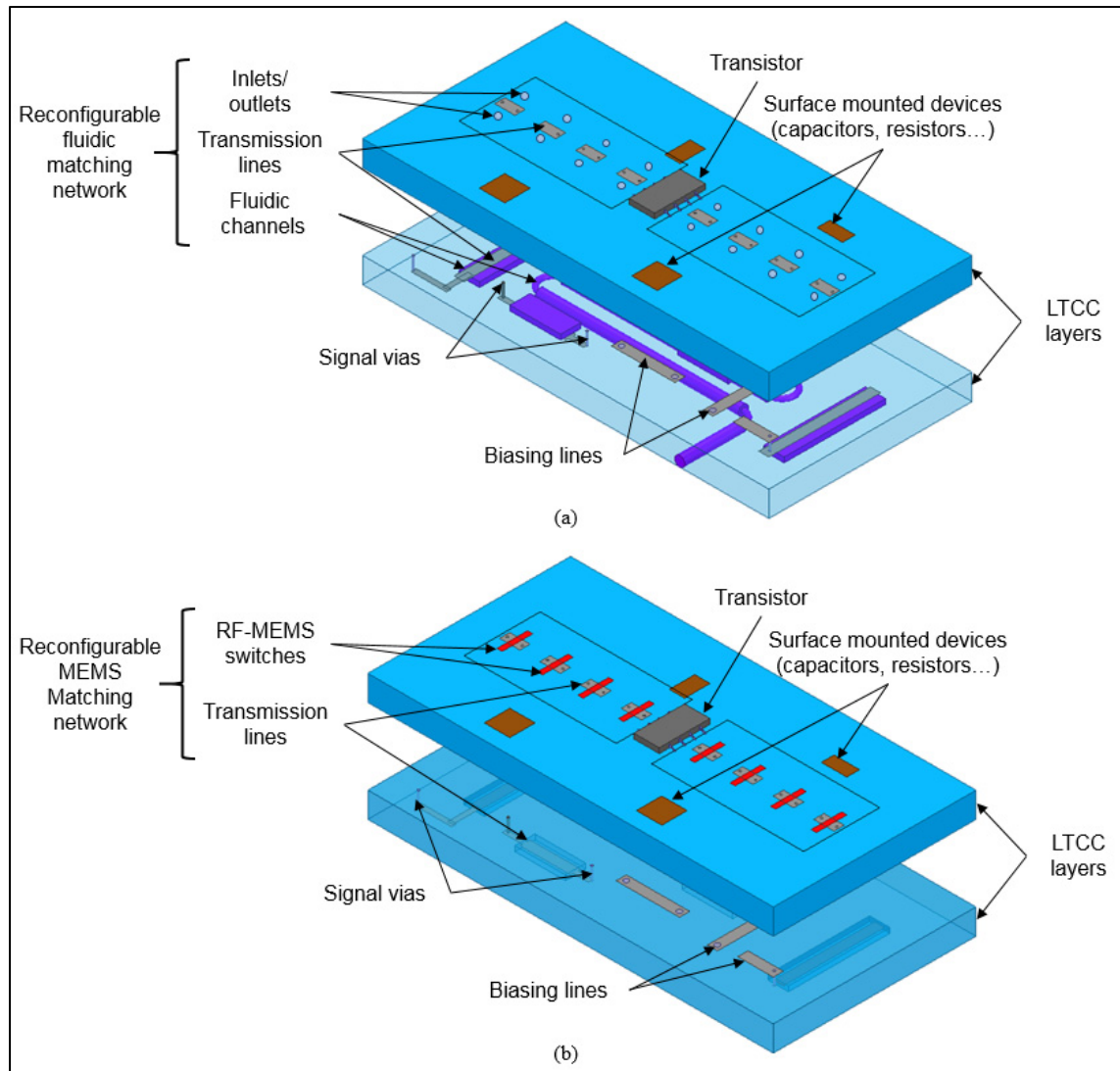


Figure 2.5 Exploded 3D view of a reconfigurable RF amplifiers with tunable matching networks realized with: a) fluidic architecture and b) MEMS architecture

2.4 Conclusion

An overview about the LTCC technology and its associated benefits and limitations were introduced. A description of LACIME in-house LTCC process was also detailed to provide an idea about the typical fabrication steps. Perspectives for combining LTCC with fluidic and MEMS technologies to build reconfigurable tuners and RF amplifiers were discussed.

FLUIDIC AND MEMS RECONFIGURABLE RF IMPEDANCE TUNERS' DESIGN

3.1 Introduction

As explained in the first chapter, it is challenging to find an RF impedance tuner able to provide wide impedance coverage, particularly at low frequencies. In this chapter, we propose RF fluidic (Bahloul & Kouki, 2020) and MEMS based tuners in a 3D LTCC substrates. The operation principle of the proposed tuners is first presented. Next, single fluidic cell and MEMS-on-LTCC switch designs are elaborated based on analytical expressions for impedance calculation and EM simulations. 8-cell LTCC fluidic and planar MEMS-on-LTCC impedance tuners are then designed. The fluidic tuner is designed to cover the 0.9 to 2.4 GHz band while the MEMS tuner is designed to operate between 2 and 9 GHz. Miniaturised 3D design iterations of the planar tuner is also presented taking full advantage of LTCC's unique integration capability. The chapter is concluded with a comparative study of the performance of the designed tuners with those in the open literature. Fabrication and measurements makes the subject of the next chapters.

3.2 Impedance tuners' design approach

Reconfigurable impedance matching networks (or tuners) present a promising alternative to fixed ones in the design of reconfigurable amplifiers as they can offer multiple impedances at different frequency bands. In this project, we consider distributed impedance tuners consisting of a cascade of N identical uniformly distributed two-state RF cells, C_1 - C_N , as shown in figure 3.1-e. The i^{th} cell, C_i , has a characteristic impedance Z_{ci} and an electric length E_{L_i} . When the cell is in state 1, its characteristics are ($Z_{ci} = Z_1, E_{L_i} = E_{L_1}$) whereas when it is under state 2 it is characterized by ($Z_{ci} = Z_2, E_{L_i} = E_{L_2}$). In this work, we are interested in the scenario where the tuner is loaded with a 50Ω impedance and Z_1 is set to 50Ω in a 50Ω system such that when all cells are in state 1, we simply have a 50Ω line. Consequently, for a given combination of cell states, the resulting impedance Z_{in} consists of successive movements on the circles

centered on Z_1 and Z_2 by an electrical length EL_1 and EL_2 , respectively, starting from the Smith chart center, as shown in figure 3.1-f. For instance, the 1-cell (figure 3.1-a) and 2-cell tuners (figure 3.1-c) result on 2 and 4 different input impedances as depicted in figure 3.1-b and d. Therefore, as an asymmetric device, the tuner is expected to synthesize 2^N input impedances (Z_{in}) at each frequency (figure 3.1-f).

Based on the N-cell tuner coverage illustrated in figure 3.1-f, a wide coverage at a particular frequency corresponds to one where the 2^N synthesized impedances are distributed throughout the Smith chart covering low and high reflection coefficients. Here, we define the impedance ratio R and the tuner's total electric length EL_t by:

$$R = \frac{Z_1}{Z_2} \quad (3.1)$$

$$EL_t = N \cdot EL_1 \quad (3.2)$$

To synthesize impedances with high reflection coefficients, i.e., close to the Smith chart edge, Z_2 should be minimized and losses should be reduced. Therefore, for a Z_1 set to 50Ω , we seek to increase R . We note also that the generated impedances Z_{in} are located within a region of the Smith chart limited by EL_t as shown in figure 3.1-b. For values of EL_1 and N where EL_t is close to a multiple of half wavelength ($\lambda/2$), a large coverage with well distributed impedances is expected. However, this condition may be satisfied only for some frequencies in a targeted frequency band. Apart from its impact on EL_t , the cells number N also controls the coverage resolution, i.e., a low value leads to scattered impedances points while a high one leads to a crowded coverage with a larger size and an increased complexity. Therefore, the tuner's coverage depends on two factors: the cells' electrical parameters and their number.

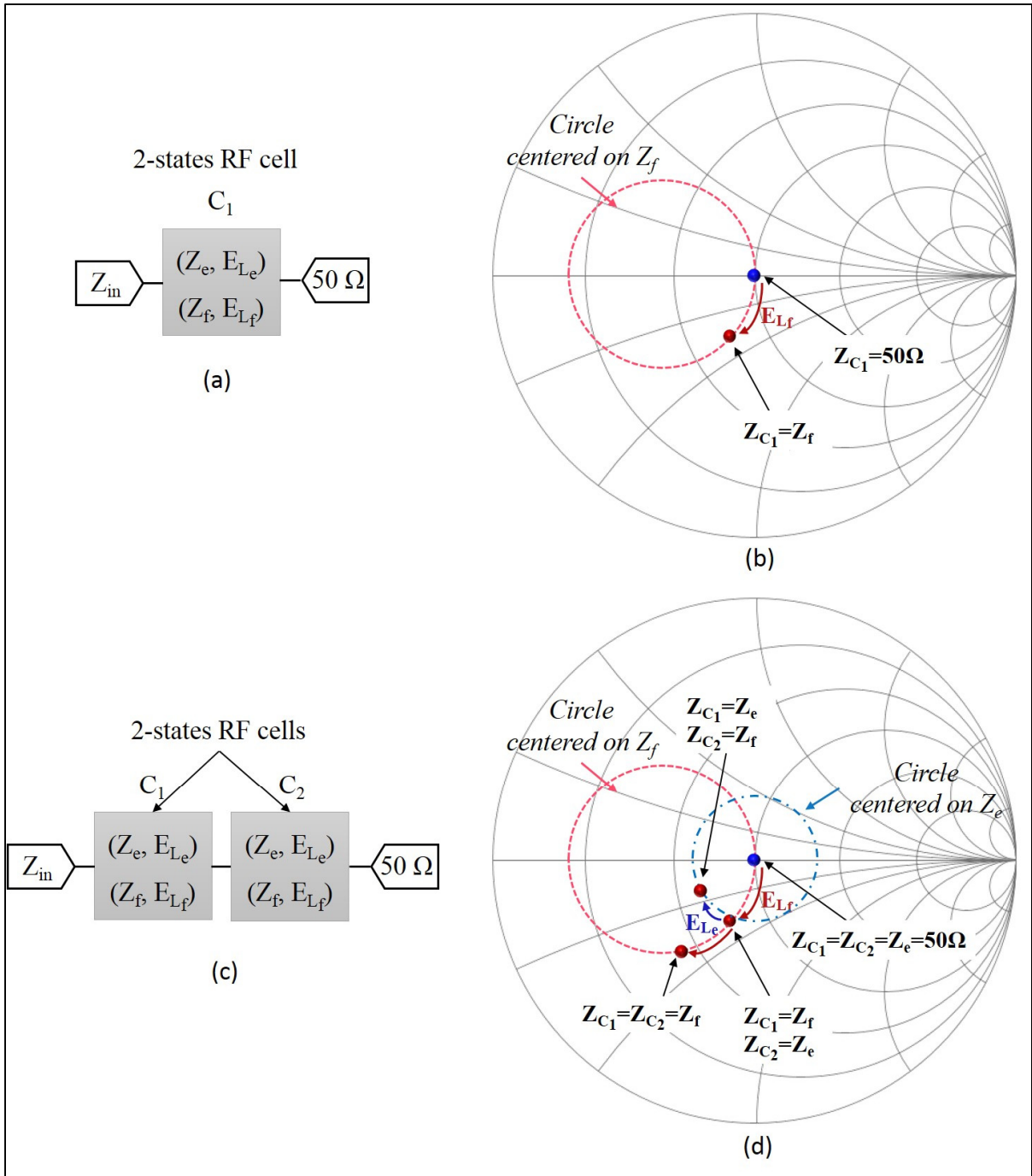


Figure 3.1 Impedance tuner operation principle: a) 2-state RF cell illustrative scheme, b) 2-state RF cell illustrative Smith chart coverage, c) two 2-state RF cell illustrative scheme, d) two 2-state RF cell illustrative Smith chart coverage, e) N 2-state RF cell illustrative scheme, f) N 2-state RF cell illustrative Smith chart coverage

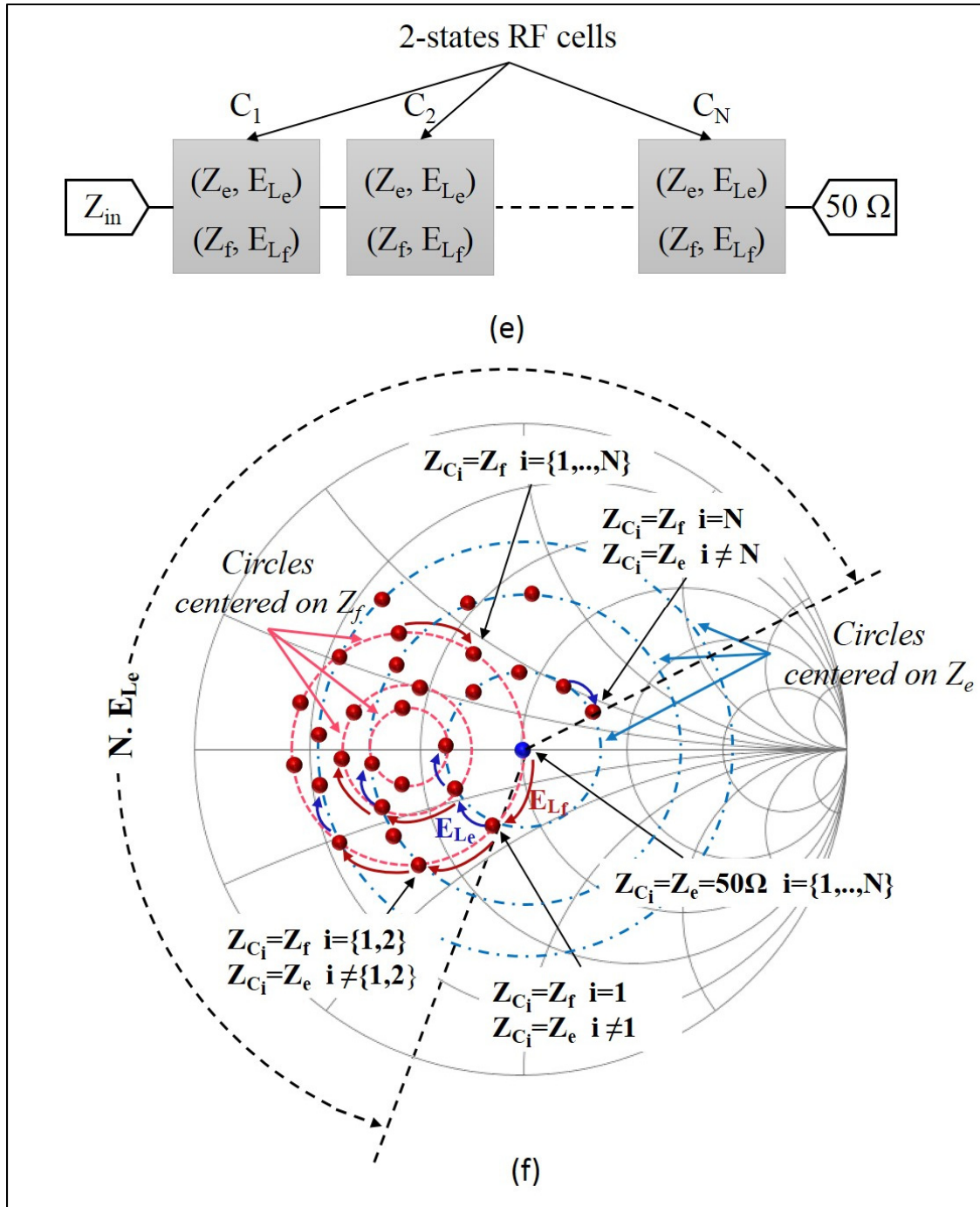


Figure 3.2 Impedance tuner operation principle: a) 2-state RF cell illustrative scheme, b) 2-state RF cell illustrative Smith chart coverage, c) two 2-state RF cell illustrative scheme, d) two 2-state RF cell illustrative Smith chart coverage, e) N 2-state RF cell illustrative scheme, f) N 2-state RF cell illustrative Smith chart coverage (continued)

In the next sections, we propose two different configurations of impedance tuners based on the distributed architecture of figure 3.1-a, where the individual cells are made of fluidic elements or MEMS switches. Our goal is not only to offer a wide Smith chart coverage, but also to cover both low and high frequencies, while improving RF performance, enabling integration with other RF circuits and reducing fabrication complexity.

3.3 LTCC based fluidic tuner

In this section, we propose the design of a new RF fluidic impedance tuner in a 3D LTCC substrate for RF frequency applications. To do so, the design of a single fluid cell is detailed with new analytical expressions for impedance calculation. Then, we introduce an 8-cell LTCC fluidic impedance tuner covering the 0.9 to 2.4 GHz frequency range. Its coverage is characterised based on EM simulations.

3.3.1 Fluidic RF cell design

3.3.1.1 General overview

Figure 3.2 shows a 3D view of the proposed 2-state RF fluidic cell. It is implemented in a multilayer LTCC substrate. It consists of a grounded coplanar waveguide (CPWG) transmission line buried into an LTCC multilayer substrate with an empty cavity, i.e., channel, above a part of the line (figure 3.2-a). An inlet and an outlet, to inject/extract the desired gas or liquid, along with two tapered transitions, for on-wafer probe measurement, are also integrated in the cell design.

Considering figure 3.2-b, where a cross-section of the fluidic cell with various dimensions is illustrated, this structure can be modeled by 5 transmission line sections, S1-S5, with different parameters as shown in figure 3.2-c. Sections S1 and S5 represent the tapered transitions corresponding to conventional CPWG transmission lines over an h_1 -thick substrate. Sections S2 and S4 correspond to CPWG lines where the coplanar plane is sandwiched between two

dielectrics with thicknesses of h_1 and h_2 , respectively. Section S3 represents the reconfigurable part and consists of a CPWG line covered by a double layer dielectric: solid dielectric over an h_c -thick cavity filled with air or liquid dielectric. The whole structure is surrounded by air.

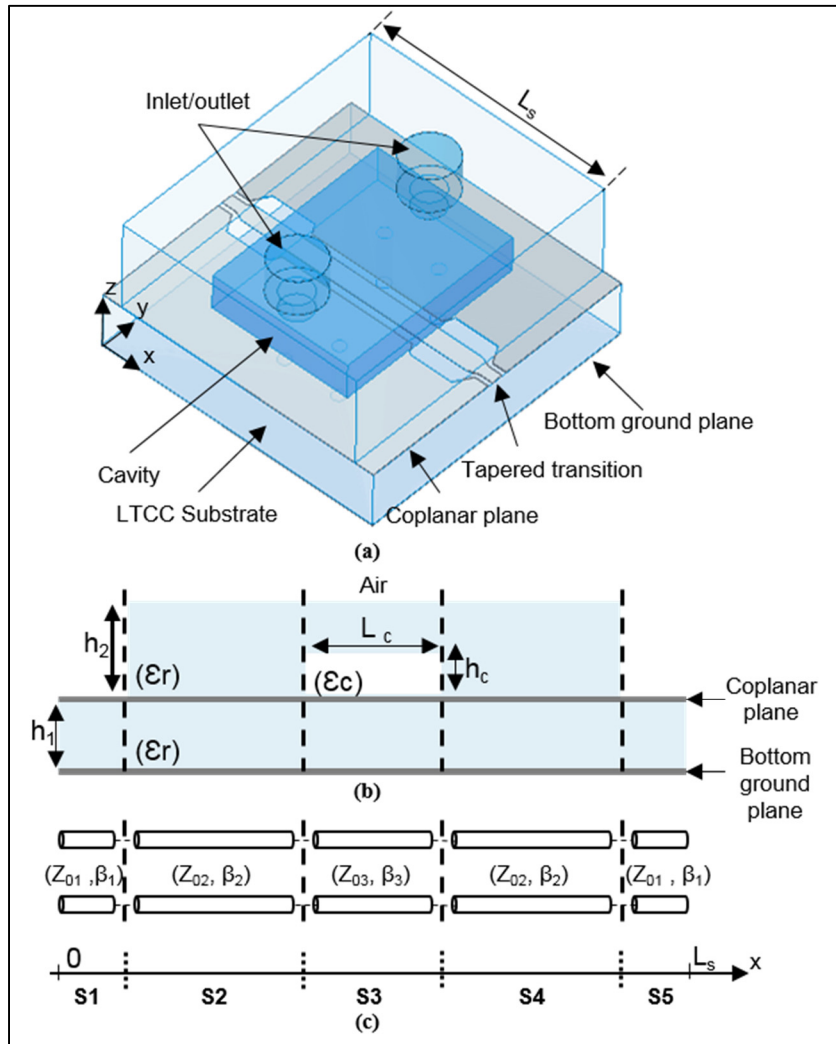


Figure 3.2 Two-state RF fluidic cell: a) 3D view, b) cross section view and c) transmission lines model

Reconfigurability of the proposed RF fluidic cell is accomplished through section S3 of figure 3.2-b by changing the fluidic content of its cavity, thereby varying the dielectric constant ϵ_c . This results in changing the propagation constant, β_3 , as well as the characteristic impedance, Z_{03} , for section S3 as shown in figure 3.2-c. Therefore, based on the fluid filling the S3 cavity and its length L_c , the equivalent impedance and the electrical length of the complete fluidic cell

can be toggled between the two states (Z_1, E_{L1}) and (Z_2, E_{L2}) . Here, we identify the empty and fluidic-full states by their electrical characteristics $(Z_1 = Z_e, E_{L1} = E_{Le})$ and $(Z_2 = Z_f, E_{L2} = E_{Lf})$ respectively.

3.3.1.2 Model parameters and dimensioning

As shown in figure 3.2, the five sections of the fluidic cells represent various CPWG line segments of varying geometries and dielectric stacking. For sections S1 and S5, conventional CPWG line closed form models exist and are commonly accessible in various software tools. However, sections S2, S3, and S4 are not conventional CPWG lines and no models for calculating their characteristics exist. Therefore, the conformal mapping technique detailed in (Simons, 2001) is applied to these sections, as Q-TEM (Quasi-Transverse ElectroMagnetic) structures, to derive the expressions for effective dielectric constants, ϵ_{eff} , and characteristic impedances, Z_0 :

$$\epsilon_{eff} = 1 + \frac{(\epsilon_r - 1)\left(\frac{K(k_1)}{K(k'_1)} + \frac{K(k_2)}{K(k'_2)}\right) + (\epsilon_{up} - \epsilon_r)\frac{K(k_c)}{K(k'_c)}}{\frac{K(k_3)}{K(k'_3)} + \frac{K(k)}{K(k')}} \quad (3.3)$$

$$Z_0 = \frac{60\pi}{\sqrt{\epsilon_{eff}\left(\frac{K(k_3)}{K(k'_3)} + \frac{K(k)}{K(k')}\right)}} \quad (3.4)$$

where

$$\epsilon_{up} = \begin{cases} \epsilon_r & \text{for } S2 \text{ and } S4 \\ \epsilon_c & \text{for } S3 \end{cases} \quad (3.5)$$

$$k = \frac{W}{W + 2.G} \quad (3.6)$$

$$k_i = \frac{\text{Sinh}[\pi.W / (4.h_i)]}{\text{Sinh}[\pi.(W + 2.G) / (4.h_i)]}; i = \{1, 2, c\} \quad (3.7)$$

$$k_3 = \frac{\text{Tanh}[\pi.W / (4.h_1)]}{\text{Tanh}[\pi.(W + 2.G) / (4.h_1)]} \quad (3.8)$$

$$k'_i = \sqrt{1 - k_i^2}; i = \{1, 2, 3, c\} \quad (3.9)$$

$K(\cdot)$ is the complete elliptic integral of the first kind, ϵ_r is the LTCC's relative permittivity, W and G are the CPWG center conductor width and gap, respectively.

As stated in section 3.2, we should increase R for wide reconfigurability. Considering the fixed physical parameters of the different sections, this can be achieved through a wide change in ϵ_c , resulting on generating the highest change in Z_{03} , and β_3 . To quantify this change, we introduce the impedance ratio r_z and the propagation ratio r_β as follow:

$$r_z = \frac{Z_{03}(\epsilon_c = 1)}{Z_{03}(\epsilon_c = \epsilon_{rliquid})} \quad (3.10)$$

$$r_\beta = \frac{\beta_3(\epsilon_c = \epsilon_{rliquid})}{\beta_3(\epsilon_c = 1)} \quad (3.11)$$

where we require that $Z_{03}(\epsilon_c = 1) = 50\Omega$. We further require that $Z_{01} = Z_{02} = 50\Omega$. In this manner, the fluidic cell presents a 50Ω impedance (Z_e) if the cavity is empty. Equations (3.3)-(3.9) are used to determine the dimensions for each section that meet these requirements. Here we used multiple layers of DuPont 951 for the computations. With six 4.5-mil layers for h_1 , ten 4.5-mil layers for h_2 and four 4.5-mil layers for h_c , the initial dimensions of the CPWG line for each section are calculated based on the substrate characteristics detailed in table 3.1 and are as given in table 3.2.

Table 3.1 DuPont 951 characteristics

| Parameter | Value |
|--|---------|
| Dielectric constant: ϵ_r | 7.8 |
| Dielectric tangent loss: $\tan\delta$ | 0.006 |
| Layer thickness (before shrinkage) (mil) | 4.5; 10 |

Table 3.2 CPWG sections initial dimensions

| Sections | S1 and S5 | S2 and S4 | S3 |
|--|-----------|-----------|-----|
| CPWG center conductor width: W (μm) | 118 | 200 | 200 |
| CPWG gap: G (μm) | 48 | 180 | 79 |

Once the initial dimensioning is completed, the ratios r_z and r_β , are determined by the choice of $\epsilon_{r_{liquid}}$. For maximum ratios, and hence maximum reconfigurability, high values of $\epsilon_{r_{liquid}}$ must be chosen. Here, deionized (DI) water is chosen as the filling fluid given its high relative permittivity. Based on Debye's formula (Andryieuski, Kuznetsova, Zhukovsky, Kivshar, & Lavrinenko, 2015) and considering a room temperature of 20 °C, the DI water's relative permittivity and loss tangent may be calculated using:

$$\epsilon_{r_{water}} = 6.28 + \frac{73.91}{1 + 0.26 \cdot 10^{-20} \cdot f^2} \quad (3.12)$$

$$\text{Tan } \delta_{water} = \frac{4.48 \cdot 10^{-9} \cdot f}{80.19 + 2.26 \cdot 10^{-20} \cdot f^2} \quad (3.13)$$

Equations (3.12) and (3.13) show that the DI water's dielectric constant decreases from 80 to 78.6, and its dielectric loss tangent increases from 0.05 to 0.14 when frequency varies from 0.9 GHz to 2.4 GHz. Using equations (3.3-3.4) and (3.12) to compute ϵ_{eff} and Z_{03} when the cavity is filled with DI water, then equations (2.10) and (3.11), to compute r_z and r_β , we obtain the results shown in table 3.3.

Table 3.3 Characteristics for S3 when empty and filled with DI water

| f (GHz) | Empty | | DI Water | | r_z | r_β |
|---------|-----------------------|-------------------|-----------------------|-------------------|-------|-----------|
| | Z_{03} (Ω) | β_3 (rad/m) | Z_{03} (Ω) | β_3 (rad/m) | | |
| 0.9 | 50 | 39.5 | 16.5 | 122 | 3.03 | 3.08 |
| 2.4 | 50 | 105 | 16.6 | 322 | 3.01 | 3.06 |

To complete the design of the fluidic cell, several (cavity length: L_c ; cell length L_s) combinations were considered and simulated. As we aim to minimize DI-water related loss while maintaining considerable change in the reflection coefficient, we selected an L_c of 1.5 mm and an L_s of 3 mm.

3.3.1.3 Simulated RF performance

Figure 3.3 shows the insertion loss and the complex reflection coefficient of this structure resulting from optimised HFSS 3D field simulation between 0.9 GHz and 2.4 GHz for both filled and empty cavity cases. As can be seen, when the cell is empty, it presents an input impedance of 50Ω whereas when DI-water is injected into the cavity, the cell impedance and its electrical length change and show variation with frequency. Consequently, a part of the signal is reflected, resulting in an increase on the insertion loss (figure 3.3-a) and a change in the reflection magnitude and phase (figure 3.3-b).

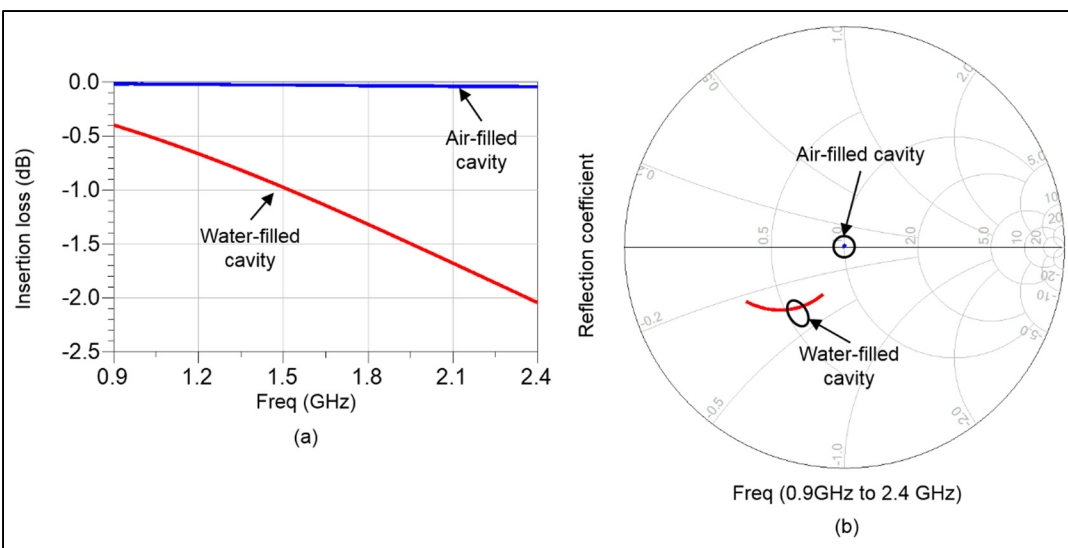


Figure 3.3 RF fluidic cell simulated: a) Insertion loss and b) reflection coefficient

3.3.2 Fluidic tuner

Eight fluidic cells were cascaded to form the tuner as shown in figure 3.4. Two $50\ \Omega$ vertical CPW transitions to upper CPWG lines were added at the input and output for easy measurement of the fabricated device. The overall tuner size, including the vertical transitions, is $26\ \text{mm} \times 10\ \text{mm} \times 1.5\ \text{mm}$.

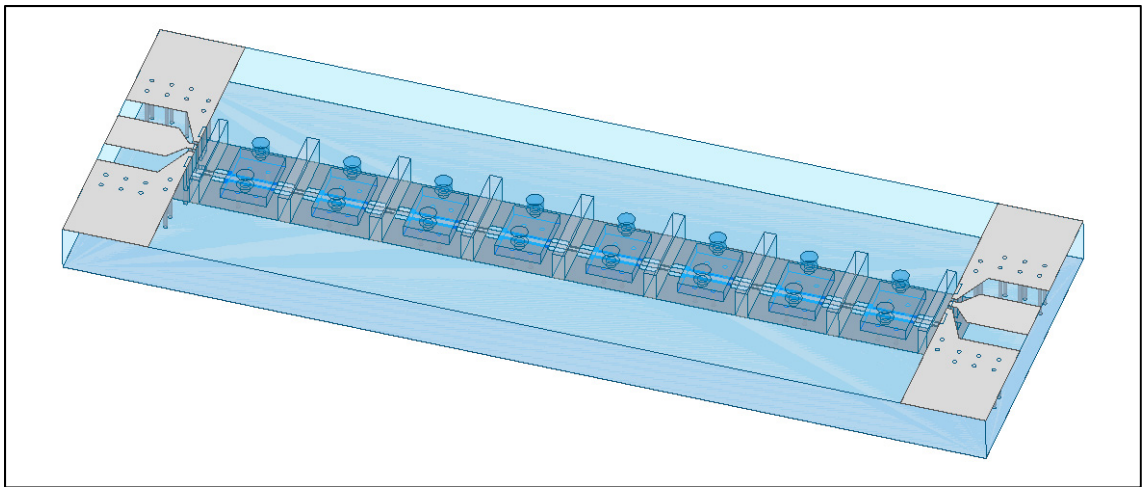


Figure 3.4 Fluidic tuner 3D view

To simulate the impedance coverage of the proposed tuner, 256 (2^8) states must be modeled and simulated. Given that the cells are identical, we can reduce the complexity of field simulations by cascading 8 identical two-port S-parameters data items in the ADS software. Each data item contains the 2×2 S-matrix obtained by 3D field simulation using HFSS for both the empty and DI water-filled states over the $[0.9\ \text{GHz} - 2.4\ \text{GHz}]$ frequency band. Two data items containing the field simulated S-parameters for the vertical transitions are also added to ADS circuit.

Figure 3.5 shows the obtained input impedances when the output port is terminated by a $50\ \Omega$ load. As can be seen, the tuner offers reasonable coverage of the Smith chart, particularly at higher frequencies. However, the coverage tends to be concentrated away from the edge of the Smith chart. This is attributed to the value of the fluidic cell's impedance Z_f that depends

basically on the fluid parameters. Indeed, substituting DI-water with a liquid characterized by higher dielectric constant and lower dielectric loss results on more spread coverage. Furthermore, as we cannot satisfy a total tuner length EL_t of $\lambda/2$ for all the frequencies between 0.9 GHz and 2.4 GHz, the impedance coverage is not evenly distributed throughout the Smith chart at low frequencies (0.9 GHz and 1.2 GHz). Increasing the unit cell's length to enhance the tuner coverage at those frequencies is not recommended for such periodic structure because it results on decreasing the Bragg frequency (T. Vähä-Heikkilä & Rebeiz, 2004), i.e. the frequency where the transmission ceases. No coverage can be provided at higher frequencies (higher than 2 GHz) in this case.

Still, despite the retracted coverage, the impedance matching capability of the proposed tuner is quite good even at such low frequencies. In fact, based on equation 3.14 as introduced in (Domingue, Fouladi, et al., 2009), each point in the Smith chart, representing ideal matching with a given tuner state, would become a circle if lower matching level are permitted. For example, an impedance coverage area larger than the 256 individual points is reached at 10 dB matching level at the considered frequencies, as shown in figure 3.6. Moreover, this tuner can be used in most circuits (amplifiers, filters, etc.) tuning in combination with other fixed pre-matching circuits that can be bring the required impedances within the tuner constellation.

$$\Gamma_{in} = \frac{\Gamma_s - S_{11}}{\Gamma_s S_{11} - 1} \quad (3.14)$$

where Γ_{in} is the reflection coefficient at the required matching level Γ_s is the reflection coefficient at a particular point in the Smith chart and S_{11} is the reflection coefficient at a point from the tuner constellation.

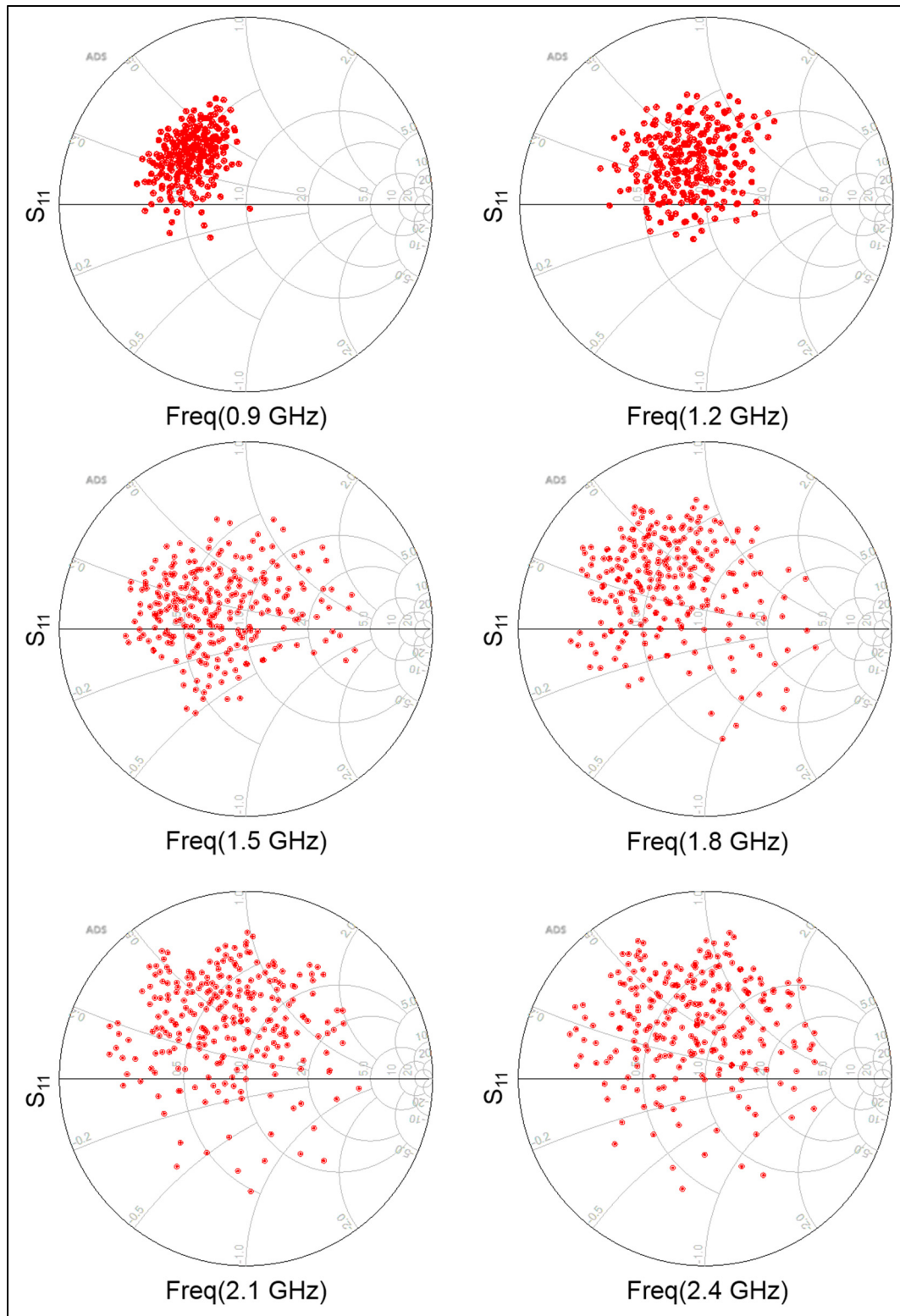


Figure 3.5 Fluidic tuner simulated Smith chart coverage at different frequencies between 0.9 GHz and 2.4 GHz

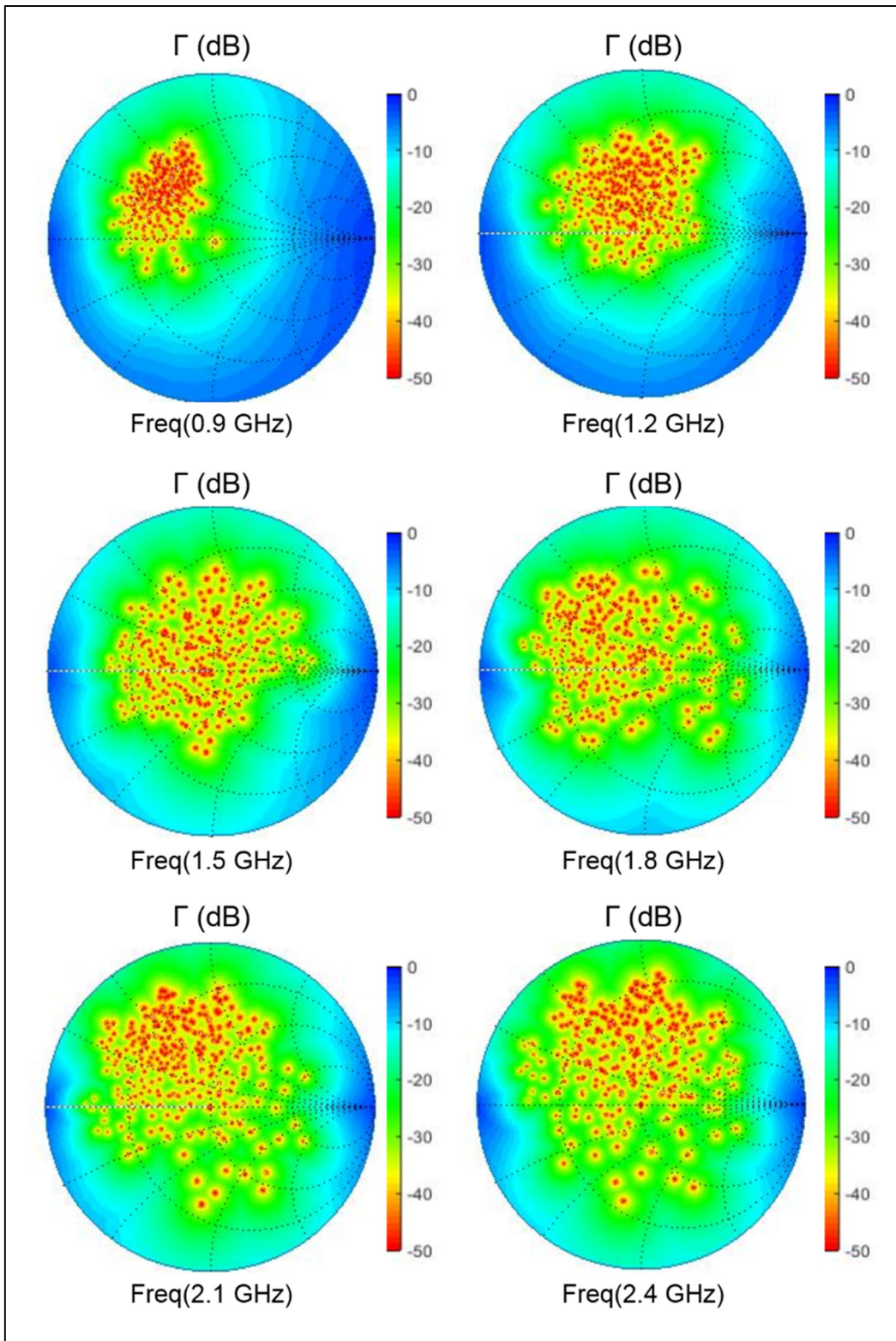


Figure 3.6 Fluidic tuner simulated reflection coefficient over the gamma plane at different frequencies between 0.9 GHz and 2.4 GHz

3.4 MEMS-on-LTCC tuner

In this section, we introduce, for the first time, the design of an RF MEMS-on-LTCC impedance tuner. Here, the 2-state RF cell is an RF MEMS switch built on LTCC substrate. It is designed based on analytical equations and EM simulation. This switch is then used to make an 8-cell tuner operating between 2 GHz and 7 GHz. Both uni-planar and 3D designs of the tuner are considered.

3.4.1 MEMS-on-LTCC RF switch

3.4.1.1 General overview

An RF MEMS switch is the building block of the MEMS-on-LTCC tuner. As detailed in figure 3.7-a, we consider a capacitive RF MEMS switch with lateral actuation, built directly on the surface of an LTCC substrate. Here, biasing circuits are not shown, and dimensions are not uniformly scaled through the x, y and z axis. In this section, we focus only on the required parameters to design an RF tuner with wide impedance coverage operating for both low and high frequencies. The fabrication process, electrical and mechanical performance of the MEMS-on-LTCC switch are detailed in chapter 4.

Figures 3.7-b and 3.7-c show the top and side views of the MEMS cell with various dimensions. It is composed of a movable membrane over a CPW transmission line. A dielectric layer covering the transmission line is used for isolation purposes. When an independent biasing voltage is applied through two DC actuation pads, the membrane moves from an up state to a down state resulting in a change of the switch equivalent capacitance. This structure can be modeled by 2 transmission line sections with a parallel 2-state capacitance (C_{MEMS}) as shown in figure 3.7-d. C_{MEMS} is the reconfigurable element of the MEMS cell as it causes the variation of its equivalent impedance Z_s and electrical length E_{L_s} , thereby producing two different states: an upstate characterised by ($Z_1 = Z_{up}$, $E_{L_1} = E_{L_{up}}$) and a down state corresponding to ($Z_2 = Z_{dn}$, $E_{L_2} = E_{L_{dn}}$).

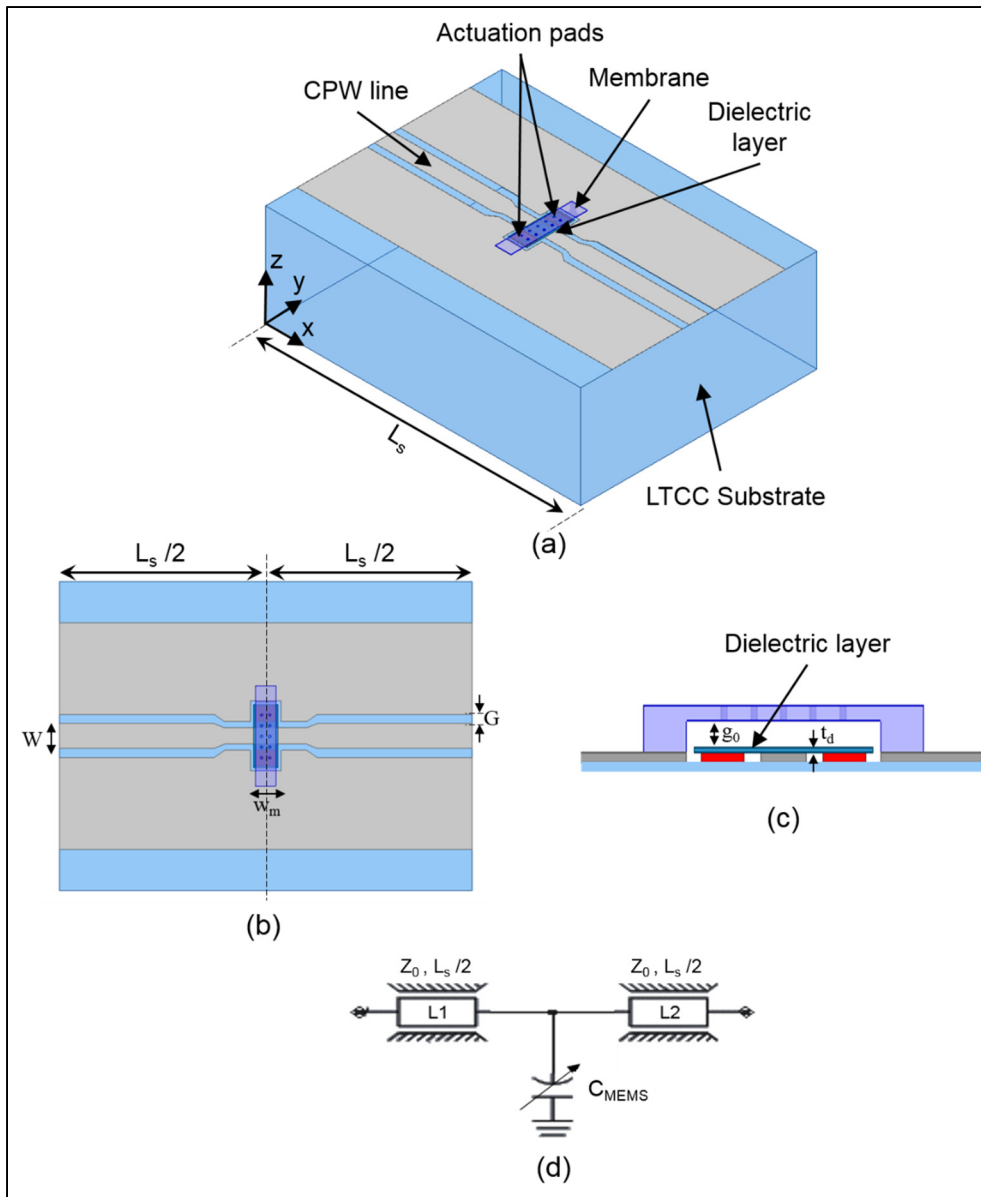


Figure 3.7 RF MEMS-on-LTCC switch: a) 3D view, b) top view, c) side view and d) model

3.4.1.2 Model parameters and dimensioning

Aside from the CPW line's properties (characteristic impedance Z_0 , substrate effective dielectric constant ϵ_{eff} , and the cell physical length L_s), the capacitance value C_{MEMS} has the most important effect on the tunable behavior of the MEMS-on-LTCC switch as it may present two different values for the up and down states. It affects both the MEMS switch equivalent

impedance Z_s and the effective dielectric constant ϵ_{eff-s} , or equivalently the electrical length E_{Ls} , as explained in (Domingue, Fouladi, et al., 2009):

$$Z_s = \frac{Z_0}{\sqrt{L_F}} \quad (3.15)$$

$$\epsilon_{eff-s} = \epsilon_{eff} \cdot L_F \quad (3.16)$$

$$E_{Ls} = \frac{360 \cdot L_s}{c} \cdot f \cdot \sqrt{\epsilon_{eff-s}} \quad (3.17)$$

$$L_F = 1 + \frac{c \cdot Z_0 \cdot C_{MEMS}}{L_s \cdot \epsilon_{eff}} \quad (3.18)$$

where c is the light speed, f is the operating frequency and L_F is a loading factor.

Based on the L_F formula (equation (3.18)) and equations (3.15) to (3.17), the MEMS capacitance, C_{MEMS} , on both states, increases the characteristic impedance and decreases the electrical length of the bare CPW transmission line (unloaded line) for both states. Rebeiz (2004) provides its associated formulas at both the up ($C_{MEMS-up}$) and down states ($C_{MEMS-down}$) as follows:

$$C_{MEMS-up} = \frac{\epsilon_0 \cdot W \cdot w_m}{g_0 + t_d / \epsilon_d} + C_{FF} \quad (3.19)$$

$$C_{MEMS-down} = \frac{\epsilon_0 \cdot W \cdot w_m}{t_d / \epsilon_d} \quad (3.20)$$

where ϵ_0 is the permittivity of vacuum, W is the width of the CPW line, w_m is the width of the membrane, g_0 is the gap, t_d and ϵ_d are the thickness and the relative permittivity, respectively of the dielectric layer, and C_{FF} is the fringing field capacitance.

Similar to the fluidic cell, the MEMS-on-LTCC switch should present 50Ω at the initial state, i.e., when the membrane is in the up position. Considering equation (3.19) and based on the common physical properties of MEMS switches, the up-state capacitance has a value in the

femto-Farad range. Therefore, the loading factor value is approximately "1", and the characteristic impedance Z_{s-up} and the effective dielectric constant $\epsilon_{eff-s up}$ of the up state are around the unloaded line's Z_0 and ϵ_{eff} , respectively. The width (W) and the gap (G) of the CPW line are therefore chosen to provide the required 50Ω impedance on six 10-mil layers of DuPont951 and are detailed in table 3.5. As it can be seen in figure 3.7, although W and G may be kept constant, we opted for decreasing their values under the membrane while maintaining a Z_0 of 50Ω . This helps reducing the membrane's length for better mechanical performance (actuation voltage, stress, etc.) as detailed in chapter 4.

To ensure a high impedance ratio, R (as defined by equation 3.1), between the switch's two states that will lead to better impedance coverage on the Smith chart, the down state impedance Z_{s-down} should be decreased, while its associated electrical length $E_{Ls-down}$ should be increased. A high down state capacitance $C_{MEMS-down}$, i.e., a high capacitance ratio C_r , equation (3.21), is therefore required.

$$C_r = \frac{C_{MEMS-down}}{C_{MEMS-up}} \quad (3.21)$$

Considering the electrical and mechanical constraints of a shunt MEMS switch, further detailed in chapter 4, the membrane physical parameters are fixed and summarised in table 3.5. Aside from these parameters, the choice of the electrical length E_{L_s} significantly affects the functioning of the switch, and most importantly the tuner's impedance distribution and its operating frequency band. Depending on the physical length L_s (or the distance between two consecutive switches), as detailed in equation (3.17), most of the proposed researches (Papapolymerou et al., 2003; Tauno Vähä-Heikkilä et al., 2007) were constrained to high frequency tuners since the used technologies provides only small size features limiting L_s to few hundreds of microns. Equation (3.17) demonstrates also that E_{L_s} depends on the switch effective dielectric constant ϵ_{eff-s} . Some researchers employed complicated techniques to increase this parameter and, thus, increase E_{L_s} while maintaining miniaturised size, as in (Domingue, Fouladi, et al., 2009), where slow wave structures are used to build tuners for medium frequency applications. Taking advantage from the LTCC technology to build long

lines while respecting the Bragg frequency limit, we fix the length L_s to 3.4 mm, as shown in table 3.4 to provide functioning covering a large bandwidth of several GHz starting from low frequencies.

Table 3.4 RF MEMS-on-LTCC switch initial dimensions

| Parameter | Value |
|--|-------|
| W (μm) – away from membrane | 120 |
| W (μm) – under membrane | 80 |
| G (μm) – away from membrane | 48 |
| G (μm) – under membrane | 30 |
| w_m (μm) | 100 |
| g_0 (μm) | 2 |
| t_d (μm) | 0.3 |
| L_s (mm) | 3.4 |

Using SiO_2 ($\epsilon_d=3.9$) as material for the isolation layer, and considering a fringing capacitance component C_{FF} , typically estimated to be around 30 % of the up state capacitance (Rebeiz, 2004), $C_{MEMS-up}$ is around 44.3 fF and $C_{MEMS-down}$ is equal to 0.92 pF. This results in a C_r of 20.77. This value, constrained by the MEMS technology, leads to an R ratio of 1.4 as detailed in table 3.5. In this scenario, the electrical lengths at different states and frequencies, shown in table 3.5, are high enough to provide reconfigurability.

Table 3.5 MEMS-on-LTCC switch electrical parameters

| f (GHz) | Up state | | Down state | | R |
|---------|--------------------|----------------|--------------------|----------------|-----|
| | Z_s (Ω) | E_{Ls} (deg) | Z_s (Ω) | E_{Ls} (deg) | |
| 2 | 50 | 23 | 36.4 | 28.1 | 1.4 |
| 7 | 50 | 80.7 | 36.4 | 98.3 | 1.4 |

3.4.1.3 Simulated RF performances

Based on HFSS 3D field simulation, the MEMS-on-LTCC switch operation has been considered between 2 GHz and 7 GHz. Figure 3.8 shows its scattering parameters (insertion loss and complex reflection coefficient) for both up and down states. In the up state, the switch has an insertion loss of less than 0.3 dB (figure 3.8-a) up to 7 GHz with a good matching (figure 3.8-b), indicating thus an excellent RF signal transmission. Moving the membrane to the down state results in a change of the switch's impedance and its electrical length, leading to an insertion loss (or isolation) varying between 0.5 dB and 3.5 dB (figure 3.8-a) and a high reflection coefficient (figure 3.8-b). The obtained isolation range is sufficient despite its limited swing.

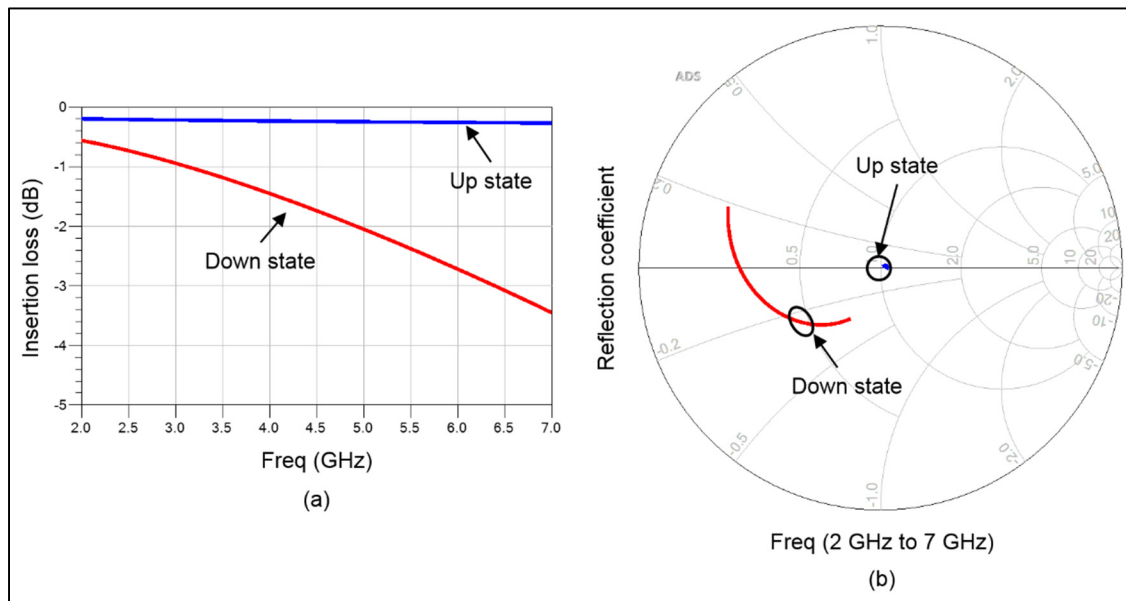


Figure 3.8 Field simulation of the MEMS-on-LTCC switch: a) insertion loss and b) reflection coefficient

3.4.2 MEMS-on-LTCC planar tuner

With the single switch's performance optimized, we proceed similarly to the fluidic tuner by cascading eight switches to form the MEMS-on-LTCC tuner shown in figure 3.9. Here, biasing circuits are hidden for clarity. The overall tuner size is 27.2 mm × 1.2 mm × 1.19 mm.

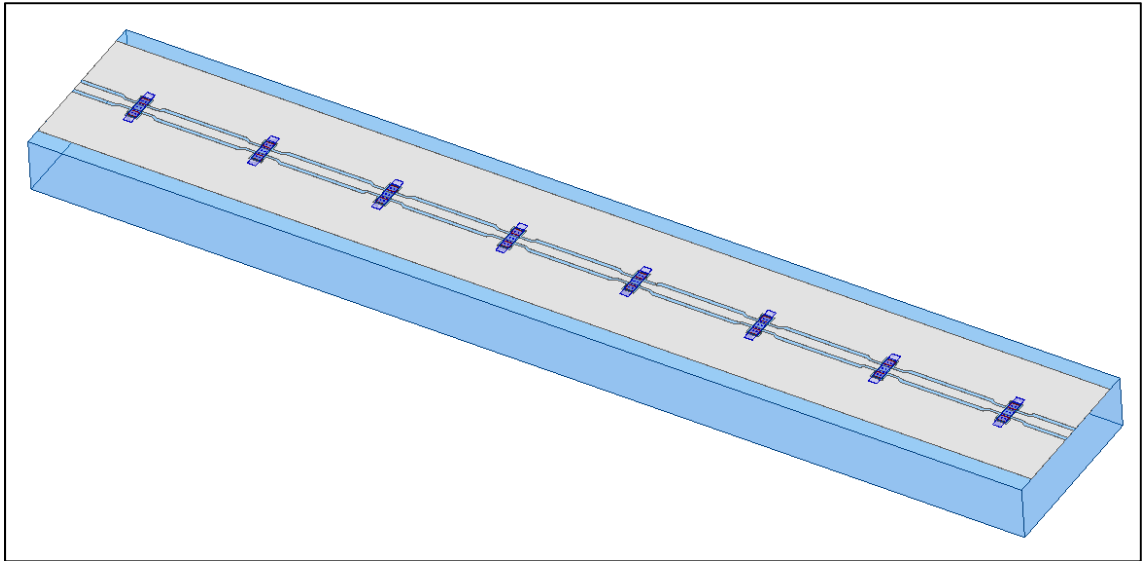


Figure 3.9 MEMS-on-LTCC planer tuner 3D view

The MEMS-on-LTCC tuner behavior is simulated using HFSS 3D field and ADS circuit simulations (see Appendix I). 256 (2^8) states resulting from various switches' up and down states combinations are synthesised over the [2 GHz – 7 GHz] frequency band. Figure 3.10 shows the impedance coverage generated at one port when the other port is terminated by a 50 Ω load at selected frequencies. Despite the retracted coverage related to the limited impedance change between the switches' states at low frequencies, the tuner offers good coverage of the Smith chart, starting at frequencies as low as 2 GHz. At higher frequencies ($f > 4$ GHz) where the impedance change and the electrical length are high enough, better distributed coverages are obtained.

Apart from the exact constellation where each point from the synthesised 256 impedances provides an ideal matching, the MEMS-on-LTCC tuner may offer better performance if we consider lower matching levels. As detailed in section 3.3.2 and using equation 3.14, matching levels are studied at the frequencies considered in figure 3.10 and are visualised in figure 3.11. As it can be seen, a matching level of 10 dB corresponds to a large covered area between 2 GHz and 3 GHz. Higher frequencies offer excellent matching capabilities at each point of the Smith chart.

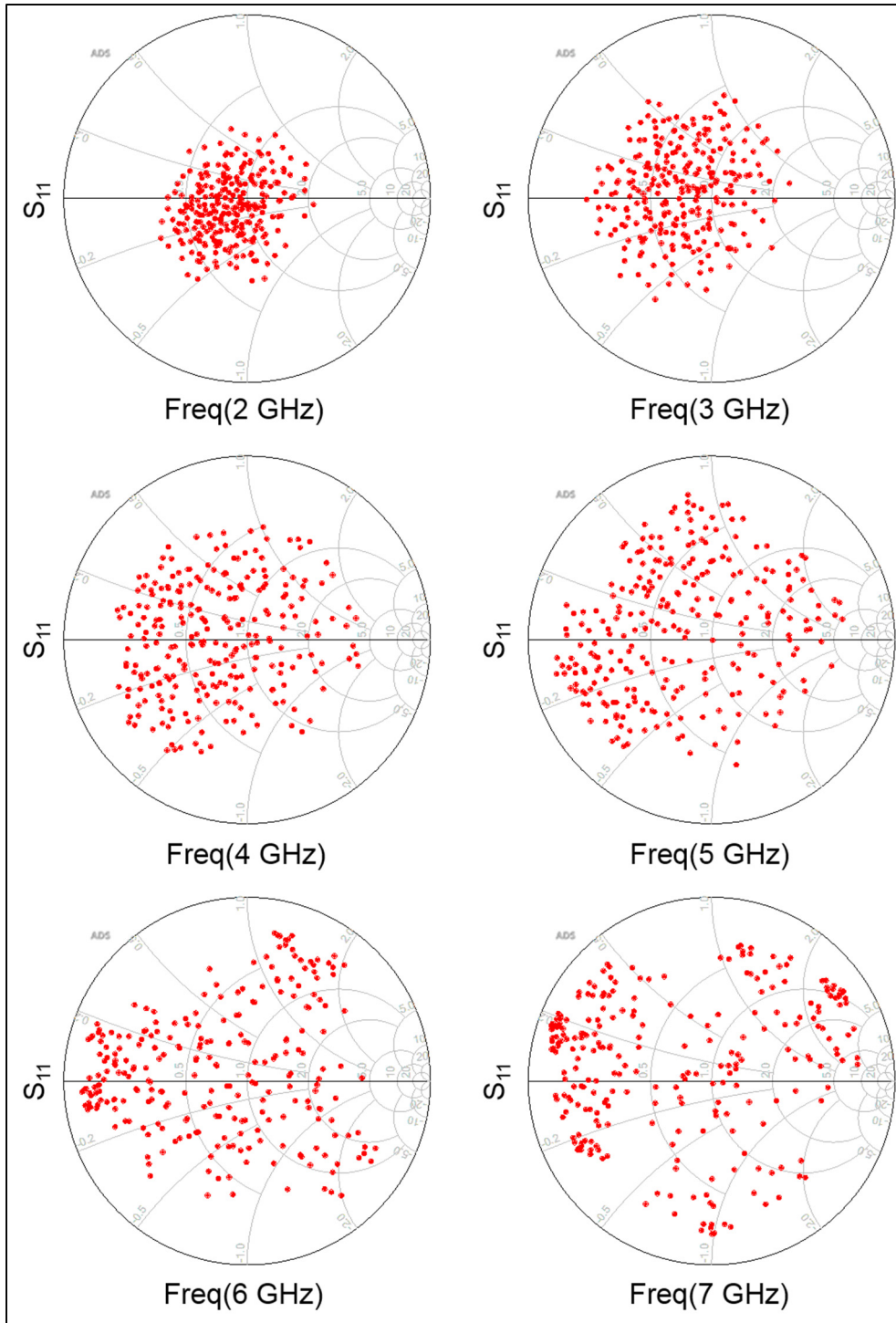


Figure 3.10 MEMS-on-LTCC tuner simulated Smith chart coverage at different frequencies between 2 GHz and 7 GHz

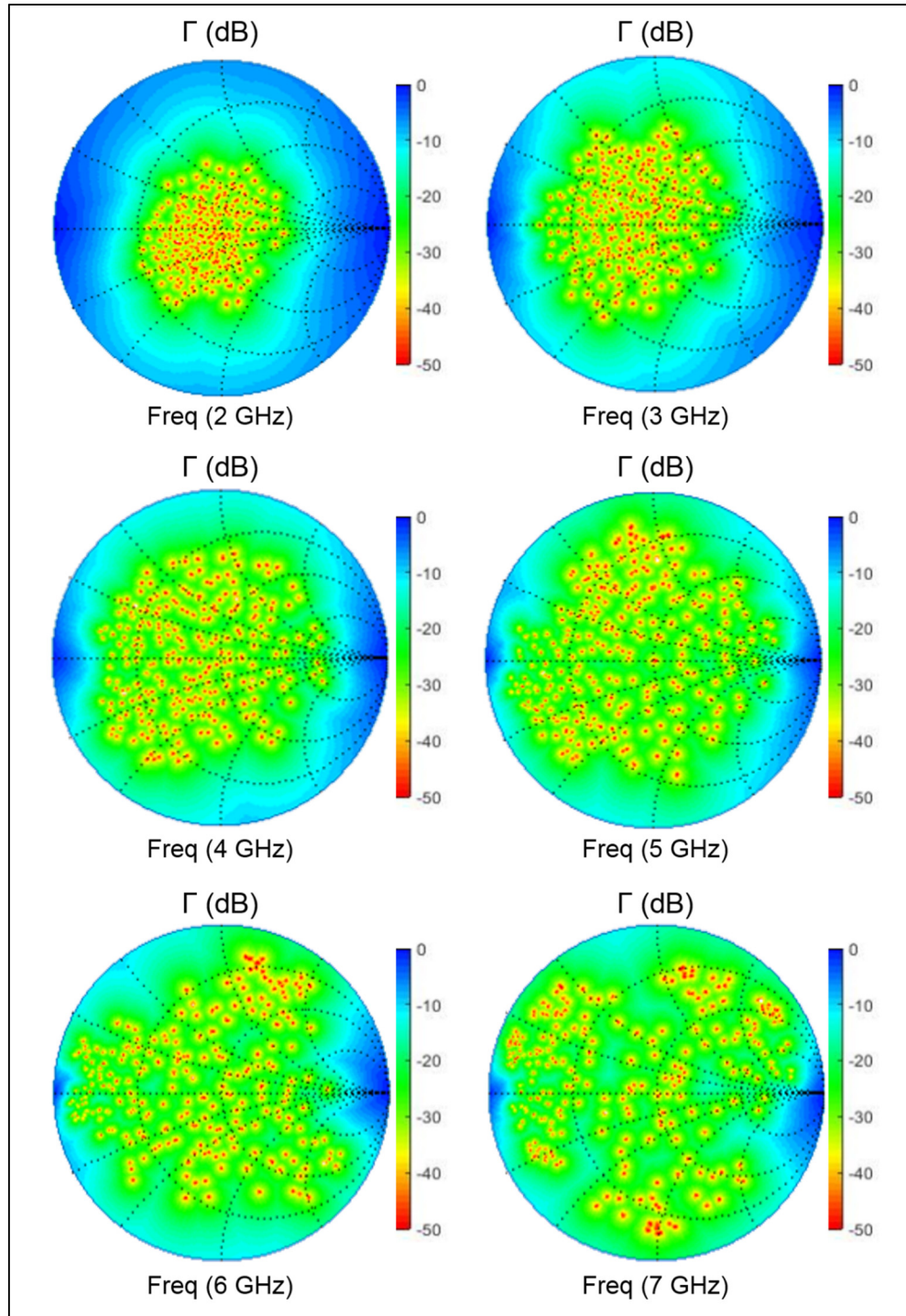


Figure 3.11 MEMS-on-LTCC tuner simulated reflection coefficient over the gamma plane at different frequencies between 2 GHz and 7 GHz

3.4.3 MEMS-on-LTCC 3D tuner

Taking advantage of the LTCC technology's 3D nature and its ability to realize buried transmission lines inside a multilayer substrate, the proposed planar MEMS-on-LTCC tuner may be shrunk significantly while maintaining similar performance. This miniaturisation step consists simply of routing some parts of the tuner's transmission lines that interconnect the switches inside the substrate. In this context, vertical interconnections between the different layers will be required and must be carefully designed.

3.4.3.1 Vertical LTCC transitions

We propose three different vertical transitions between a $50\ \Omega$ CPW upper transmission lines and a buried striplines as shown in figure 3.12. As in (Belambri, Dubouil, Talbot, Kouki, & Gagnon, 2011), a quasi-coaxial (Q-coax) interconnect illustrated in figure 3.12-a and composed of a cylindrical signal via surrounded by grounded vias is implemented. The second transition depicted in figure 3.12-b is a modified Q-coax transition, where the cylindrical grounded vias are replaced by curved ones. Figure 3.12-c represents a CPW transition where the signal line and the ground planes are formed using vertical rectangular vias.

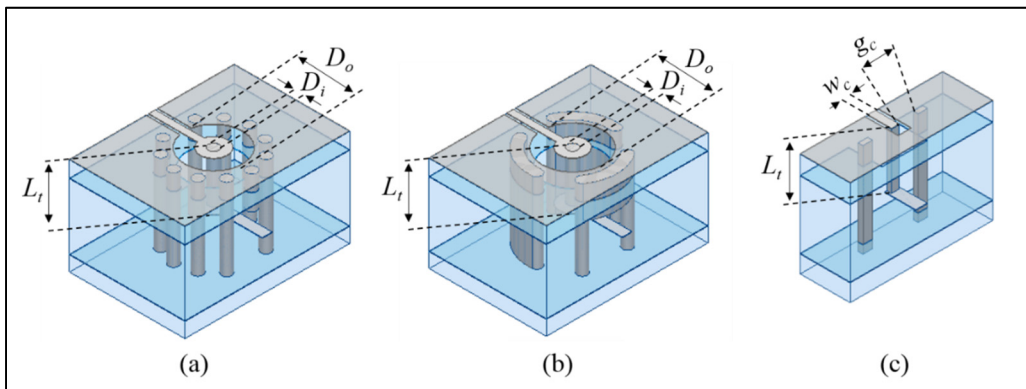


Figure 3.12 Vertical transitions: a) Q-coax, b) modified Q-coax and c) CPW

The three transitions, implemented on DuPont 951, are simulated with the HFSS software. Since the diameter of the cylindrical signal (D_i) via is fixed by the LTCC process, the Q-coax

and the modified Q-coax outer diameters (D_o) and discontinuities are tuned to fit the LTCC fabrication requirements and to obtain 50Ω transitions. As for the CPW transition, the rectangular vias' thickness is set to $50 \mu\text{m}$ to meet the LTCC process's minimal feature size. Its physical parameters (w_c , g_c) are optimised to match 50Ω . Table 3.6 summarizes the optimized transitions' geometrical dimensions.

Table 3.6 Vertical transitions geometrical dimensions

| Parameter | Value |
|---|--------------------|
| Q-coax inner diameter (circular via diameter): D_i | $126 \mu\text{m}$ |
| Q-coax outer diameter: D_o | $1170 \mu\text{m}$ |
| Modified Q-coax outer diameter: D_o | $1200 \mu\text{m}$ |
| CPW center conductor width: w_c | $80 \mu\text{m}$ |
| CPW gap between vertical center conductor and ground plane: g_c | $200 \mu\text{m}$ |
| Transition length (six 4.5 mils layers): L_t | $587 \mu\text{m}$ |

Figure 3.13 shows the simulated overall attenuation per transition. In addition to being the smallest, the CPW vertical transition presents less than 0.04 dB of attenuation and demonstrates the lower degradation over the Q-coax and modified Q-coax counterparts from 2 GHz to 7 GHz. The CPW transition will therefore be used for the miniaturized tuner.

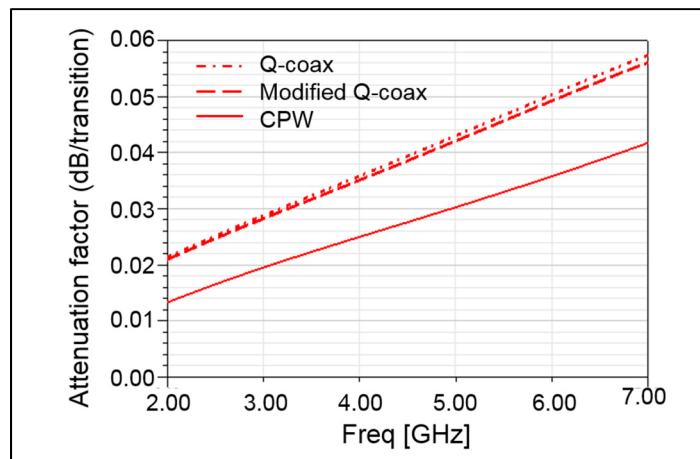


Figure 3.13 Vertical transitions attenuation's factors

3.4.3.2 3D tuner

Here, we first consider a modified design of the MEMS-on-LTCC switch where a part of the upper CPW line is replaced by a smaller structure made of two vertical CPW transitions and two buried striplines. Using twelve 4.5-mil layers of DuPont951, the different lines are distributed as shown in figure 3.14 to allow easy transitions between the different layers as well as providing a miniaturised architecture. The stripline's width and length are dimensioned and simulated with HFSS to ensure that the 3D MEMS-on-LTCC switch's performance fits its planar counterpart. The obtained dimensions are detailed in table 3.8. With this 3D configuration, the switch's size is reduced from $3.4 \text{ mm} \times 1.2 \text{ mm} \times 1.29 \text{ mm}$ to $1.79 \text{ mm} \times 1.2 \text{ mm} \times 1.19 \text{ mm}$.

Table 3.7 Stripline geometrical features

| Parameter | Value |
|---|-------------------|
| Stripline width: w_{st} | $120 \mu\text{m}$ |
| Ground plane spacing (eight 4.5 mils layers): B | $793 \mu\text{m}$ |
| Stripline length: L_{st} | $600 \mu\text{m}$ |

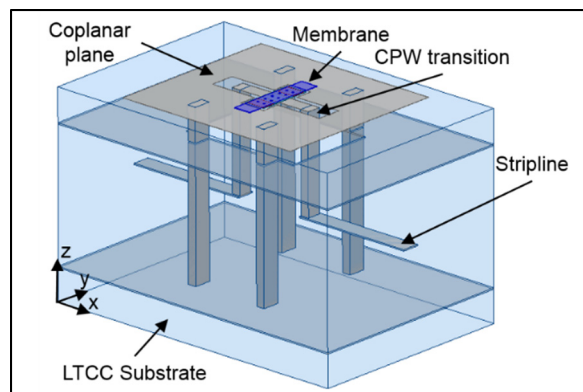


Figure 3.14 RF MEMS-on-LTCC 3D switch

Figure 3.15 shows a superposition of the simulated S-parameters for both planar (red curves) and 3D (blue curves) MEMS-on-LTCC switches between 2 GHz and 7 GHz. The 3D switch

provides better insertion loss (figure 3.15-a) as a part of the CPW line is replaced by a stripline and so its associated radiation loss is suppressed. Phase shifts (figure 3.15-b) and input impedances (figure 3.15-c) track very well at up and down states over the entire frequency range, showing that LTCC based miniaturisation doesn't affect the overall performance.

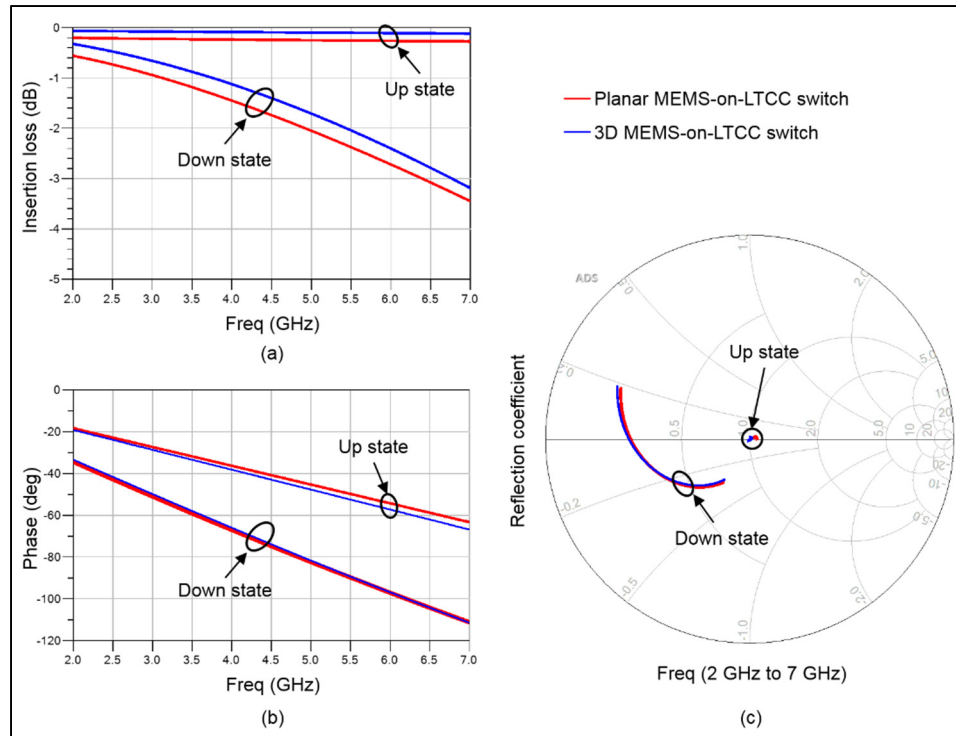


Figure 3.15 Field simulation of the planar and 3D MEMS-on LTCC switches: a) insertion loss, b) phase shift and c) reflection coefficient

Similarly to the planer tuner, eight miniaturized 3D switches were cascaded to form the 3D tuner. Two CPW vertical transitions are added at the input and the output for measurement purposes. A significant gain in terms of the size of the overall tuner is obtained as shown in figure 3.16. In fact, the final size is reduced from $27.2 \text{ mm} \times 1.2 \text{ mm} \times 1.19 \text{ mm}$ to $14.76 \text{ mm} \times 1.2 \text{ mm} \times 1.19 \text{ mm}$, close to 50% reduction in length. However, even further size reduction can be obtained through transmission lines (CPW and stripline) routing. For instance, figure 3.17 illustrates a second iteration of the 3D tuner with an extremely small size of $5.51 \text{ mm} \times 2.54 \text{ mm} \times 1.19 \text{ mm}$, which represents approximately 80% length reduction over the original planar tuner.

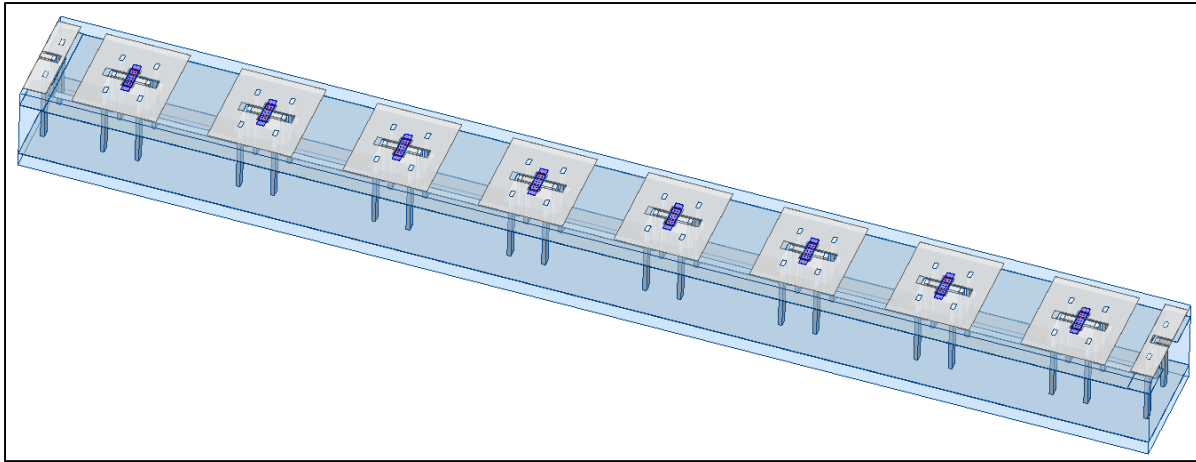


Figure 3.16 RF MEMS-on-LTCC 3D tuner (1st iteration)

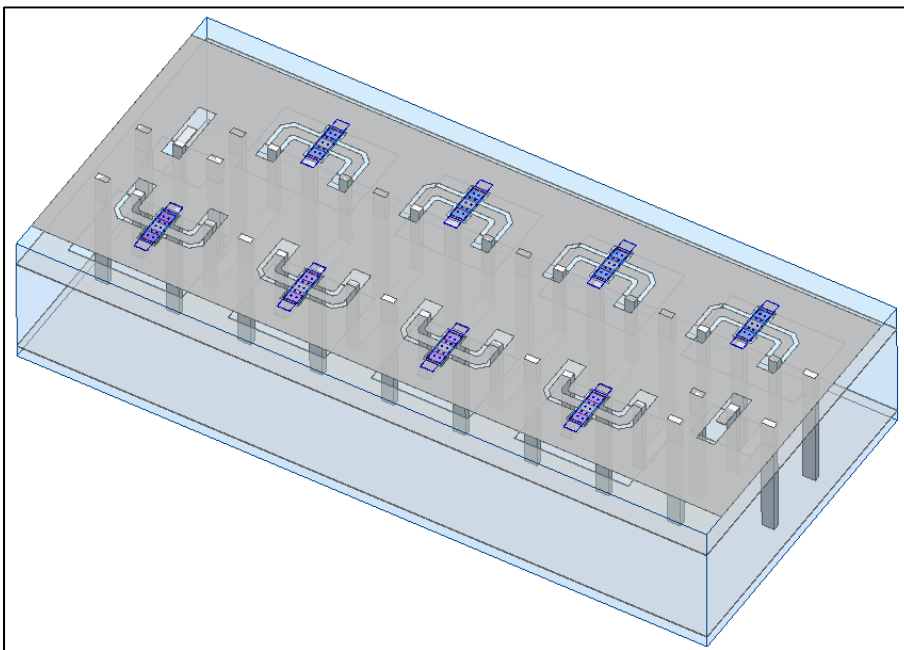


Figure 3.17 RF MEMS-on-LTCC 3D tuner (2nd iteration)

Figure 3.18 shows a superposition of the three tuner iterations' impedance coverages, which were synthesized through cascaded HFSS 3D field simulations of a single cell in ADS (Appendix I). Both 3D tuner iterations demonstrate coverages similar to their planar counterpart for six frequency points in the range of [2 – 7 GHz].

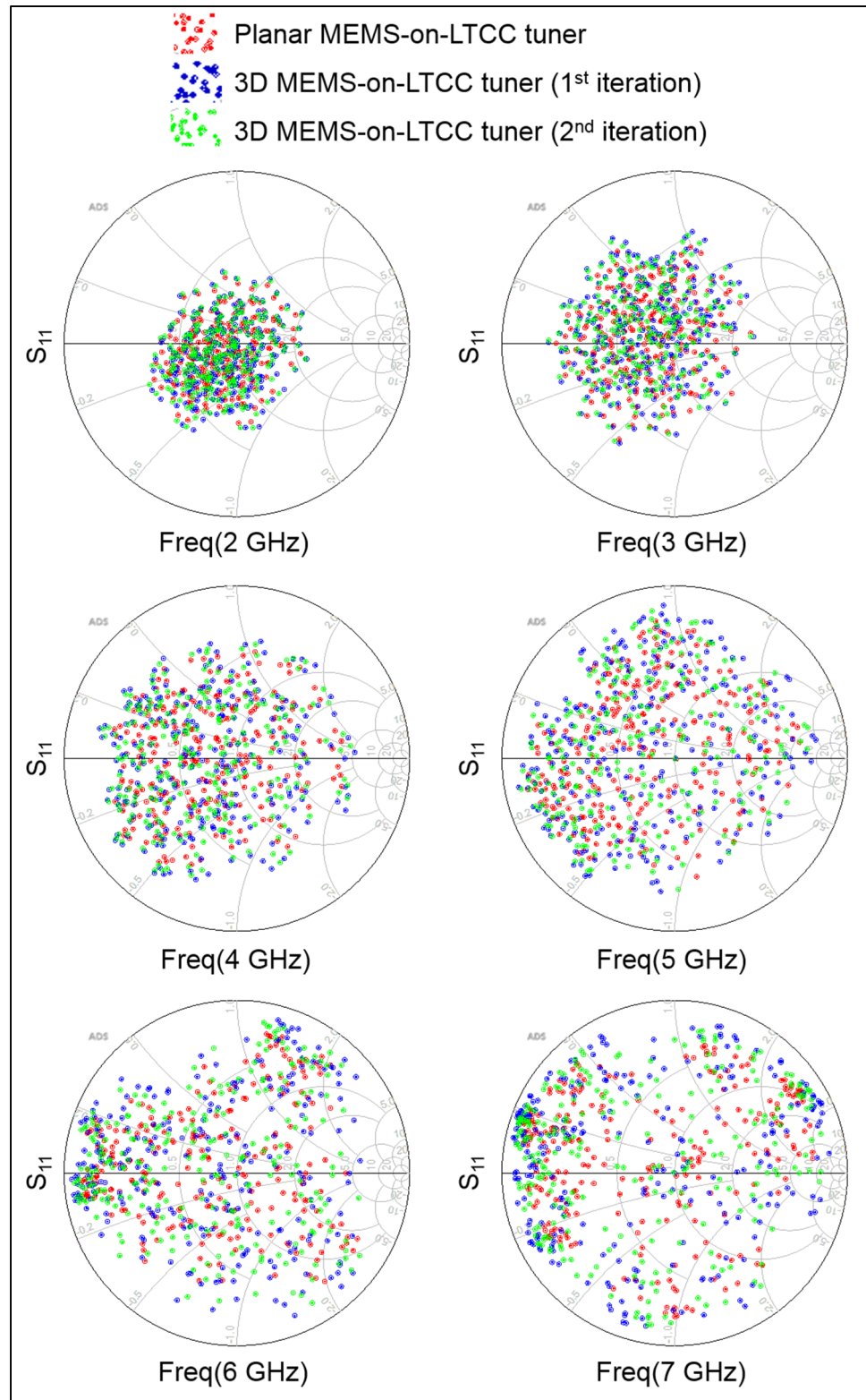


Figure 3.18 MEMS-on-LTCC planar and 3D tuners simulated Smith chart coverage at different frequencies between 2 GHz and 7 GHz

3.5 Comparison of fluidic and MEMS-on-LTCC tuners

Both fluidic and MEMS-on-LTCC tuners demonstrate their ability to operate at low frequencies while maintaining small sizes. In fact, they offer good coverages as low as 0.9 GHz, for the fluidic tuner, and 2 GHz, for the MEMS-on-LTCC tuner. However, while the fluidic is not recommended to operate at frequencies higher than 2.4 GHz due to the DI-water's increasing loss, these frequencies can be covered by the MEMS-on-LTCC tuner. Still, both tuners show that they offer performance better than other reported counterparts in the literature as detailed in table 3.8. For fluidic tuners, most of reported ones are designed to match particular states as in (Chlieh & Papapolymerou, 2017; M. Lee & Lim, 2018) or present huge gaps on the smith chart coverage as in (Lei et al., 2012; Morishita, Dang, Gough, Ohta, & Shiroma, 2015). The fluidic tuner we present in this report is much smaller than its counterparts (table 3.4) with better Smith chart coverage. As for the MEMS tuners, which are generally restricted to work at high frequencies as in (Tauno Vähä-Heikkilä et al., 2007), the MEMS-on-LTCC tuners that we have introduced operate at low frequencies without the requirement of complicated techniques as the slow wave structure used in (Domingue, Fouladi, et al., 2009). Moreover, based on LTCC 3D capability, the 3D tuner provides a competitive size compared to the planar one.

Table 3.8 RF tuner's comparison

| Ref | Tuner's type | Size (mm ³) | Impedance Coverage | Frequency (GHz) |
|--|------------------|------------------------------------|--------------------|-----------------|
| (M. Lee & Lim, 2018) | Metal fluid | $60 \times 40 \times 1.51$ | 2 points | • 0.9 |
| (Lei et al., 2012; Morishita et al., 2015) | Metal fluid | $\approx 40 \times 35 \times 1.79$ | wide | [3.37– 6.02] |
| (Chlieh & Papapolymerou, 2017) | Dielectric fluid | $76 \times 76 \times 0.7$ | 2 points | • 2.4 • 4.8 |
| (Tauno Vähä-Heikkilä et al., 2007) | MEMS | $7.3 \times 7.3 \times ?$ | wide | [6 – 24] |

Table 3.8 RF tuner's comparison (continued)

| Ref | Tuner's type | Size (mm ³) | Impedance Coverage | Frequency (GHz) |
|--|------------------|--------------------------------|--------------------|-----------------|
| (Domingue, Fouladi, et al., 2009) | MEMS | $4 \times 0.5 \times 0.64$ | wide | [3 – 8] |
| Fluidic tuner: this work | Dielectric fluid | $26 \times 10 \times 1.5$ | wide | [0.9 – 2.4] |
| MEMS-on-LTCC planar tuner: this work | MEMS | $27.2 \times 1.2 \times 1.19$ | wide | [2 – 7] |
| MEMS-on-LTCC 3D tuner (1 st iteration): this work | MEMS | $14.76 \times 1.2 \times 1.19$ | wide | [2 – 7] |
| MEMS-on-LTCC 3D tuner (2 nd iteration): this work | MEMS | $5.51 \times 2.54 \times 1.19$ | wide | [2 – 7] |

3.6 Conclusion

Two types of novel RF impedance tuners in LTCC technology have been presented based on a periodic arrangement of 8 identical cells made basically of fluid-fillable cavities or MEMS switches. Closed form equations for the calculation of a single cell's electrical characteristics, both fluidic and MEMS, have been derived and used in the cell's and tuner's designs. Empty/deionized water filled cavities and movable membranes have been used to achieve reconfigurability with a high change in impedance and electric length, even at low microwave frequencies, thereby offering good coverage of the Smith chart by the tuners. While LTCC hermiticity and 3D characteristics are exploited to prevent concerns about the fluidic tuner's operation, its multilayer capability was leveraged to achieve considerable miniaturisation of the planar MEMS-on-LTCC tuner.

MEMS-ON-LTCC PROCESS

4.1 Introduction

Materials and processes are the most important factors in the successful realization of RF-MEMS components since they directly influence the resulting performance. Silicon and alumina as substrates have been widely used to fabricate MEMS circuits (Rebeiz, 2004). Ceramic substrates, such as LTCC, with improved dielectric properties, higher integration ability and miniaturized size become of increasing importance in this context. In this chapter, we present the various MEMS-on-LTCC process steps starting from surface treatment to the release of the movable membrane (Bahloul, Ben Amar, & Kouki, 2016). Step validation and challenges encountered through the definition of the various layers are highlighted. A switch prototype is then proposed based on the developed process and multi-physics simulations.

4.2 MEMS-on-LTCC process development

Fabrication of MEMS components directly on a LTCC 3D multilayer technology, has not been investigated or developed much as highlighted in the first and second chapters. This is in part due to fact that one needs to have access to the equipment and materials required for both LTCC and MEMS technologies. Fortunately, such a rare infrastructure is available at the LACIME laboratory, allowing us to investigate their combination to develop a novel MEMS-on-LTCC process. Due to its relative complexity, we propose to start with a general idea about the final process flow and then detail the different requirements at each step and discuss the encountered technical challenges.

4.2.1 Process flow overview

In this thesis, we are interested in electrostatically actuated MEMS devices developed on an LTCC substrate that may incorporate buried elements and interconnects. However, MEMS

processes require excellent surface finishes in terms of planarity and low roughness. Unfortunately, the standard LTCC process yields structures with high surface roughness, on the order of several microns, and sometimes limited planarity. Therefore, the first step must consist of polishing the LTCC substrate to reach the required smoothness and ensure the feasibility of well-shaped thin films. Once the LTCC substrate is polished to the required surface finish, we can use surface micromachining techniques, commonly used in planar MEMS processes like on silicon wafers, to form the different layers and realize the MEMS devices. However, since no standard detailed MEMS-on-LTCC process has been published, several investigations and deep explorations have been carried out. Also, special care has been given to the LTCC's potential chemical interactions with some materials typically used in MEMS processes, such as hydrofluoric (HF) acid.

Various materials, machines and techniques were experimented during the process development to address size and shape requirements as well as layer material compatibility. Figure 4.1 summarizes the final process, whose different sequences are detailed in Appendix II. It is composed of 9 main steps, as follow:

1. Polishing of the LTCC substrate containing buried circuits;
2. First metal layer forming: 1 μm of aluminum (Al) film is deposited on the polished LTCC substrate using DC sputtering on a patterned photoresist layer which is thereafter stripped to define the RF transmission lines. Here, no adhesion material like chromium (Cr) or titanium (Tn) is used as Al adhere well on our polished ceramic. Also, passivation dielectric layer, frequently used on semiconductor substrates like silicon, is not required;
3. First dielectric layer forming: 500 nm of silicon dioxide (SiO_2) layer is deposited using RF sputtering, followed by an anisotropic dry IBE (Ion Beam etching) etching leaving thus only the oxide material covered with a photoresist mask. As temperature rises along the etching, several mask's stripping sub-steps under different stripper temperatures are required. This oxide layer serves to prevent physical connection between the first and the second metal layers;
4. Second metal layer forming: 1 μm of Al films are patterned using the same recipe of step 2 to form the DC circuitry (bottom electrodes and biasing lines and pads);

5. Second dielectric layer: 300 nm of SiO₂ layer is deposited and patterned with the recipe detailed in step 3. It isolates the RF signal line and the bottom electrodes from the movable membrane;
6. Deposition of the sacrificial layer: 2 μm of a polyimide material (PI-2545) is spin coated and heated;
7. Anchors patterning: the polyimide layer is patterned using a photoresist masking layer. Openings in the photoresist and photosensitive polyimide double layer are made through UV exposure. Photoresist stripping leaves thereafter a patterned sacrificial layer;
8. Membrane patterning: it consists of Al/ Cr double layer. 100 nm of Al seed layer is first DC sputtered directly on the sacrificial layer. Then, 1 μm of Cr is deposited on a patterned photoresist layer. The membrane form is defined following the photoresist stripping. An Al etchant is subsequently used to etch the Al seed layer. Here the Cr layer serves simultaneously as a functional layer and a mask to etch the Al layer. Depending on the membrane size, adding some holes is recommended to promote the under-etching during the release step;
9. Membrane release: the sacrificial layer is wet etched based on a 2 sub-step stripping operation. Critical point dryer (CPD) is then used to remove liquids. It prevents thus the membrane stiction to the bottom layers, a well-known phenomenon in wet etching of thin sacrificial layers (few microns).

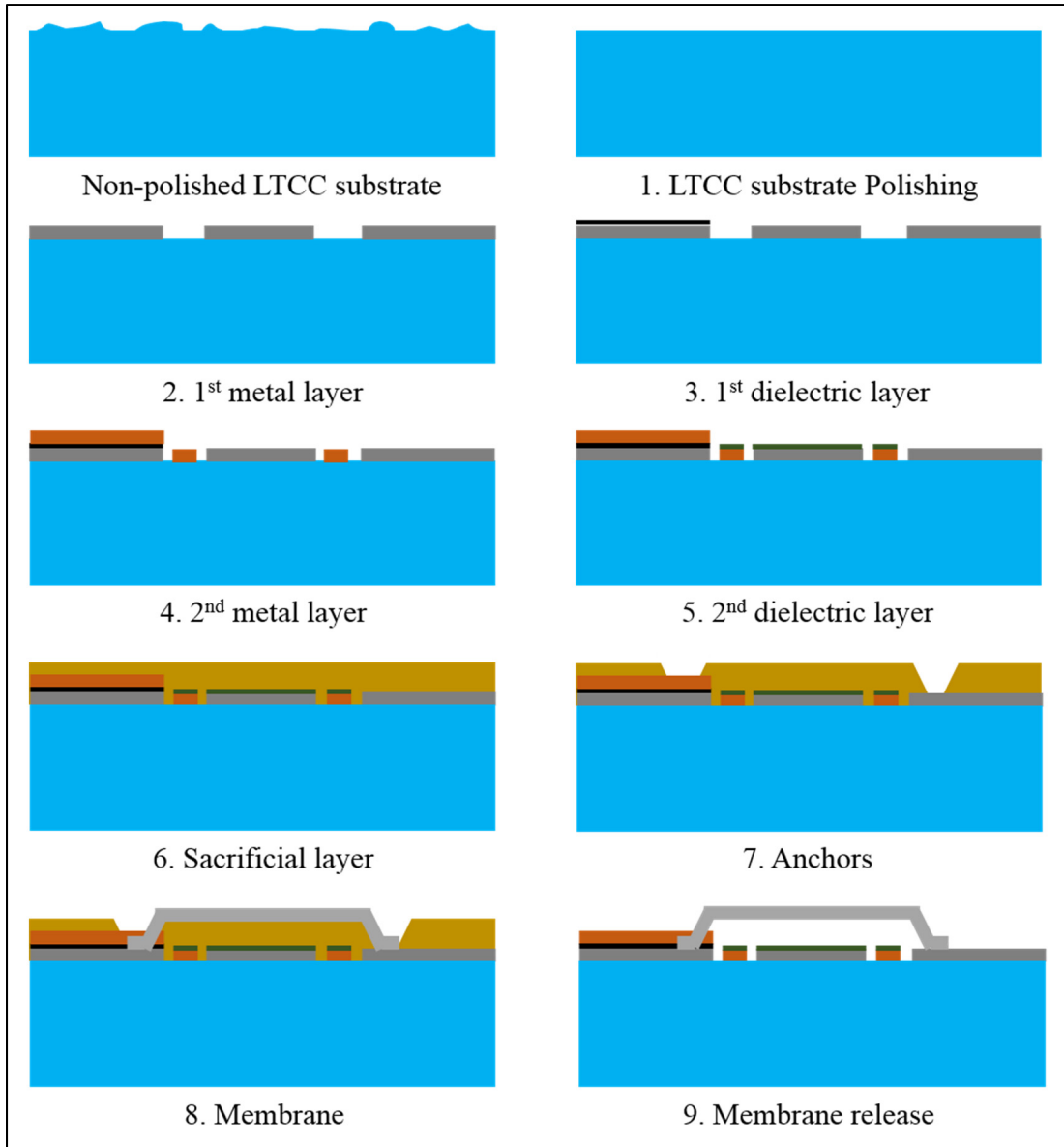


Figure 4.1 MEMS-on-LTCC process flow

4.2.2 Fabrication challenges and considerations

4.2.2.1 LTCC surface finish

An important concern in a MEMS process is how smooth the wafer's surface is. Surface roughness will negatively impact the patterning and development of layers and will, therefore, influence their electrical (losses, isolation, etc.) and mechanical (shape of the subsequent

layers, etc.) performance. Unfortunately, unlike silicon wafers which are very smooth, co-fired LTCC surfaces are significantly rough. Vias and circuits buried into the LTCC add more irregularities to the substrate and increase its roughness as well as its waviness. The mean roughness of an LTCC substrate after co-firing is higher than $1\mu\text{m}$. However, a very flat and smooth surface with a mean roughness typically around tens of nanometers is required to build functional MEMS devices. Therefore, substrate roughness is the most critical design issue in the MEMS-on-LTCC process development.

Chemical Mechanical Polishing (CMP) is a process used to reach an optimum planarization level of a dielectric or a metal before the development of upper layers (H. J. Kim, Choi, Hong, Lee, & Ko, 2012). It involves mechanical and chemical reactions. While a downward force is applied to a revolving wafer against a rotating platen, slurry containing abrasives and reactive chemicals is used to remove unwanted material from the wafer's surface, as shown in figure 4.2. Removed parts are evacuated outside of the platen through a conditioner. Polishing is considered as a complicated and weakly understood process as it depends on the optimization of a wide range of factors such as: slurry choice, slurry rate, pad choice, platen and carrier rotation speed, polishing time, pressure, etc. Experimenting and optimizing the polishing process is compulsory to find the parameters needed to reach the targeted LTCC surface smoothness for the MEMS layers' development.

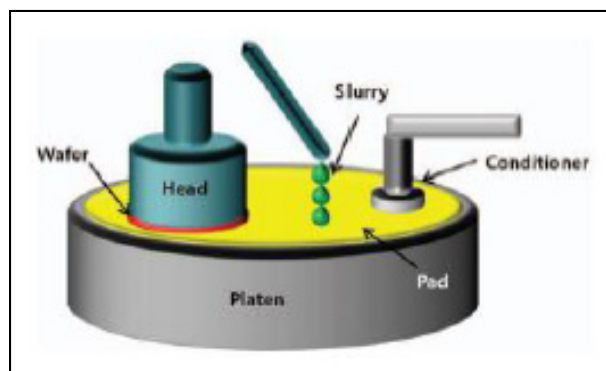


Figure 4.2 CMP process
Taken from H. J. Kim et al. (2012)

To obtain the LTCC surface finish for the development of MEMS elements, several planarization tests have been carried out using the CMP (BT-380C) instrument from RTEC Instrument, Inc. Polishing was performed in two steps using two slurries dedicated to ceramic polishing and containing particles with different sizes. First, Ultra-Sol Diamond solution with 1 μm grains was used to decrease the LTCC waviness and to drop the roughness to an intermediate value. Then, Ultra-sol 556 Colloidal Silica slurry with 0.07 μm particles was utilized to reach the targeted roughness of tens of nanometers. The second slurry allows proportional removal of metal and dielectric materials, avoiding thus the creation of holes around via locations. This way, obtaining a flat surface is possible even in the presence of vias holes. The different process parameters (time, pressure, rotation velocity, etc.) were also investigated and optimized according to the initial LTCC surface state.

The polished LTCC substrate surface was characterized using the optical confocal microscope Olympus Lext OLS 4000. Figure 4.3 shows 3D optical views of samples from an LTCC surface substrate before and after polishing. The mean surface roughness S_a has been enhanced from 850 nm to 30 nm for a via free 640 μm x 640 μm LTCC sample (figure 4.3-a and b). The maximum surface roughness S_z (difference between the peak and valley points in a surface) has dropped from 11 μm to 315 nm for the same sample. Including vias in a LTCC substrate increases the roughness. figure 4.3-c shows a via hole in a 640 μm x 640 μm LTCC surface with a mean roughness S_a of 1 μm and a maximum roughness S_z of 13 μm before polishing. After polishing, we have obtained a smooth surface (figure 4.3-d) with a mean roughness S_a of 50 nm and a maximum roughness S_z of 657 nm. We noticed that errors may occur during the roughness measurement procedure. In order to obtain accurate and significant results, we applied a surface filter to suppress these errors.

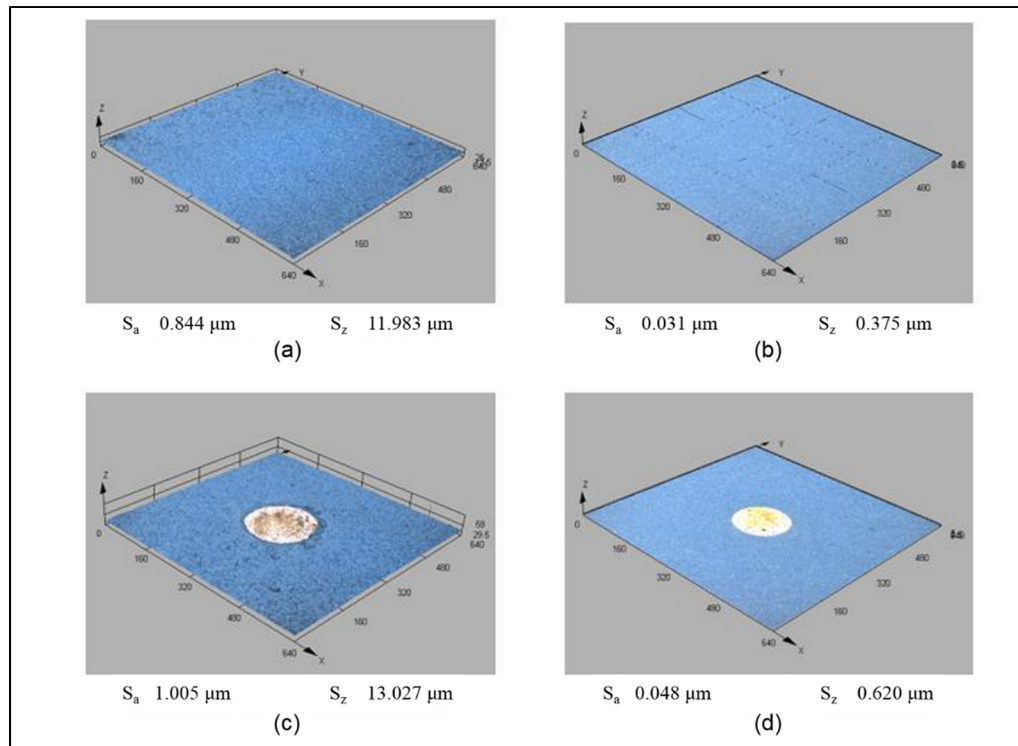


Figure 4.3 LTCC surface roughness: a) without via before polishing, b) without via after polishing, c) with via before polishing and d) with via after polishing

4.2.2.2 Pin holes

Small defects related to extra or missing material may occur during thin films processing (Franssila, 2010). Apart from their cosmetic effect, they are fatal as they often cause functional problems, and they may even lead to microstructure failure. For instance, pinholes are small bores created in thin films due to the presence of contaminants in the substrate, used material (sputtered or spin coated materials) or the surrounding environment (for example sputtering chamber used to deposit different materials).

As detailed in the process flow, SiO_2 was used as a dielectric layer between the RF and DC lines, and between membranes and DC electrodes. During the testing procedure, short circuits were recorded, as shown in figure 4.4. High resistance values were also measured between Al conductive layers which are intended to be dielectrically isolated. As an excellent insulator

with very high breakdown voltage ($5\text{-}15 \cdot 10^6 \text{ V/cm}$), SiO_2 layer cannot become electrically conductive at the voltage range required to actuate RF MEMS switches. Therefore, the presence of pinholes on the SiO_2 layer, allowing to form a shortage path between the Al layers, is confirmed.

Pinholes are more likely to take place in thinner films (hundreds of nm), as in the oxide isolation layers required in our process. They were probably formed during the RF sputtering of the SiO_2 layer due to the presence of contaminants on the substrate or in the sputtering chamber. Contaminants or bubbles in the spin-coated photoresist layer, used as a mask to etch the SiO_2 layer, may also lead to form some holes, which will be transferred to this dielectric layer during the etching step. Films free from pinholes defects are required to generate functional switches. Consequently, to avoid this problem, we insist on applying some rules throughout the different process steps: a well-controlled cleaning process with a high quality vacuum is compulsory to remove contaminants from treated surface, solutions, targets, machines and surrounding environment. Also, bubbles should be treated and removed before materials spin coating.

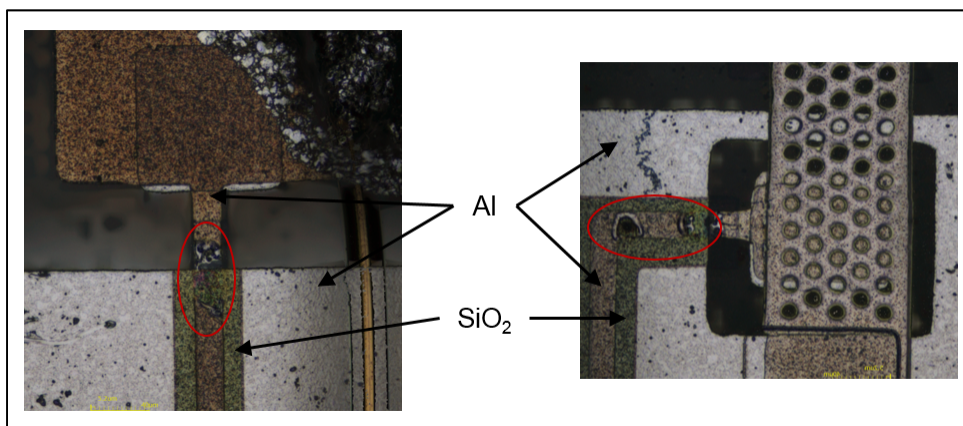


Figure 4.4 RF MEMS switch short circuits due to pinholes

4.2.2.3 Membrane stress

Stress is a critical problem related to MEMS' released membranes since it affects their operation, and may lead to un-functional switches. It causes membrane buckling and thereby

altering its expected response: changes the on and off capacitances, modifies the pull down voltage, or even results in membrane cracking or a permanent contact between the membrane and the lower functional layers.

We distinguish two types of stresses: residual stress developed due to the intrinsic and thermal (or extrinsic) interactions taking place during the deposition step, and post-fabrication stress resulting from the surrounding atmospheric pressure on the membrane or other processing external forces (Al-masha'al, Mastropaolo, Bunting, Dunare, & Cheung, 2017). Intrinsic stress occurs during thin film growth and is due to particles' energy, their interactions, their phase transformations and lattice mismatch between the membrane and its precursor layer. As for thermal stress, it arises from layers' thermal expansion coefficients misfit.

The overall stress depends basically on the used materials for the membrane and the sacrificial layer, deposition conditions (pressure, power, gases flow rate, etc.), release technique and the environmental conditions. Avoiding stress is challenging, but low stress values are accepted for RF MEMS switches. We performed several experiments to minimize the stress associated to the membrane of the MEMS-on-LTCC switch. As beam deflection can be minimized by an appropriate material choice, we considered aluminum (Al) and chromium (Cr) as membrane metals. We used two different etching techniques: dry plasma etching and wet CPD etching. The polyimide PI-2545 was employed as sacrificial layer. Sputtering parameters, mainly power and pressure, were altered to characterise the structures' stress. Table 4.1 and Table 4.2 summarize the obtained stress for various deposition and etching conditions. As we observed that sputtering power has minimum effect on the stress, these tables show results for beam deposited at fixed power (200 W) under various pressures. Based on the maximum fixed-fixed membranes deflections z_{\max} , measured with LEXT OLS4000 confocal microscope, residual stress is calculated as follow (Al-masha'al et al., 2017):

$$\sigma_r = \pm \frac{\pi^2 E}{L_s^2} \left[\frac{z_{\max}^2}{4} + \frac{t^2}{3} \right] \quad (4.1)$$

where E is membrane material Young's Modulus and t its thickness.

Table 4.1 Stress on MEMS-on-LTCC membrane

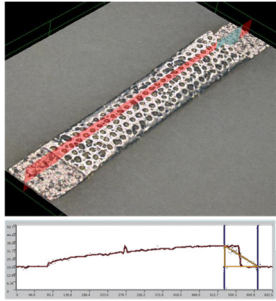
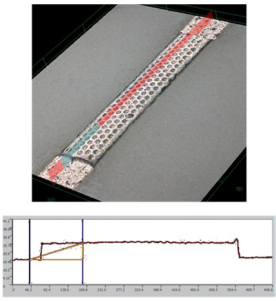
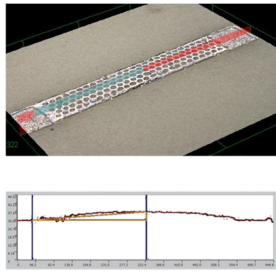
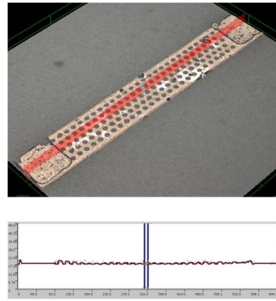
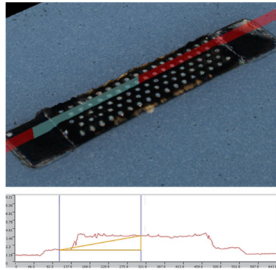
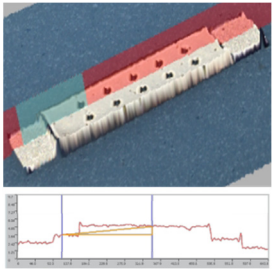
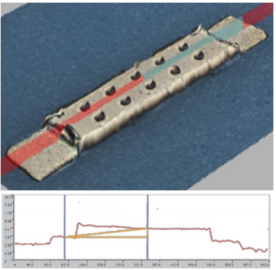
| Structure | | M1 | M2 | M3 | M4 |
|-----------------------------|-----------------------------|--|---|--|--|
| Membrane | Metal | Al | Al | Al | Al |
| | Deposition type | DC sputtering | DC sputtering | DC sputtering | Thermal evaporation |
| | Deposition Pressure (mTorr) | 10 | 15 | 20 | X |
| | Thickness (μm) | 0.65 | 0.85 | 0.8 | 0.6 |
| Sacrificial layer | Material | PI-2545 | PI-2545 | PI-2545 | PI-2545 |
| | Etching | O ₂ plasma | O ₂ plasma | O ₂ plasma | O ₂ plasma |
| Suspended membrane | |  |  |  |  |
| z_{max} (μm) | | 14 | 8 μm | 4 μm | >2.5 μm |
| Stress | Type | Compressive | Compressive | Compressive | Tensile |
| | σ_r (MPa) | -133 | -44 | -11 | >4.5 |

Table 4.2 Stress on MEMS-on-LTCC membrane (continued)

| Structure | | M5 | M6 | M7 |
|-----------------------------|-----------------------------|--|---|--|
| Membrane | Metal | Cr | Al/ Cr | Al/ Cr |
| | Deposition type | DC sputtering | DC sputtering | DC sputtering |
| | Deposition Pressure (mTorr) | 10 | 15 | 10 |
| | Thickness (μm) | 0.9 | 1.1 | 1.1 |
| Sacrificial layer | Material | PI-2545 | PI-2545 | PI-2545 |
| | Etching | O ₂ plasma | CPD | CPD |
| Suspended membrane | |  |  |  |
| z_{max} (μm) | | 0.3 | ≈ 0 | ≈ 0 |
| Stress | Type | Tensile | No stress | No stress |
| | σ_r (MPa) | 3.44 | 0 | 0 |

As detailed in tables 4.1 and 4.2, Al/ Cr membrane sputtered on the top of a polyimide sacrificial layer with a pressure of 10 mtorr, and released with CPD offers the minimum deflection. Taken into account the rapid transition between tensile and compressive stress, deflection was measured for several beams through different fabrication iterations. Low stress with almost no deflection was ensured for the different fabrication runs.

4.3 Application: Capacitive RF MEMS-on-LTCC switch

In the light of the MEMS switch requirements for RF tuners, detailed in chapter 3, and based on the developed MEMS-on-LTCC process steps and constraints, we detail the design of the RF MEMS-on-LTCC switch. It is a capacitive switch with lateral electrostatic actuation. Figure 4.5 illustrates a longitudinal view of the proposed structure. A fixed-fixed suspended membrane is used as the moving part. The two actuation pads have a width of W_{DC} and are supposed to be placed at a distance S from both sides of the central RF transmission line. As the switch's RF operation principle and simulation have been presented in chapter 3, only the electro-mechanical study is presented here. Indeed, analytical dimensioning and COMSOL Multiphysics simulations are performed. Then, the switch fabrication steps are detailed.

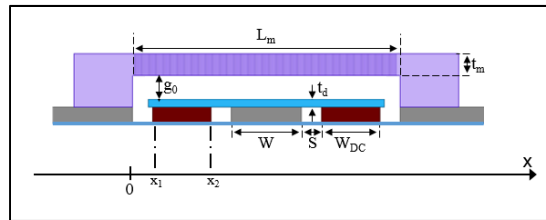


Figure 4.5 RF MEMS-on-LTCC switch longitudinal view

4.3.1 Electromechanical analysis

4.3.1.1 Analytical model

From an electromechanical perspective, an electrostatically actuated RF MEMS switch is made of two parallel plates: a movable electrode (the membrane) on the top and fixed ones (actuation

pads) at the bottom (Rao, Thalluri, Guha, & Sravani, 2018; Rebeiz, 2004). Applying a voltage V between these electrodes results in an electrostatic force F_e , leading to membrane deflection. A restoring force F_k , resulting from the membrane's stiffness, takes thereby place to carry it back to its initial position. Applying a force F_e higher than F_k results in its collapse and an abrupt change in the switch capacitance C from $C_{MEMS-up}$ to $C_{MEMS-down}$. At the down position, a contact force F_c , due to two close surfaces' interactions and the Van Der Waals forces, arises. The presence of a gas (air, nitrogen, etc.) surrounding the switch may cause a damping force, F_d . It changes, most importantly, the actuation speed. Consequently, the RF MEMS switch electromechanical operation can be described by the following equation (Marcelli, Lucibello, Angelis, Proietti, & Comastri, 2010):

$$F_e + F_k + F_c + F_d = m \frac{d^2 z}{dt^2} \quad (4.2)$$

where:

$$F_e = \frac{1}{2} \frac{\partial C_{dc}(z)}{\partial z} V^2 \quad (4.3)$$

$$F_k = -k[z - (t_d + g_0)] \quad t_d \leq z \leq t_d + g_0 \quad (4.4)$$

$$F_c = -\alpha \frac{dz}{dt} \quad (4.5)$$

$$m = \rho A t_m \quad (4.6)$$

z is the motion direction, $C_{dc}(z)$ is the capacitance between the membrane and the actuation pads, k is the membrane equivalent spring constant, ρ is the membrane material density, A is the membrane area, t_m is the membrane thickness and α is the damping factor.

Based on Equations (4.2) to (4.6), we can extract the various parameters related to RF MEMS switch operation like actuation voltage, spring constant, power handling, switching time, resonant frequencies, etc. As it is difficult to manage and optimise all of these parameters, and as some of them don't affect the progress of our project, we focus only on the actuation voltage and the spring constant.

An equilibrium balance corresponds to applying a voltage V able to keep the membrane at an up state. It can be calculated by equating the electrostatic and restoring forces ($F_e = F_k$). This equilibrium state can be maintained up to a certain height of the initial gap g_0 . Reaching a supply voltage level where the electrostatic force dominates the restoring force causes its collapse. This voltage, known as pull-in voltage V_p , is one of the most important parameters in the design of electrostatic MEMS switches as it is required to move to the down state. It corresponds to a voltage value capable of moving the membrane down to 2/3 of the initial gap (g_0) and it is given by (Rebeiz, 2004):

$$V_p = \sqrt{\frac{8kg_0^3}{27\epsilon_0 A}} \quad (4.7)$$

As detailed in Equation (4.7), the calculation of this voltage (V_p) requires the knowledge of the membrane spring constant k , composed of two components as expressed by equation (4.8) (Marcelli et al., 2012; Rebeiz, 2004). The first part k' (equation 4.9) characterises the membrane's stiffness, and it depends on the selected geometry and material. The second one k'' (equation 4.10) accounts for the residual stress (σ_r) arising during beam fabrication. A convenient choice of the membrane material and geometry results in low spring constant, and thereby low pull-in voltage. However, a very low value of k may lead to functional problems, as permanent stiction of the membrane following its first actuation may occur. In this case, the restoring force F_k won't be high enough to liberate the membrane from the contact force F_c . For instance, a k value higher than 10 N/m is recommended to avoid such scenario (Marcelli et al., 2010).

$$k = k' + k'' \quad (4.8)$$

$$k' = \frac{-L_m EI}{2} \frac{1}{\int_{x1}^{x2} \frac{1}{48} (L_m^3 - 6L_m^2 \alpha + 9L_m \alpha^2 - 4\alpha^3) d\alpha} \quad (4.9)$$

$$k'' = \frac{L_m}{2} \frac{1}{\int_{x_1}^{x_2} \frac{L_m - \alpha}{2\sigma_r(1-\nu)w_m t} d\alpha} \quad (4.10)$$

where I is the beam moment inertia, ν is the beam material Poisson's ratio, x_1 and x_2 delimit half the actuation region (figure 4.5).

The above equations were implemented in Matlab for a rectangular fixed-fixed chromium beam with lateral actuation. Taking into account the developed MEMS-on-LTCC process' constraints, and the initial dimensions of the MEMS switch detailed in chapter 3, the spring constant and the required pull-in voltage were calculated. Table 4.3 summarizes the analytical mechanical characteristics of the proposed switch with a stress-free membrane.

Table 4.3 RF MEMS-on-LTCC switch mechanical characteristics

| Parameter | Value |
|----------------------------|-------|
| w_m (μm) | 100 |
| L_m (μm) | 340 |
| t_m (μm) | 1 |
| g_0 (μm) | 2 |
| W_{DC} (μm) | 75 |
| S (μm) | 25 |
| E (GPA) | 279 |
| ν | 0.21 |
| k (N/m) | 80.7 |
| V_p (V) | 38 |

4.3.1.2 COMSOL simulation

The proposed MEMS-on-LTCC switch has been modeled and simulated using the Electromechanics module of the COMSOL Multi-physics software, where the switch mechanical and DC electrical behaviors were computed simultaneously. A thin fixed-fixed Cr membrane suspended above two Al actuation pads and an Al RF signal line were firstly defined. A thin SiO₂ layer covering the DC and RF electrodes was added implicitly. In facts, a function, applied to the region between the fixed and movable electrodes, allows varying the dielectric constant to distinguish between this oxide layer ($\epsilon_r=4$) and the air ($\epsilon_r=1$) filling the gap. Here, to accelerate the long Finite Element Analysis (FEA) simulation time, we omitted the substrate as it doesn't affect the electromechanical operation. An air region covering the structure's top and side regions was added. The dimensions and material properties detailed in Table 4.3 were used. A holes-free membrane was first considered. As some holes are required in the fabrication process, some 12 μm holes were subtracted from the membrane in a second scenario. Considering the switch's symmetry, only the quarter of the structure was used to accelerate the simulations.

We used the electromechanics module (emi) to assign the required boundary conditions emulating the structure real environment. The membrane is free to move along the vertical direction and is subject to a fixed constraint at its anchor surfaces. A fixed mesh is applied to the DC and RF electrodes, forcing them to maintain their shape and to prevent their movement. The membrane is grounded and a voltage is applied to the DC electrodes. The electrostatic force resulting from this potential difference bends the membrane according to the Maxwell stress tensor, i.e. an equation that calculate the induced stress in a structure surrounded by an electric field or other forces. The air region is subject to a moving mesh boundary to follow the geometry change resulting from the membrane motion. As the thickness of the air region cannot contract to zero when the membrane collapses into the SiO₂ layer, its corresponding mesh is compressed into this dielectric region. Symmetry boundaries are also used as a single quadrant of the switch is modeled. A detailed Multiphysics setup for COMSOL simulation is presented in Appendix III.

To avoid the tedious non-convergent simulations occurring for unsolvable problems, the pull-in voltage is firstly computed using a stationary study. It consists of searching the required voltage to move a point on the membrane to a particular gap height. Figure 4.6 shows the beam deflection - voltage curve. The pull-in voltage is the maximum voltage under which the membrane is in an equilibrium state. It divides this curve into stable ($F_e = F_k$) and unstable ($F_e > F_k$) regions. The simulated pull-in voltages for membranes without and with holes are therefore equal to 36.8 V (V_p) and 34.4 V (V_{ph}) respectively. They correspond to a gap height of 1.17 μm . The displacement in both cases is a little bit higher than the 1/3 of the initial gap size g_0 as the mechanics solver takes into account the geometric nonlinearities. We note that the analytical and simulated pull-in voltage values are very close for the hole-free membrane. As expected, associated to a decrease in the beam mass and so in the spring constant, introduction holes, results in reducing slightly the pull-in voltage.

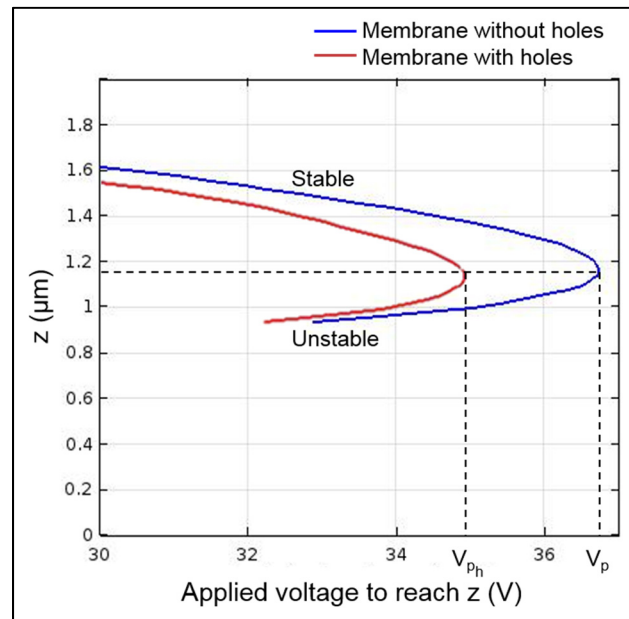


Figure 4.6 Simulated pull-in voltage

Subsequently, a time domain study is performed to reproduce the switch dynamic behavior. A voltage V_{DC} greater than the pull in voltage was applied between the membrane and the DC actuation pads, through a step function varying between 0 V and V_{DC} , set to 37 V or 35 V, as

shown in figure 4.7. The resulting electrostatic force causes the membrane to collapse onto the SiO₂ layer. A contact force is added to model the pressure between the membrane and this dielectric layer. Figure 4.8 shows the profile of the holes based membrane at the down state position after applying the DC voltage (the hole-free membrane profile is not shown here for similarity purpose). A small gap, corresponding to the dielectric layer thickness is observed between the membrane and the RF line. The displacement of the central point versus time is also depicted in figure 4.8.

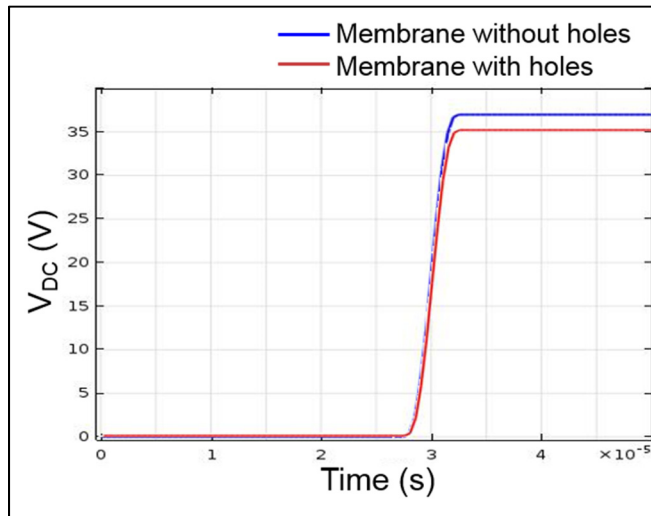


Figure 4.7 Applied DC voltage

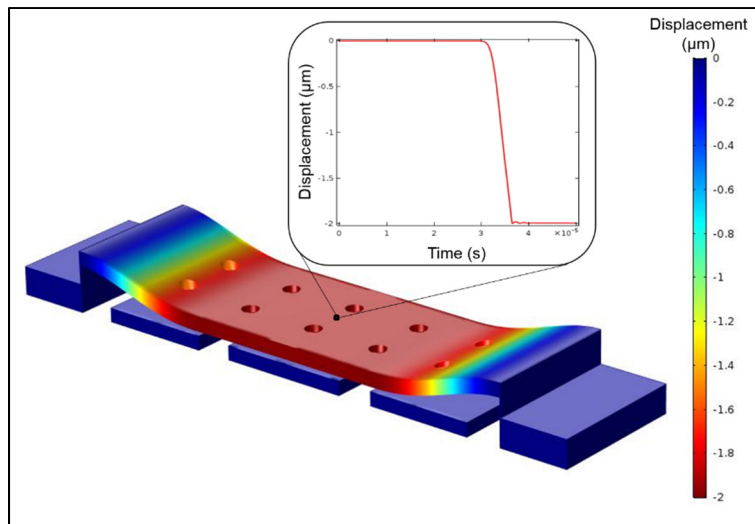


Figure 4.8 Membrane collapse

After collapse, the capacitance between the membrane and the RF line rises. A small voltage (1 mV) is therefore applied to the RF line to simulate the switch capacitances. This voltage is low enough and does not cause the switch's auto-actuation. Figure 4.9 shows the RF switch capacitance variation as a function of the time. An abrupt change in the capacitance value from 50 fF to 1.04 pF and 1pF are obtained for the membranes without and with holes respectively.

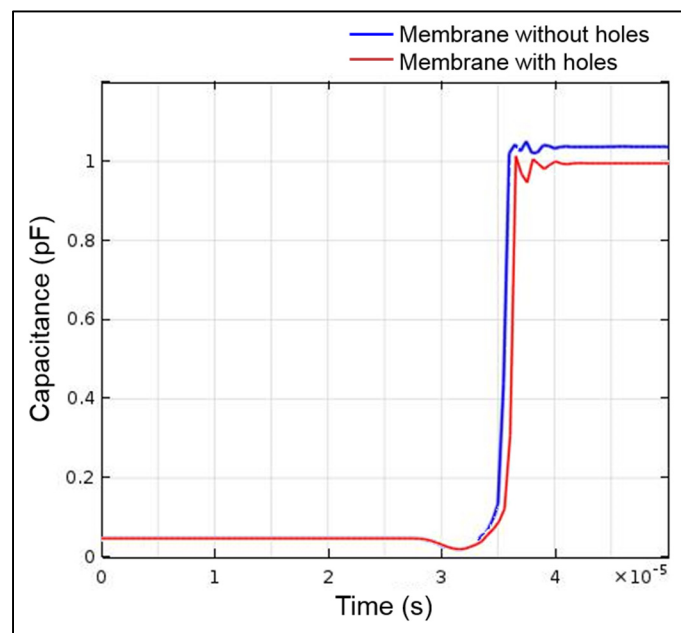


Figure 4.9 RF MEMS switch capacitance

4.3.2 RF MEMS-on-LTCC switch fabrication

We have attempted to fabricate the RF MEMS-on-LTCC switch depicted in figure 4.5 using the process detailed in section 4.2. To do so, we have fabricated and polished several LTCC substrates based on LACIME in-house basic process as detailed in chapter 2. Then, we built several iterations of the switch while trying to avoid the common fabrication challenges stated in section 4.2, mainly membrane stress and pin holes problems. Figure 4.10 shows an example of the different layers forming the switch and figure 4.11 present a 3D view of the final circuit's central part. Here, DC biasing circuits are shown.

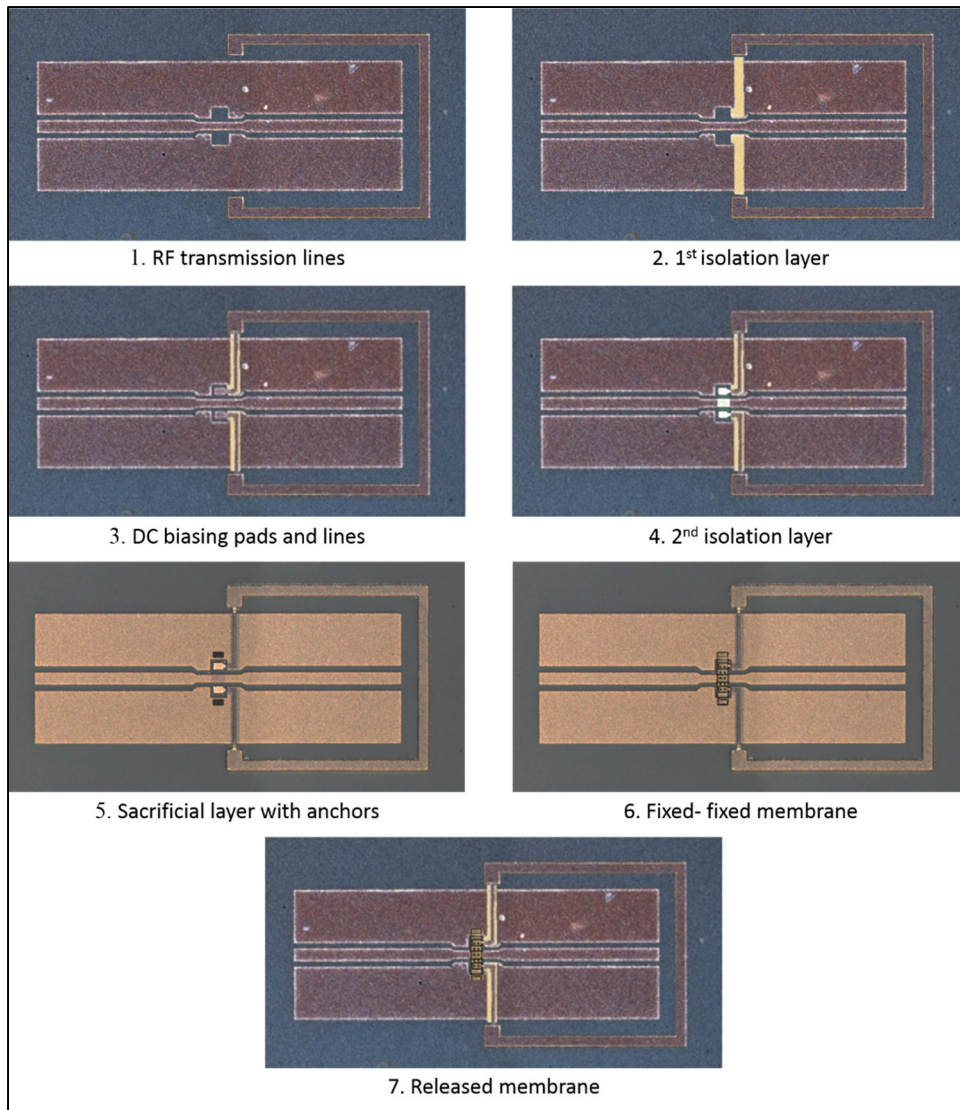


Figure 4.10 MEMS-on-LTCC switch fabrication steps

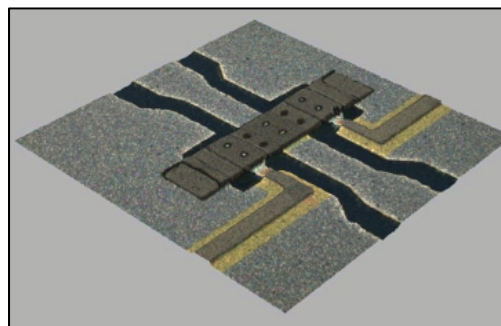


Figure 4.11 3D view of the MEMS-on-LTCC switch central part

While we have succeeded in obtaining stress-free membrane as shown in figure 4.11, the fabricated RF switch still suffers from the presence of pin holes and short circuits occur when it is actuated. Therefore, its mechanical and RF characterisation were not possible. Further fabrication runs were not possible because of some technical problems within some machines.

4.4 Conclusion

Considering the benefits of using LTCC as a substrate for the manufacturing of RF MEMS components, we detailed the various steps required for the development of such process. For instance, surface micromachining technique was used. Several challenges were encountered during the process development. We mention, basically the planarization of the LTCC surface, membranes' stress and pin holes. This process was then used to fabricate the capacitive RF MEMS switch designed in chapter 3. For mechanical characterisation and to prevent potential failure, we performed electro-mechanical study that was later confirmed through COMSOL Multiphysics simulation. Then, required masks were generated and several fabrication iterations were made.

EXPERIMENTAL RESULTS AND APPLICATIONS

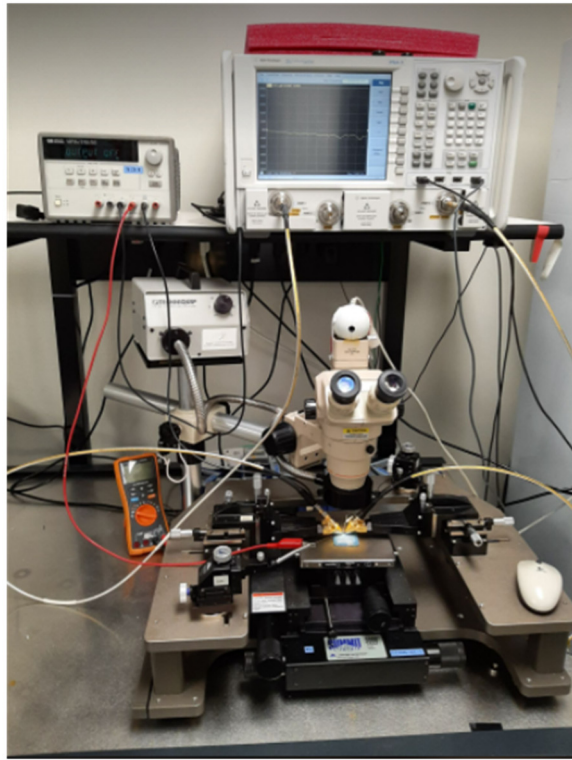
5.1 Introduction

Design and simulation of fluidic and MEMS basic cells and entire tuners on LTCC substrates have been presented in chapter 3. For validation purposes, in this chapter we propose to fabricate and measure the fluidic circuits, which was introduced in chapter 3 using our in-house LTCC process (presented in chapter 2). Measurement setups are first introduced and the fabricated circuits and their measured S-parameters are then presented. As an application of the designed tuners, we demonstrate their integration these in the design of RF reconfigurable amplifiers.

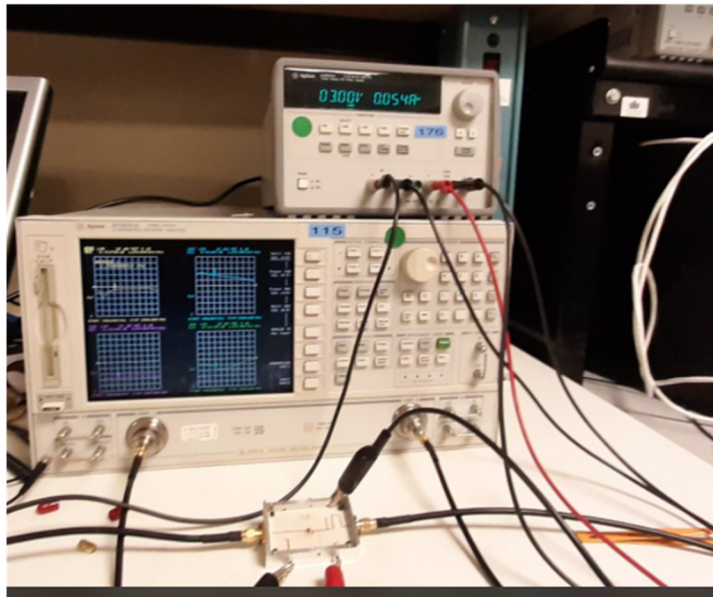
5.2 Fabrication and measurements

5.2.1 Measurement setups

The fabricated circuits were measured with a PNA-X or a VNA network analyzer in the required frequency band. While a probe station with GSG probes was used to measure the MEMS based circuits and the fluidic cell, cables with standard SMA connectors were employed for the fluidic tuner. For the fluidic circuits, few microliters of DI-water were injected/extracted manually to/from the required cavities with a syringe. As for the MEMS components, DC probes connected to external DC power supply were used. Figure 5.1 shows examples of the used test benches.



(a)



(b)

Figure 5.1 Measurement setups: a) PNA-X probe station and b) VNA test bench

5.2.2 Fluidic circuits

5.2.2.1 Fabricated circuits

Multiple tapes of DuPont 951 are employed to form the 3D fluidic cell and tuner (described in chapter 3) according to the LTCC process flow. Particularly, silver paste is used to print the outer and inner conductors and to fill the vias. Rectangular and circular shapes are laser drilled on the required tapes to form the necessary fluidic channels, inlets and outlets. To maintain the structural integrity during the stacking and laminating steps, fugitive carbon tapes are used to fill the inner and outer cavities respectively. They sublimate at 600 °C during the sintering step leaving behind empty channels. Figure 5.2 shows the fabricated fluidic circuits.

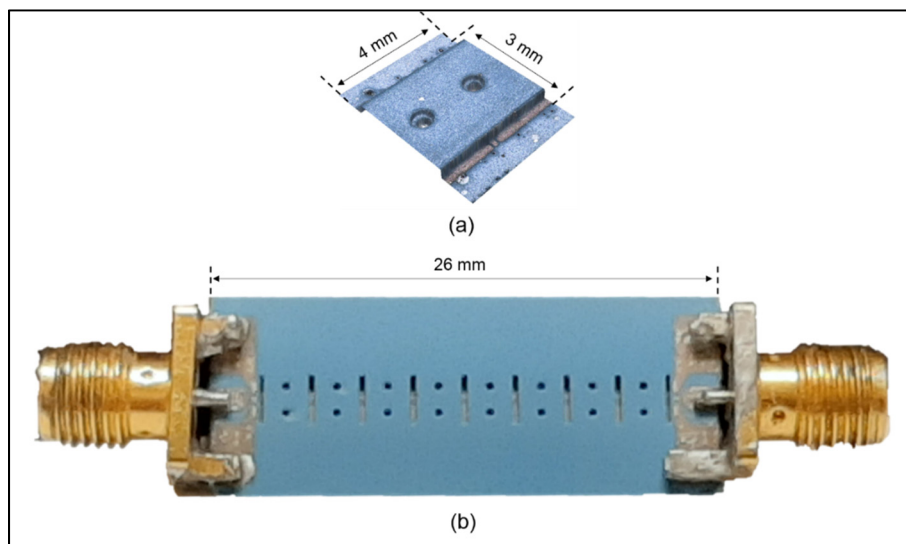


Figure 5.2 Fabricated fluidic: a) single cell and b) complete tuner

Layer misalignment was observed in the fabricated circuits. Most importantly, we observed a misalignment of about 50 μm in the x direction on the top layer. Figure 5.3-a shows the input and output tapered CPW transitions which were supposed to be symmetric measuring 250 μm each. Instead, one measures 200 μm while the other measures 300 μm . To investigate the volumetric misalignment, an X-ray image of the vertical transition at one of the tuner's ports was taken as shown in figure 5.3-b. While this figure reveals misalignment on different layers,

particularly at the cavities' level, there is overall continuity between the middle layers and the top surface. The observed misalignment is expected to impact the measurement results.

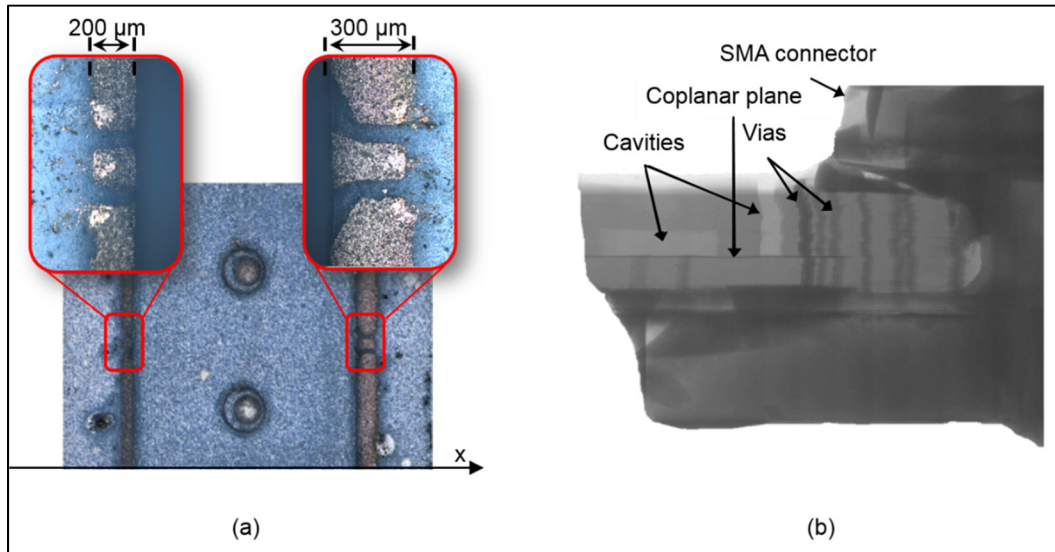


Figure 5.3 Fluidic circuits' fabrication issues: a) cell layer's misalignment (optical microscopy view) and b) tuner vertical transition's misalignment (X-ray view)

5.2.2.2 Measurement results

The fabricated fluidic circuits, single cell and entire tuner, were measured between 0.9 GHz and 2.4 GHz. Figure 5.4 shows a superposition of the measured (blue dashed curves) and simulated (red solid curves) S-parameters of a single fluidic cell for both the empty and water-filled cavity states. Here, a 1 μm of surface roughness was taken into account in the electromagnetic simulations. The difference between the measured and simulated insertion loss is less than 0.2 dB over the entire frequency range (figure 5.4-a) while the measured and simulated input impedance track very well (figure 5.4-b). The small difference in insertion loss is attributed to the layer misalignment previously discussed.

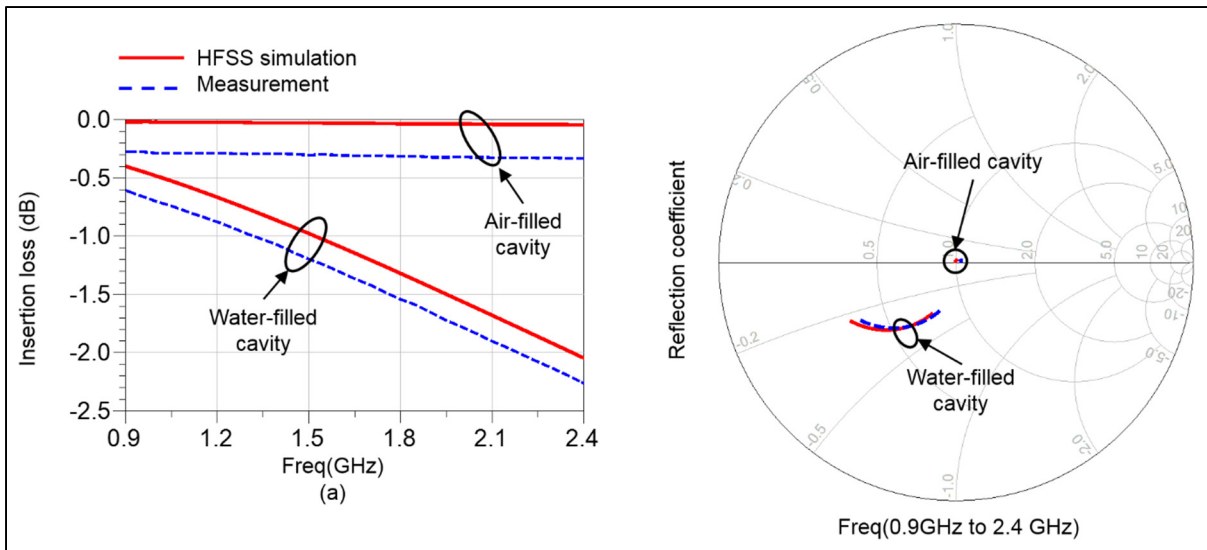


Figure 5.4 Fluidic cell measured and simulated: a) Insertion loss and b) reflection coefficient

For the measurement of the entire 8-cell impedance tuner, we follow a similar procedure to the one used for field simulation, namely, we measure a single cell in both states and cascade 8 measurement results in various combinations in ADS. The tuner's impedance coverages based on cascaded measurements and HFSS simulation are depicted in figure 5.5 for six frequency points in the range of [0.9 – 2.4 GHz]. The measurement results show a contracted coverage compared to HFSS simulations, particularly at low frequencies. This is attributed to the non-conformity of the fabricated and designed circuits due to the LTCC fabrication errors, as layer misalignment observed for a single cell. This causes minor losses in both states as shown in figure 5.4-a. Cascading cells results in losses accumulating, which leads to slight movements of impedances toward the Smith chart center. Still, the tuner offers good impedance coverage and is able to provide reconfigurability at low RF frequencies. It should be noted that the transition misalignment effect is not taken into account in these results as the transition was not fabricated separately. Indeed, the data item modeling the defect free transition, simulated with HFSS software, was used for the results depicted in figure 5.5.

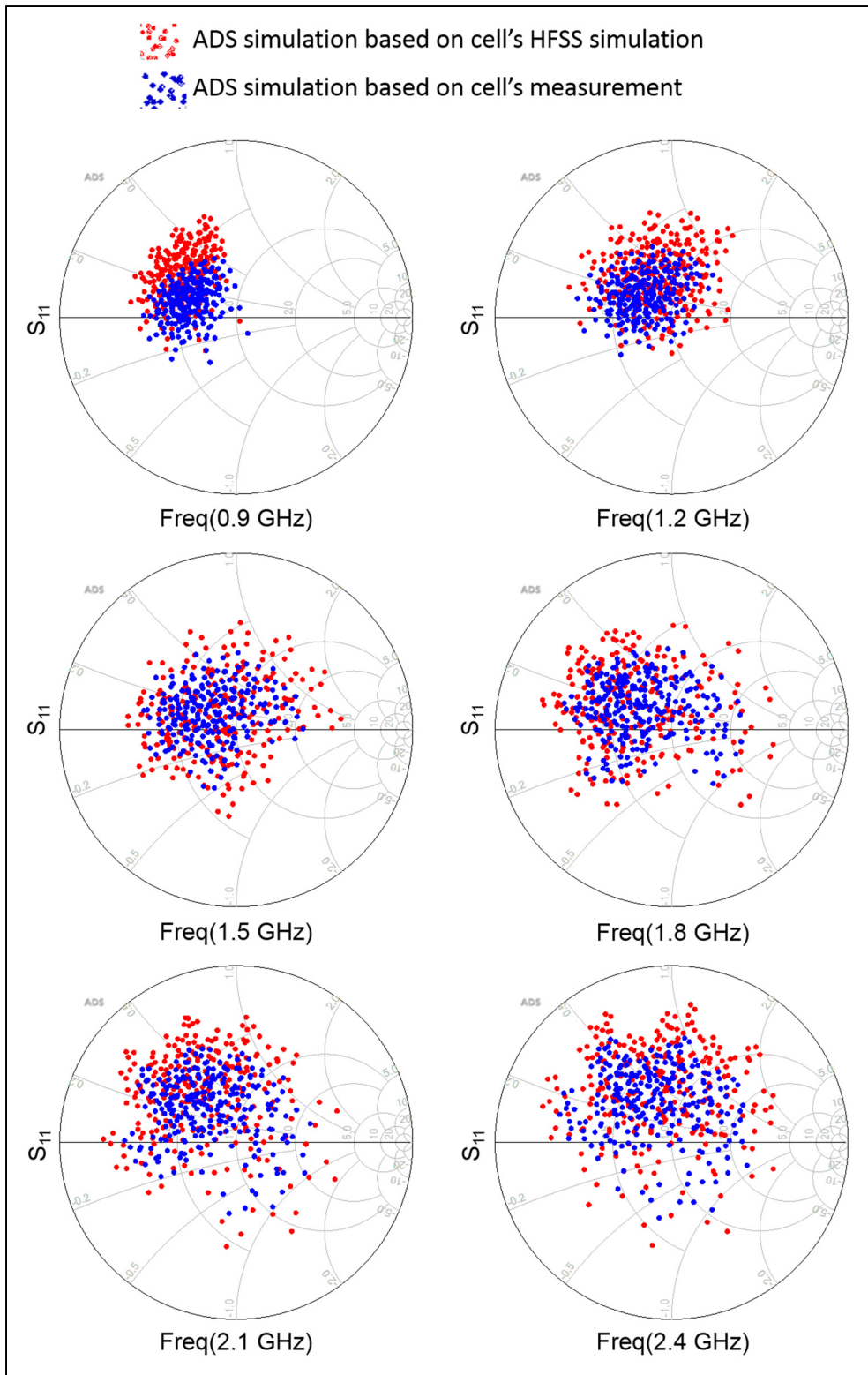


Figure 5.5 Fluidic tuner measured and simulated impedance coverage

To further validate the operation of the tuner, we consider 4 arbitrary tuner states, among the possible 256, as follows: all the cells are empty, all the cells are DI-water filled, cells C1, C2, C5 and C7 are empty, and cells C2, C6, C7 and C8 are empty. Next, we measure the actual fabricated tuner's response (insertion loss and reflection coefficient) for these states from 0.9 GHz to 2.4 GHz. Figure 5.6 shows these measurements (red solid curves) and compares them to those predicted by cascading the single cell measurements in ADS (blue dotted curves) for the same states. Overall good agreement is observed and the minor differences are attributed to: (i) the expected variability of the fabricated cells, they are not as identical as when they are cascaded in ADS; and (ii) vertical transition misalignment as shown in figure 5.3 which is not taken into account in the cascaded cells in ADS. Therefore, given the closeness of both results and given the complexity and time-consuming nature of measuring the fabricated tuner's impedance coverage (256 states) at all frequencies, the ADS cascading of single measured cells can be used for design purposes.

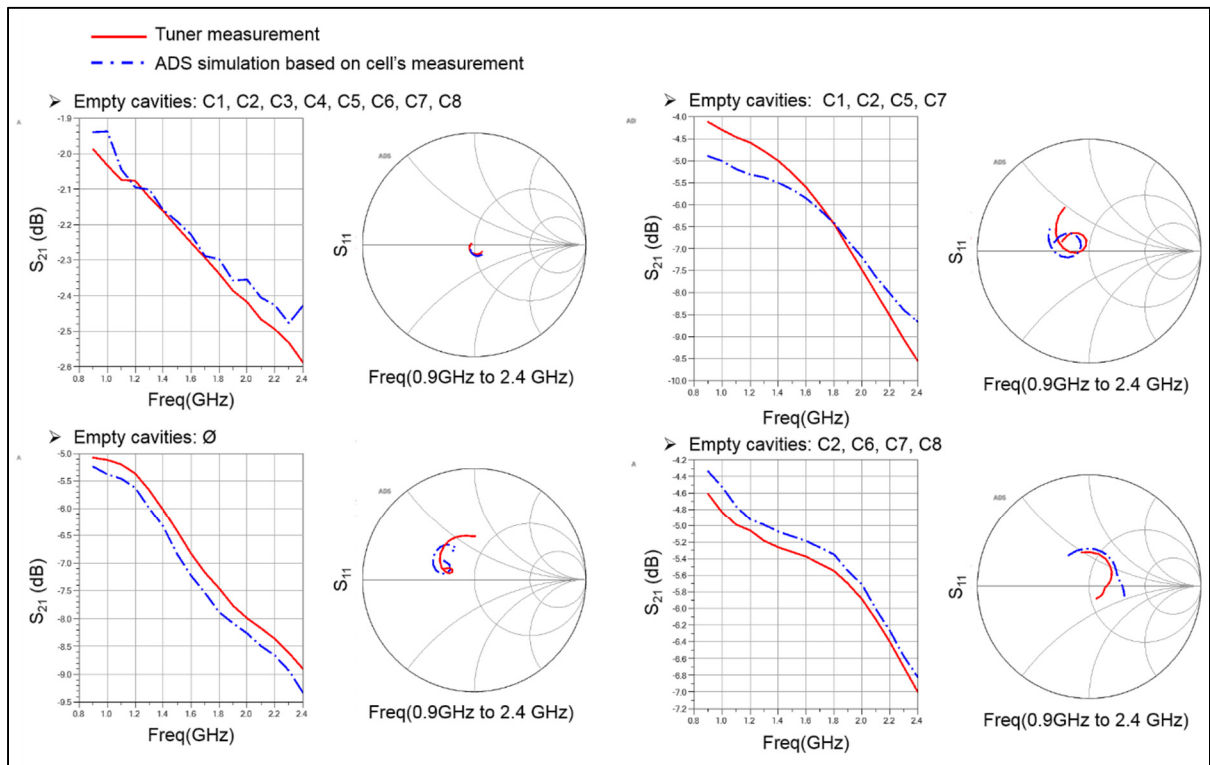


Figure 5.6 Fluidic tuner simulated and measured insertion loss and reflection coefficient when some cells are DI-water filled

5.3 Application: frequency reconfigurable RF amplifiers

As stated in chapter 1, making an RF amplifier reconfigurable requires the input and/ or output matching networks to be tunable. This way, multiple values of source and load reflection coefficients (Γ_S and Γ_L) may be provided to the transistor at the target frequencies as illustrated in figure 5.7. Here, we demonstrate how the proposed fluidic and MEMS based impedance tuners can be used to achieve reconfigurable RF amplifiers.

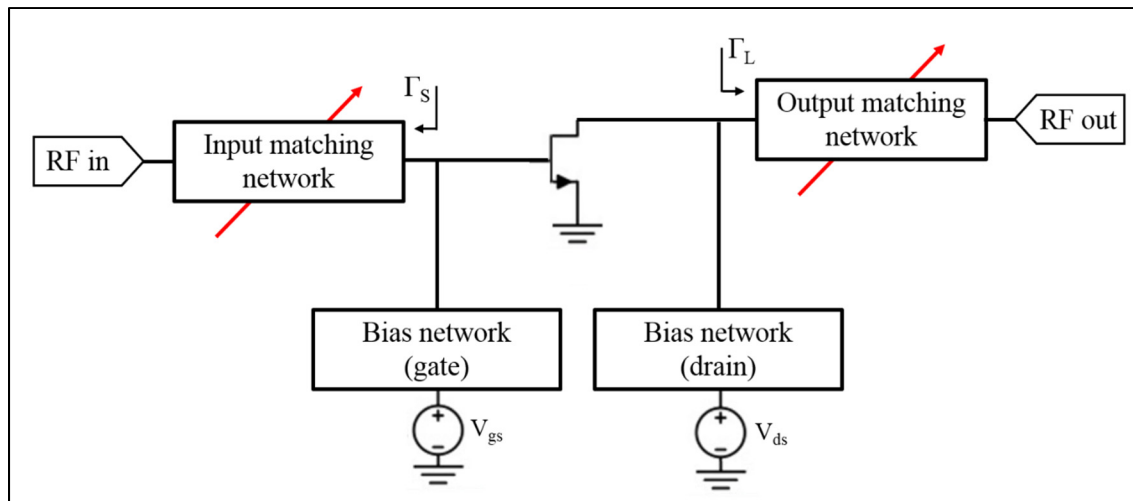


Figure 5.7 Reconfigurable amplifier block diagram

5.3.1 Reconfigurable fluidic RF amplifier

Here, we propose the design of a fluidic-based RF amplifier that is able to cover the 0.9 to 2.4 GHz frequency range. To illustrate this, we selected an Avago E-PHEMT (Enhancement mode Pseudomorphic High Electron-Mobility Transistor) surface mount unmatched transistor, the ATF-58143. The transistor datasheet is ambiguous. Therefore, we used the measured S-parameters of our in-house module where the transistor was biased under the quiescent point ($V_{ds}=3$ V, $I_{ds}=40$ mA ($V_{gs}=0.54$ V)) and stabilized with a pair of resistors at the input. Simulations were then carried out to determine the required source and load matching impedances to reach the maximum available gain (i.e. simultaneous input and output conjugate match impedances) over the frequency range of interest. It was found that the required load

impedance varied little and was close to 50Ω while the necessary source impedance varied considerably and could not be achieved with one fixed matching circuit (figure 5.8).

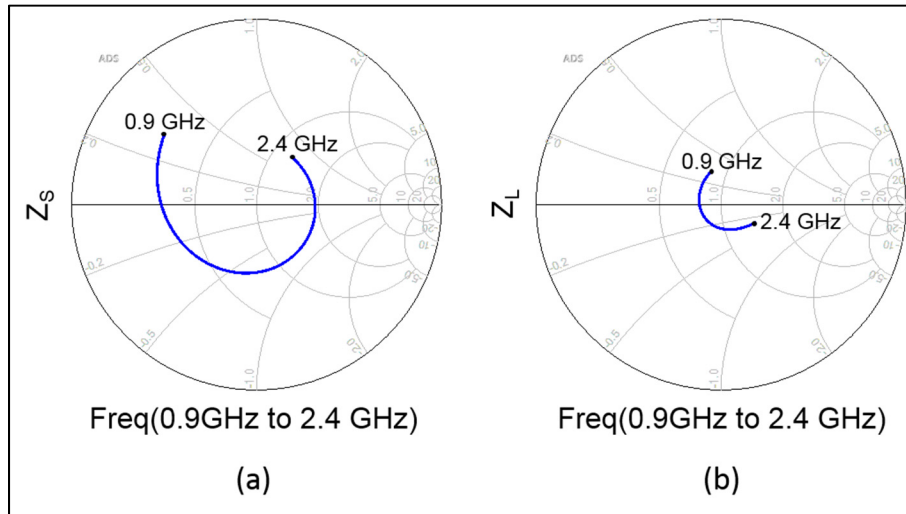


Figure 5.8 Required impedances in the ATF-58143 transistor:
a) input and b) output

Therefore, we decided to use the fluidic tuner for the input matching and used a fixed transmission line and an open stub for output matching. This results in a slight change in the transistor required source impedances. Figure 5.9 shows the variation of the required source impedance versus frequency (red solid curve), and identifies with black dots the exact impedance at three frequencies chosen in the targeted frequency range: 1.2 GHz, 1.6 GHz and 2.2 GHz. The achievable impedances with the fluidic tuner are also shown on the same plots (scattered blue dots). We notice that the tuner may provide impedances equal or adjacent to the required source impedances for the considered frequencies. Tuner's impedance (green dot) closer to the required source impedance (black dot) is therefore selected for each frequency. Their values are summarized in table 5.1.

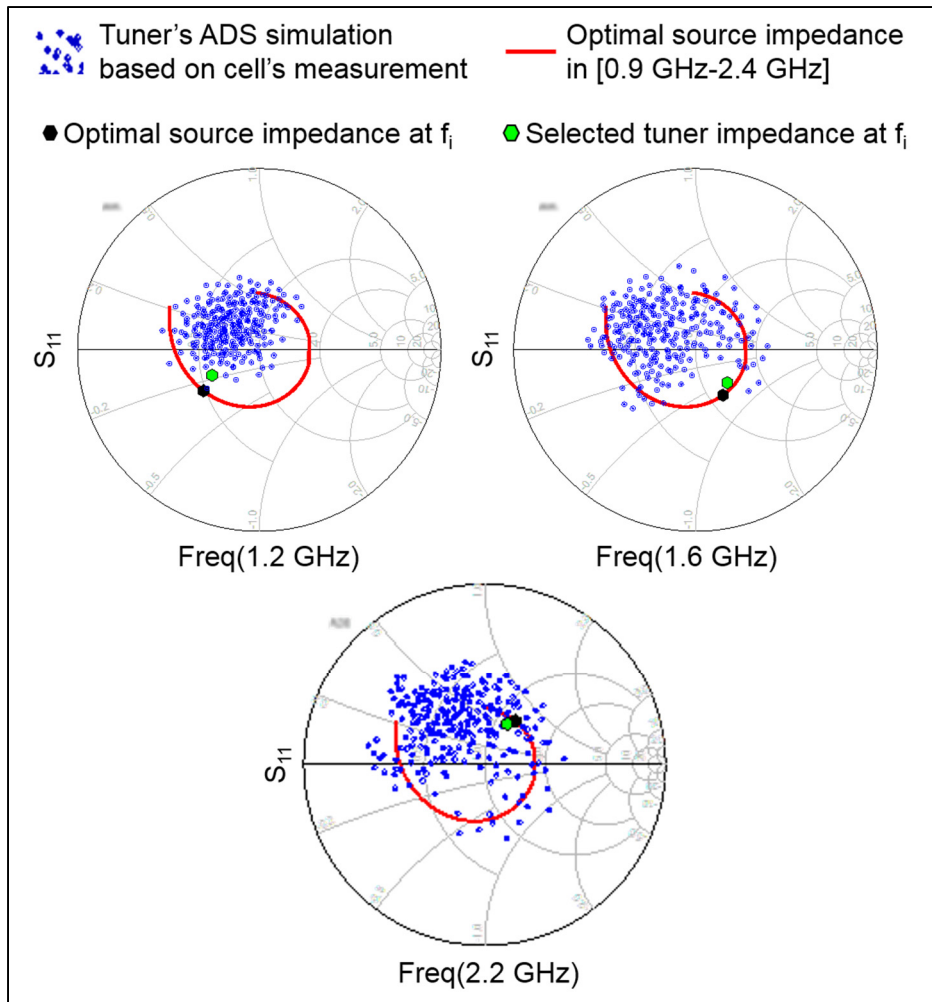


Figure 5.9 Tuner impedance coverage, optimal source impedance and selected impedance at different frequencies

Table 5.1 Optimal source impedances and tuner's selected impedances

| Frequency | Optimal source impedance | Tuner's selected impedances |
|-----------|--------------------------|-----------------------------|
| 1.2 GHz | $24.35 - j 12.8$ | $28.4 - j 8.7$ |
| 1.6 GHz | $58.45 - j 31.9$ | $63.65 - j 25.35$ |
| 2.2 GHz | $61.15 + j 31.85$ | $57.35 + j 27.15$ |

The reconfigurable fluidic amplifier design, therefore, consists of integrating the fluidic tuner as an input MN with the rest of the circuit being realized with conventional transmission lines and surface mount components. Indeed, it is first designed and simulated based on ADS

circuit/EM co-simulation of the pre-matched amplifier (i.e. transistor with its stability, biasing and output matching circuitry) and fluidic tuner's ADS simulation based on cell's measurement. Then, the entire reconfigurable amplifier circuit is fabricated on a single LTCC substrate in one run using the process described previously. Figure 5.10-a shows a 3D view of the complete amplifier while figure 5. 10-b shows the fabricated circuit with mounted discrete components.

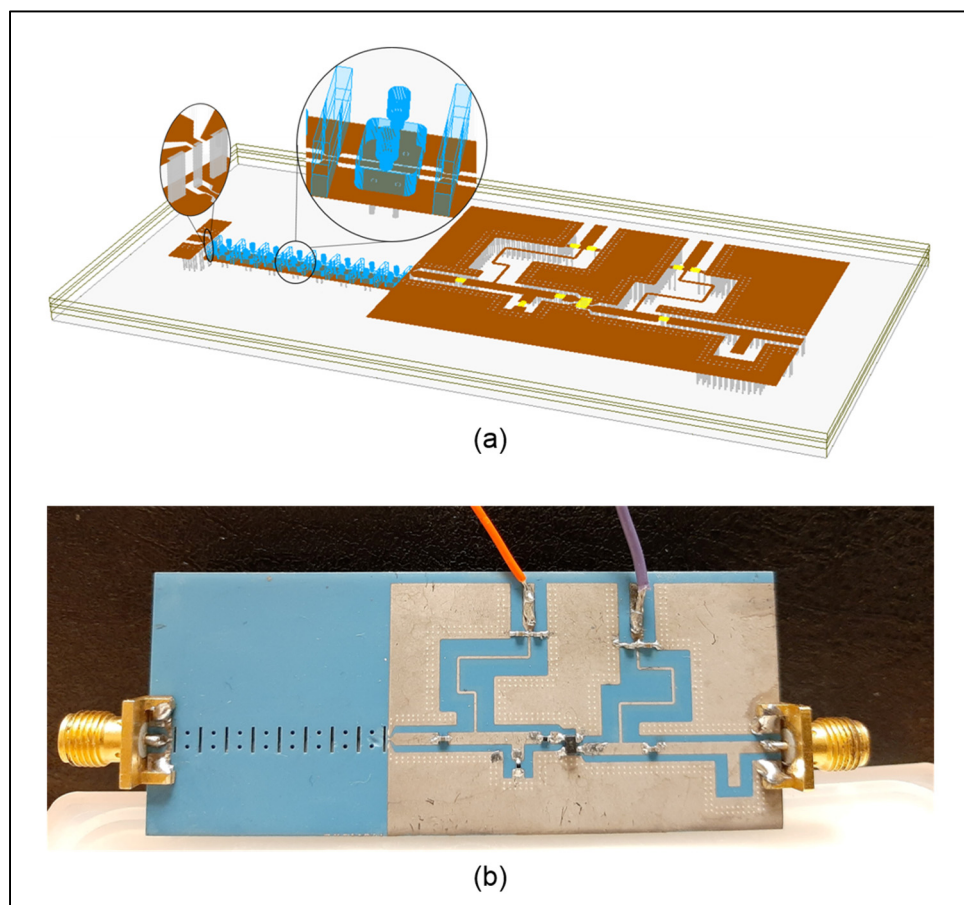


Figure 5.10 Reconfigurable RF fluidic amplifier: a) 3D view and b) fabricated circuit

A proper choice of the tuner cells' states to provide the required input impedances leads to reach high gain and maintain good input and output matching at different frequencies between 0.9 GHz and 2.4 GHz. Based on the results of figure 5. 9, we determined that to match the amplifier at 1.2 GHz, cells C1, C6, C7 and C8 must be filled with DI-water while the remaining

cells stay empty. Similarly for 1.6 GHz, C3, C5, C7 and C8 must be filled with DI-water and the others empty. Finally, for 2.2 GHz, cells C5, C7 and C8 must be filled with DI-water with the other empty. Figure 5. 11 shows the simulated and measured gain, group delay, input and output return loss for the three frequencies. Better than 20 dB input return loss was achieved at the three frequencies while the measured gain was slightly less than simulation due to the loss issues discussed previously. Both measurement and simulations show a group delay of less than 1.5 ns for the three scenarios.

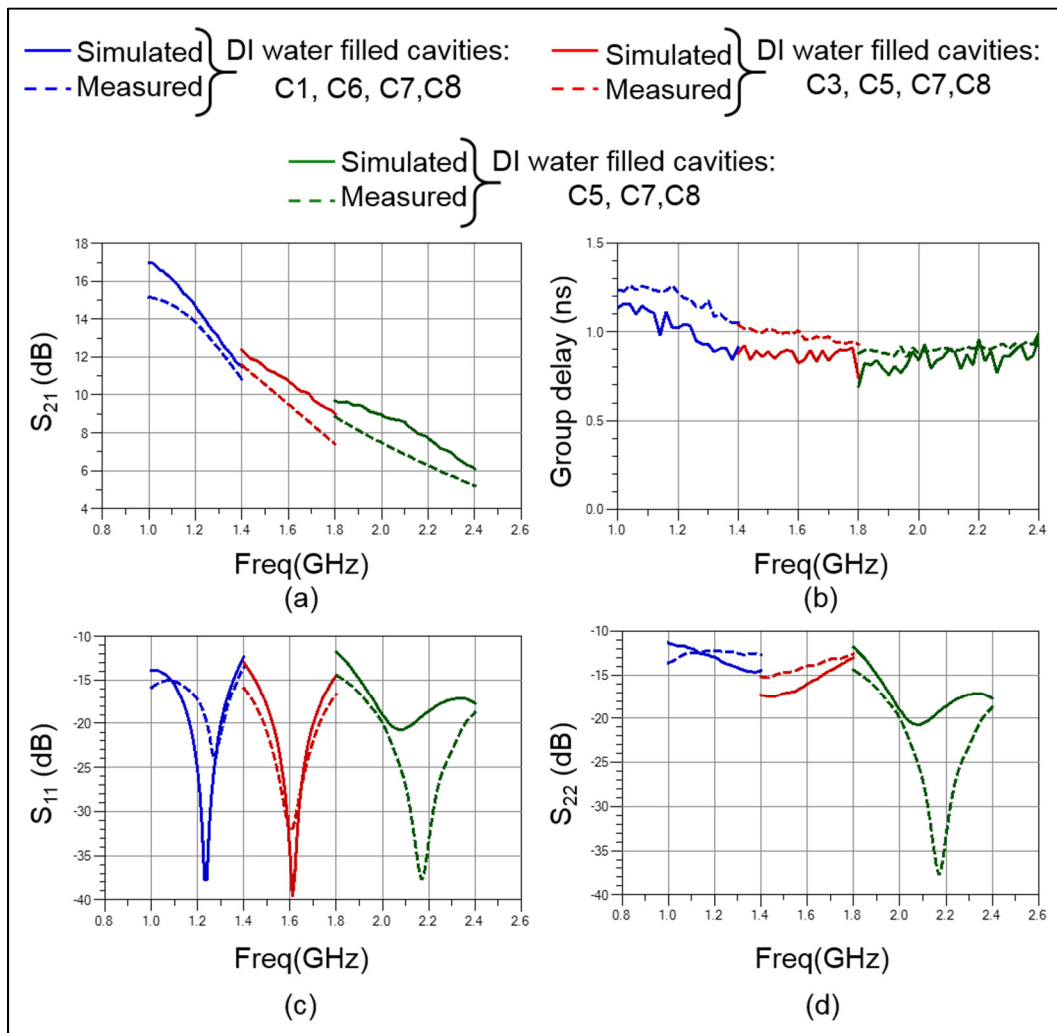


Figure 5.11 Reconfigurable fluidic RF amplifier simulated and measured: a) gain, b) group delay, c) input return loss and d) output return loss

5.3.2 Reconfigurable MEMS-on-LTCC RF amplifier

Taking advantage of the MEMS-on-LTCC tuner, we demonstrate the reconfigurability of an RF amplifier between 2 and 7 GHz. In this context, we used a SiGe HBT (high-performance Silicon Germanium Heterostructure Bipolar Transistor) surface mount unmatched transistor from Qorvo, the SGA8343Z. It was biased at $V_{CE}=3$ V and $I_{CE}=20$ mA and stabilized with a series resistor at the transistor's input. To ensure high isolation between the RF and DC paths, we employed surface mount ultra-wideband bias tees (the TCBT-123+ from mini-circuits) with bypass capacitors. Here, similarly to the fluidic reconfigurable amplifier, we target to reach the maximum available gain at four frequency point in the 2 to 7 GHz frequency range: 3 GHz, 4 GHz, 5 GHz and 6GHz. The required input and output impedances for simultaneous conjugate matching of the unmatched amplifier have been obtained through ADS simulation where fabricants' models of the surface mount components (transistor, resistor, capacitances, and bias tees) were used, and are shown in figure 5.12. Both of them vary considerably in the [2 GHz - 7GHz] frequency band.

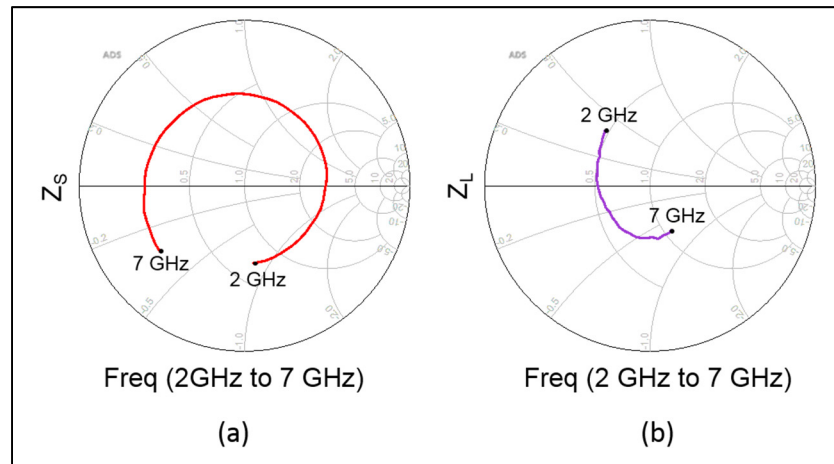


Figure 5.12 Required impedances for simultaneous conjugate matching of the SGA8343Z transistor: a) input and b) output

Consequently, we consider both input and output impedance matching based on the second iteration of the 3D MEMS-on-LTCC tuner. Since we were not successful in fabrication of a fully functional tuner, we used HFSS and ADS co-simulation to demonstrate the expected

performance. Figure 5.13 shows the tuner coverage (scattered blue dots) and the variation of the required source and load impedances (red and purple solid curve respectively) at the target frequencies. In the same plots, we identify the required source and load impedances using black dots and triangles respectively. Green dots and triangles correspond to the tuner's chosen impedances for source and load matching respectively. As shown, impedances close to the desired ones may be provided by the tuner at different frequencies for input and output matching. Table 5.2 summarize the obtained values.

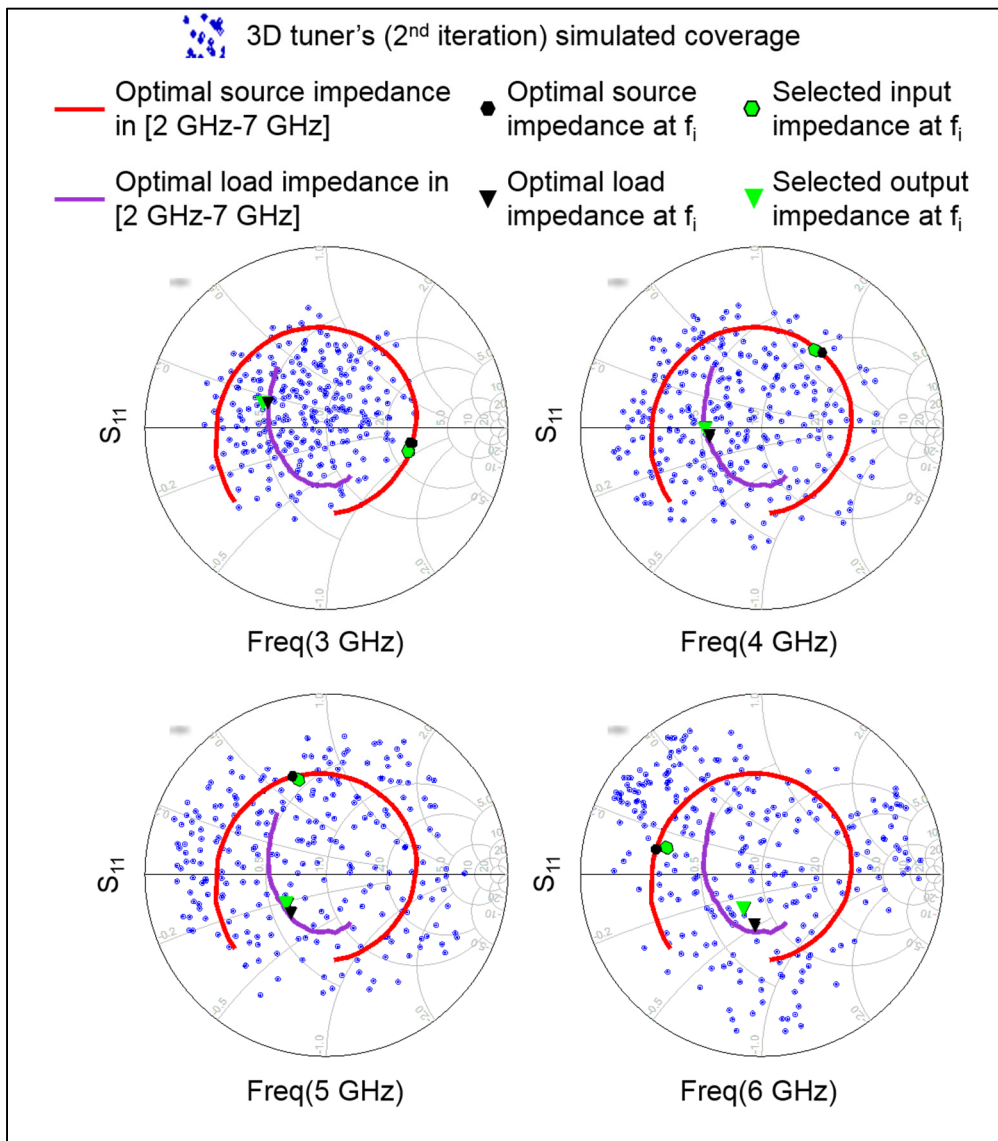


Figure 5.13 MEMS-on-LTCC tuner impedance coverage, optimal source and load impedances and selected impedances at 3GHz, 4GHz, 5 GHz and 6 GHz

Table 5.2 Optimal source, load and MEMS-on-LTCC tuner's selected impedances

| Frequency | Optimal source impedance | Tuner's selected input impedance | Optimal load impedance | Tuner's selected output impedance |
|-----------|--------------------------|----------------------------------|------------------------|-----------------------------------|
| 3 GHz | $136.1 - j 29.9$ | $133.56 - j 24$ | $25.27 + j 6.4$ | $23.72 + j 5.62$ |
| 4 GHz | $57.27 + j 66.27$ | $53.97 + j 63.53$ | $27.34 - j 5.03$ | $26.22 - j 2.09$ |
| 5 GHz | $19.93 + j 31.67$ | $22.06 + j 32.64$ | $30.52 - j 15.77$ | $30.09 - j 13.17$ |
| 6 GHz | $12.68 + j 5.44$ | $15.04 + j 6.21$ | $38.27 - j 26.89$ | $37.53 - j 18.86$ |

Two 3D MEMS-on-LTCC tuners, were therefore added at the input and output of the un-matched amplifier as impedance matching networks. Figure 5.14 gives a 3D view of the resulting MEMS-on-LTCC reconfigurable RF amplifier. While the tuners were represented by their cascaded S-parameters HFSS/ ADS field-simulation, operation of the un-matched amplifier was characterised based on ADS/ HFSS circuit and EM co-simulation. Here, S-parameters' models of the surface mount devices (transistor, bias tees, resistances, capacitors) provided by the manufacturer were used.

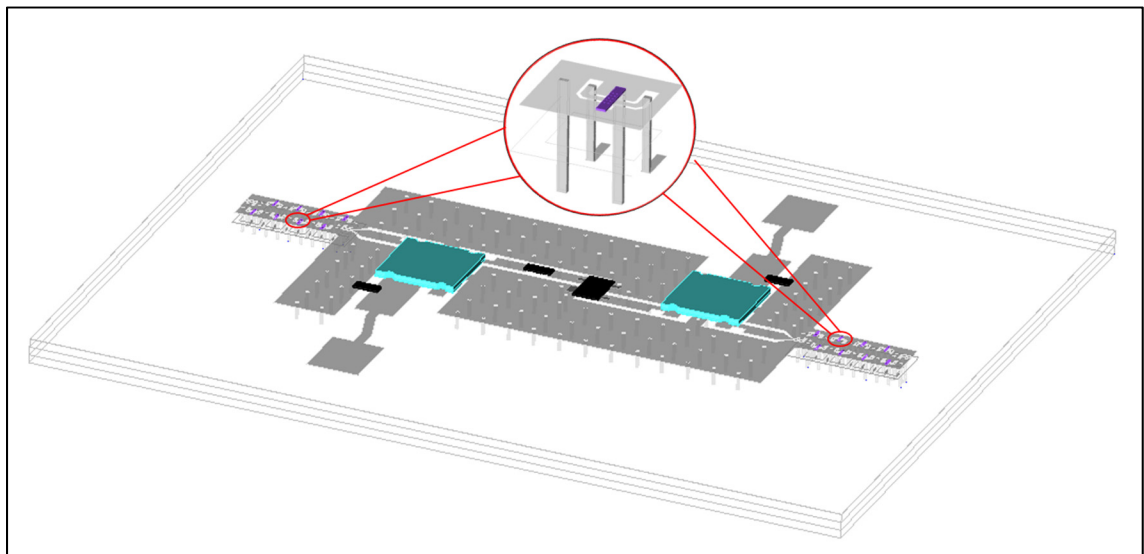


Figure 5.14 Reconfigurable RF MEMS-on-LTCC fluidic amplifier 3D view

To provide the impedances detailed in table 4.2, we searched for the appropriate tuner configurations. Various combinations of up and down states were performed according to these

configurations as depicted in figure 5.15. The resulting gain, group delay, input and output return loss are thereby shown. The gain reached at the four targeted frequencies was very close to the maximum gain. Better than 15 dB input and output return loss were achieved at the four frequencies. A group delay less than 1 ns was obtained. Here, we focussed only on certain frequency points. Considering more tuner configurations, better performance may be obtained.

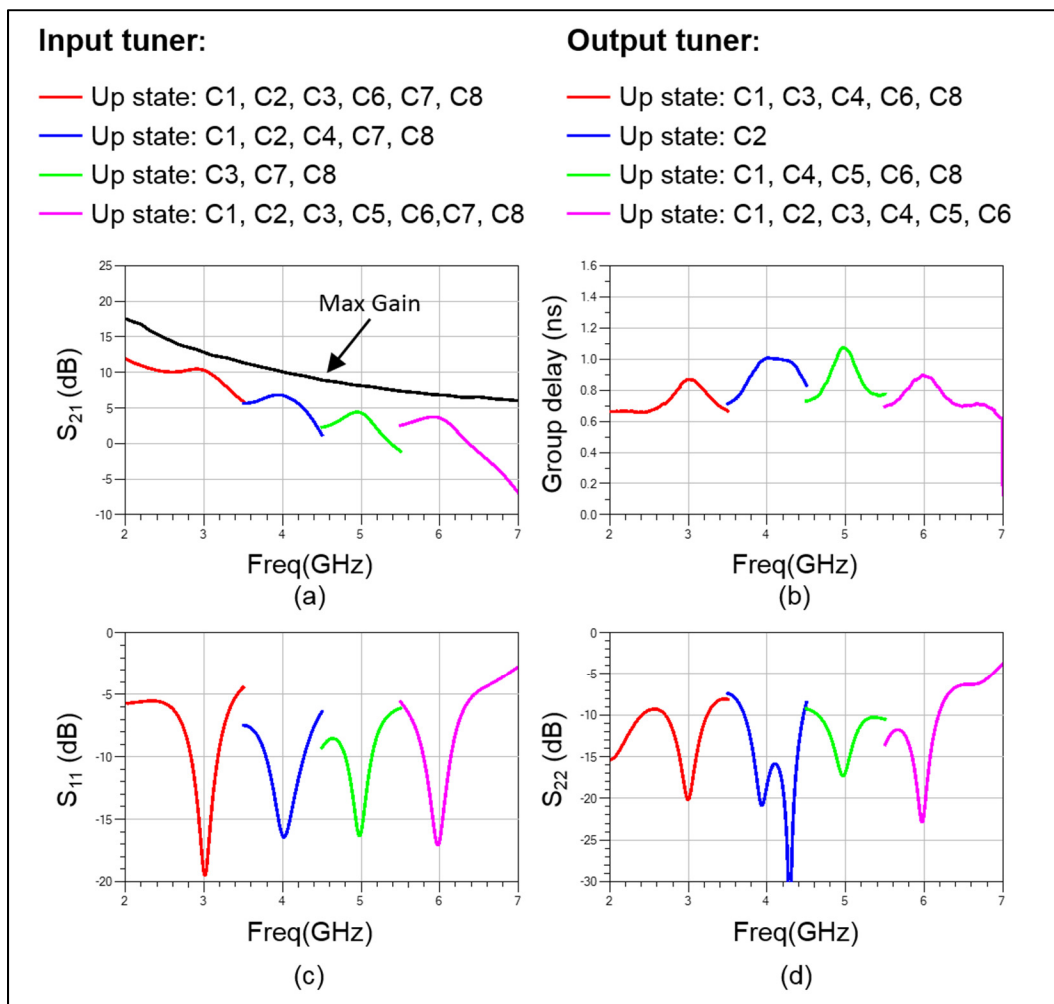


Figure 5.15 Reconfigurable MEMS-on-LTCC RF amplifier simulated: a) gain, b) group delay, c) input return loss and d) output return loss

5.4 Conclusion

Measured results of the fabricated fluidic single cell and 8-cell impedance tuner were found to be in close agreement with simulations and demonstrated generally good performance. Minor

disagreements were attributed to fabrication errors related to LTCC technology. The fluidic and MEMS tuners were then used to demonstrate the reconfigurability of a RF amplifier at different frequencies in [0.9 GHz, 2.4 GHz] and [2 GHz, 7 GHz] respectively. Only one LTCC substrate was used to integrate each tuner with a pre-matched or un-matched amplifier. Using the same design algorithm and taking into account the 256 impedances that they provide at each frequency in their frequency range, they can be exploited to design various types of frequency reconfigurable amplifiers with different figures of merit

PERSPECTIVES FOR ENHANCED PERFORMANCE RF TUNERS

6.1 Introduction

Limited Smith chart coverage near the edges has been a main limitation in the design of RF tuners. Loss remains the most important factor behind this limitation. Because of this, it was seen with the tuners which we proposed in this work that, despite their wide coverage, they cannot reach the Smith chart's outer edge. Moreover, for both fluidic and MEMS-on-LTCC tuners, we have used manual control (water injection and DC polarization). In this chapter, we investigate ways to reduce losses and extend Smith chart coverage by introducing low-loss air-filled transmission lines and metallic fluids as candidates to enhance performance of the MEMS-on-LTCC and fluidic tuners, respectively. We also propose modules to automate the control of both types of tuners.

6.2 Air-filled 3D MEMS-on-LTCC tuner

Transmission lines and waveguides with low losses, small sizes and easy integration capabilities have always been essential for high frequency applications. We distinguish three types of loss mechanisms: radiation, metal and dielectric losses. The contribution of dielectric losses to the attenuation constant of a guiding structure can be significant and depends on the the geometry and dielectric material used. Here, we propose a novel type of air-filled stripline designed using LTCC multilayer technology (Bahloul & Kouki, 2019). It consists of replacing the dielectric surrounding the signal conductor by air to suppress or minimize the dielectric losses. It is then integrated in the design of the MEMS-on-LTCC tuner to seek wider spread of the Smith chart coverage.

6.2.1 Air-filled stripline design

6.2.1.1 General overview

By leveraging the LTCC's capability to form buried air-filled cavities, making suspended striplines becomes feasible. Similar to conventional solid dielectric-filled striplines (figure 6.1-a/c), the air-filled line (figure 6.1-b/d) consists of a signal conductor surrounded by air as dielectric region with top and bottom ground planes. The whole circuit is enclosed on a ceramic substrate. The ground planes are connected through two arrays of circular via holes in the LTCC substrate, forming thereby a cage around the signal line and avoiding floating grounds and parallel plate modes. A very thin dielectric layer (membrane) is added as a support of the signal line (figure 6.1-d).

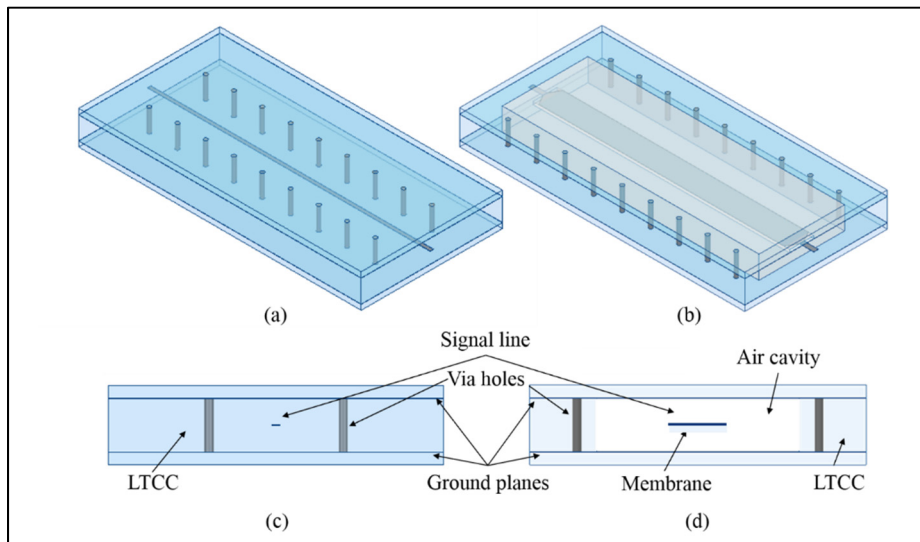


Figure 6.1 Stripline: a) dielectric-filled 3D view, b) air-filled 3D view, c) dielectric-filled side-view and d) air-filled side-view

6.2.1.2 Design and dimensioning

Both air-filled and dielectric-filled striplines are designed using multiple layers of DuPont 951 as shown in the simplified architecture of figure 6.2. The substrate thickness (B) (or the air cavity depth) is set to eight 4.5 mils layers. The floating conductor's width (w_{st}) is estimated

using transmission line calculators to obtain 50Ω transmission lines. The air cavity width (w_a) and the grounds width are at least set to three times the conductor's width ($3 \times w_{st}$) to ensure that the electric and magnetic fields, shown in figure 6.2, are constrained within the desired region (air or dielectric). Only one 4.5 mil layer is used to print the central conductor of the air-filled structure. Consequently, its thickness is equal to $1/8$ of the air cavity depth, resulting in a negligible effect on the electric and magnetic fields distributions. The dimensions of the designed striplines are detailed in table 6.1.

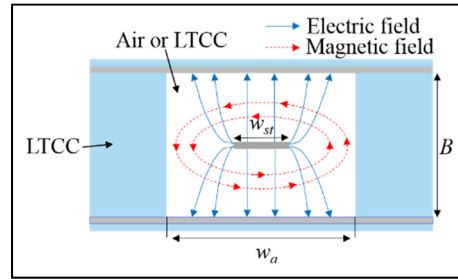


Figure 6.2 Stripline physical parameters and fields' distribution

Table 6.1 Air-filled and dielectric-filled stripline parameters

| Parameter | Value |
|---|-------------------|
| Air cavity depth: t | 1.727 mm |
| Air filled stripline width: w_{st} | 0.9 mm |
| Air cavity width: w_a | 3 mm |
| Dielectric filled stripline width: w_{st} | 120 μm |

6.2.1.3 Attenuation coefficient characterisation

The $50\ \Omega$ striplines shown in figure 6.1 have been modeled in HFSS software and their geometrical features have been tuned based on 3D field simulations to reduce losses. Their attenuation coefficients are then extracted from simulated S-parameters using (6.1) (Isapour & Kouki, 2017):

$$\alpha(\text{dB/cm}) = -8.685 \frac{\text{Ln}(|S_{21}|^2) - \text{Ln}(1 - |S_{11}|^2)}{2L} \quad (6.1)$$

where S_{21} and S_{11} are the transmission and reflection coefficients of the guiding structure and L its length.

Figure 6.3 shows a comparison between the attenuation constant of the air-filled and dielectric-filled striplines. Simulations are performed from 2 GHz to 7 GHz. As expected, lower losses are obtained from the air-filled stripline compared to its dielectric-filled counterpart. Although DuPont951 has very small dielectric loss ($\tan\delta = 0.006$), the gain provided by the air-filled stripline ($\tan\delta = 0$) is still considerable. In fact, as the signal propagates almost entirely in the air for the air-filled structures, its resulting attenuation coefficients is very small: less than 0.03 dB/cm up to 7 GHz. This level of loss is mainly due to the conductor losses, which are lowest for silver.

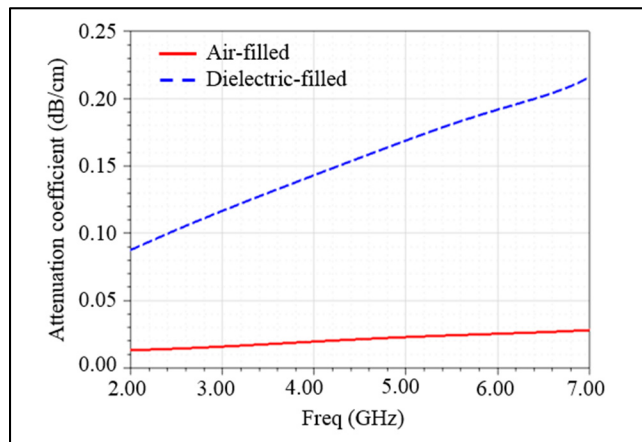


Figure 6.3 Simulated attenuation coefficients (dB/cm) of air-filled and dielectric-filled striplines

6.2.1.4 Stripline to upper layers transition

For interconnection and ease of access purposes, vertical CPW transitions (introduced in chapter 3) to CPW upper transmission lines are added to a 1 cm length dielectric-filled and air-filled striplines as shown in figure 6.4. The presence of various discontinuities due to the use

of different types of transmission lines (stripline and CPW) and dielectrics (LTCC and air) within the same circuit introduces undesired reflections. Hence, dimensions of both guiding structures were tuned to keep the lowest attenuation coefficients while maintaining 50Ω impedance. Figure 6.5 shows the obtained results taking into account the added transitions and demonstrates that the air-filled structure still outperforms the dielectric-filled in losses with both providing better than 15 dB return loss over the entire band.

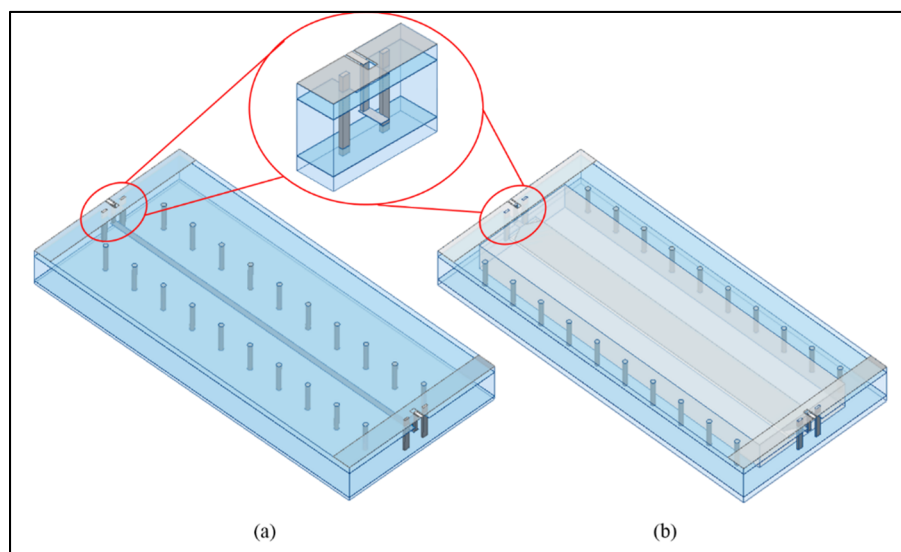


Figure 6.4 CPW vertical transition from CPW upper transmission line to buried: a) dielectric-filled stripline and b) air-filled stripline

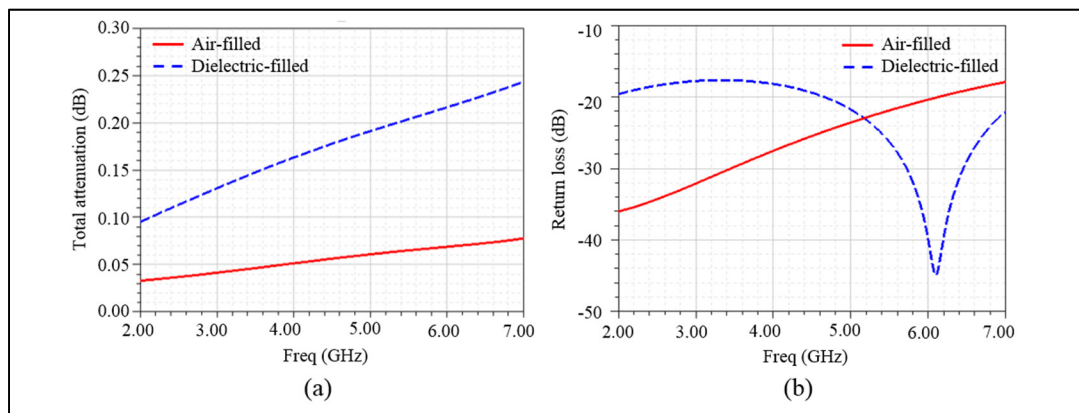


Figure 6.5 Simulated performance of air-filled and dielectric-filled structures with CPW transitions to CPWG lines: a) total attenuations and b) reflection coefficients

6.2.2 Air-filled MEMS-on-LTCC 3D tuner

The attenuation coefficient for a particular propagation medium or guiding structure is commonly referred to the physical length and given in dB/m. However, attenuation per electrical length is more significant in the design of RF and microwave circuits. In fact, changing the propagation medium (as the dielectric substrate) involves the use of the equivalent electrical parameters. Therefore, attenuations per wavelength (dB/ λ) for air-filled and dielectric-filled striplines have been simulated and depicted in figure 5.6. The air-filled stripline shows an attenuation coefficient of around 0.2 dB/ λ lower than its dielectric-filled counterpart from 2 GHz to 7 GHz. We note that, for both striplines, the attenuations per wavelength follow the wavelength variation and so decrease versus frequency.

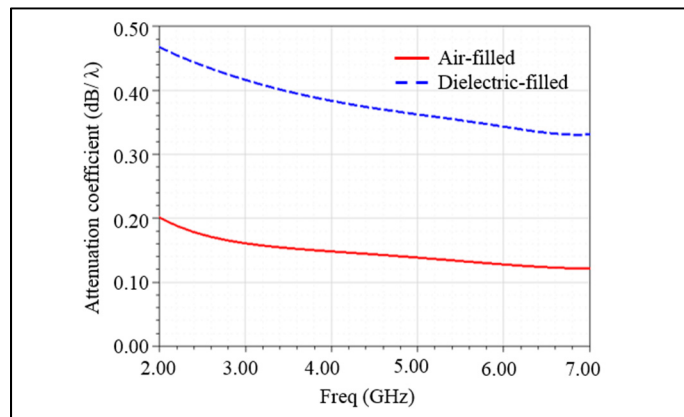


Figure 6.6 Simulated attenuation coefficients (dB/ λ) of air-filled and dielectric-filled striplines

As we aim to reduce losses in tuners, we propose another iteration of the MEMS-on-LTCC switch, where we integrate air-filled transmission lines. It consists of replacing a part of each stripline used in the architecture of the 3D switch depicted in figure 3.14 by its air-filled counterpart, as shown in figure 6.7. Hence, 1.17 mm length air-filled stripline was used instead of 0.4 mm dielectric-filled stripline, to ensure equivalent electrical lengths. Here, we employed the same LTCC stacking as the 3D switch and the air-filled structures (figure 6.1).

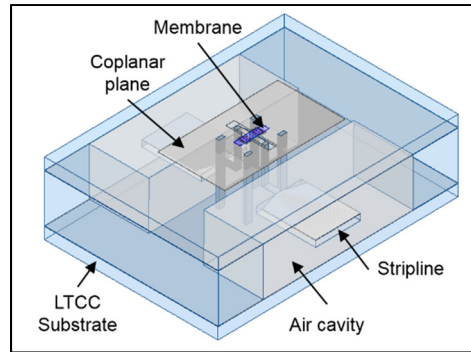


Figure 6.7 Air-filled 3D MEMS-on-LTCC switch

The air-filled 3D MEMS-on-LTCC switch was characterised based on HFSS electromagnetic simulation. As expected, although longer striplines were used, it represents less losses than its dielectric-filled counterpart. Lower insertion loss was obtained for both states as shown in figure 6.8-a. Figures 6.8-c illustrates higher reflection coefficient, at the down state, while maintaining the 50Ω impedance between 2 GHz and 7 GHz at the up state. Phase shifts shown in figure 6.8-b prove that both structures have the same electrical length, ensuring thus fair comparison.

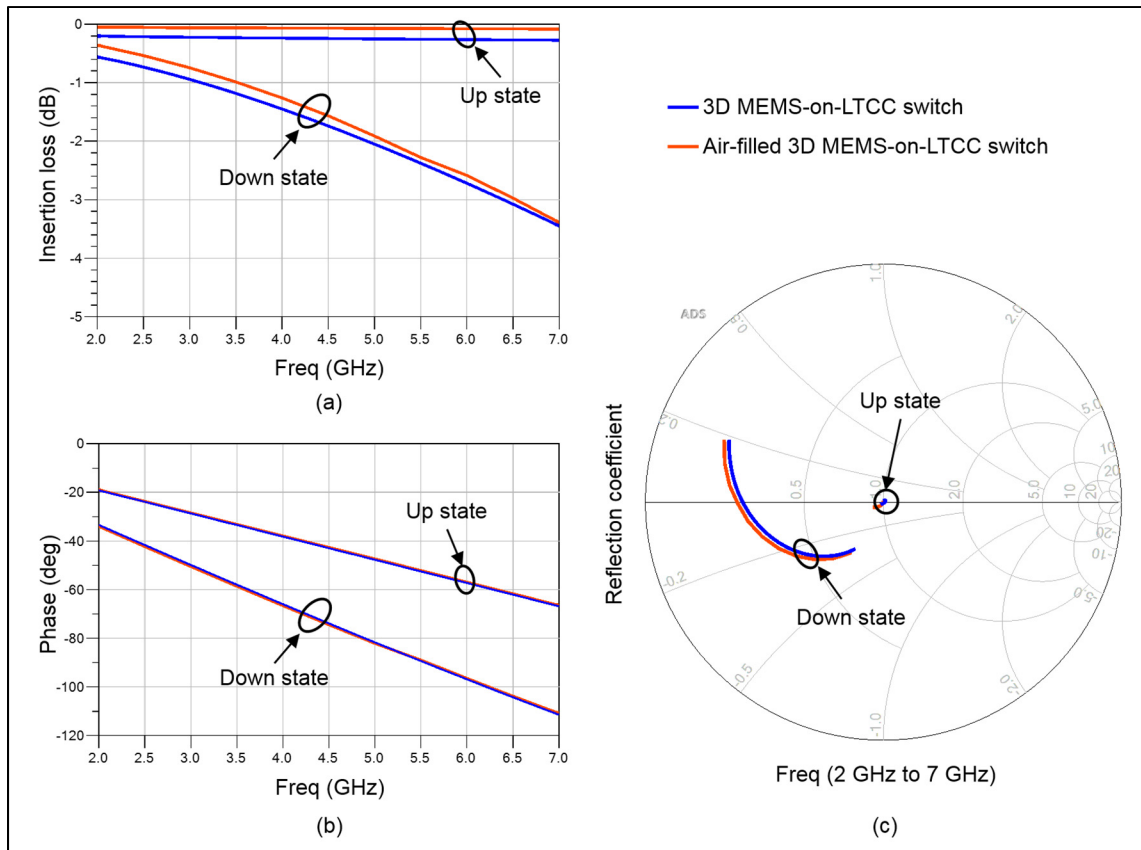


Figure 6.8 Field simulation of the dielectric-filled and air-filled 3D MEMS-on-LTCC switches: a) insertion loss, b) phase shift and c) reflection coefficient

Similarly to the 3D MEMS-on-LTCC tuner, eight cells were duplicated to form the air-filled tuner as shown in figure 6.9. Two transitions to the upper coplanar layer were added in the input and the output. The overall tuner size is $23.42 \text{ mm} \times 5 \text{ mm} \times 1.19 \text{ mm}$. Although transmission lines routing was difficult due to the significantly large width of the air-filled stripline, further iterations where the final tuner size is reduced without performance degradation are possible.

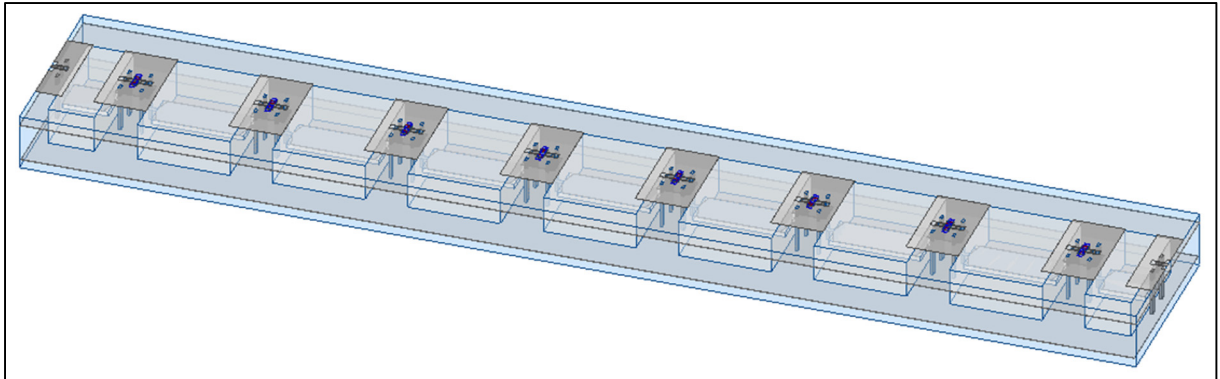


Figure 6.9 Air-filled 3D MEMS-on-LTCC tuner

Figure 6.10 shows a superposition of the air-filled and dielectric-filled 3D MEMS-on-LTCC tuners' simulated impedance coverages at six different frequencies in the [2 GHz-7 GHz] frequency range. The 256 impedances generated by the air filled based tuner at each frequency have generally higher gamma values. Indeed, maximum gamma (T) circles provided by the air-filled and the dielectric filled tuners were also added in figure 6.10 (orange and blue circles respectively). As it can be seen, all blue circles are included in the orange ones, proving thus a wider spread coverage for the air-filled tuner.

Certainly, the gain is not important if we consider low level matchings (for example -10 dB). However, for applications where an exact impedance value is required, air filled structure may be of a great interest. Fabricating such tuner in this case is beneficial. Unfortunately, it cannot be processed using the ordinary LTCC process described in chapter 4 as it doesn't allow the formation of closed thick cavities. However, such structures can be fabricated using the sandwich technique, i.e., assembly of two LTCC parts with open cavities. This requires several experiments to gather the two parts while ensuring good alignment.

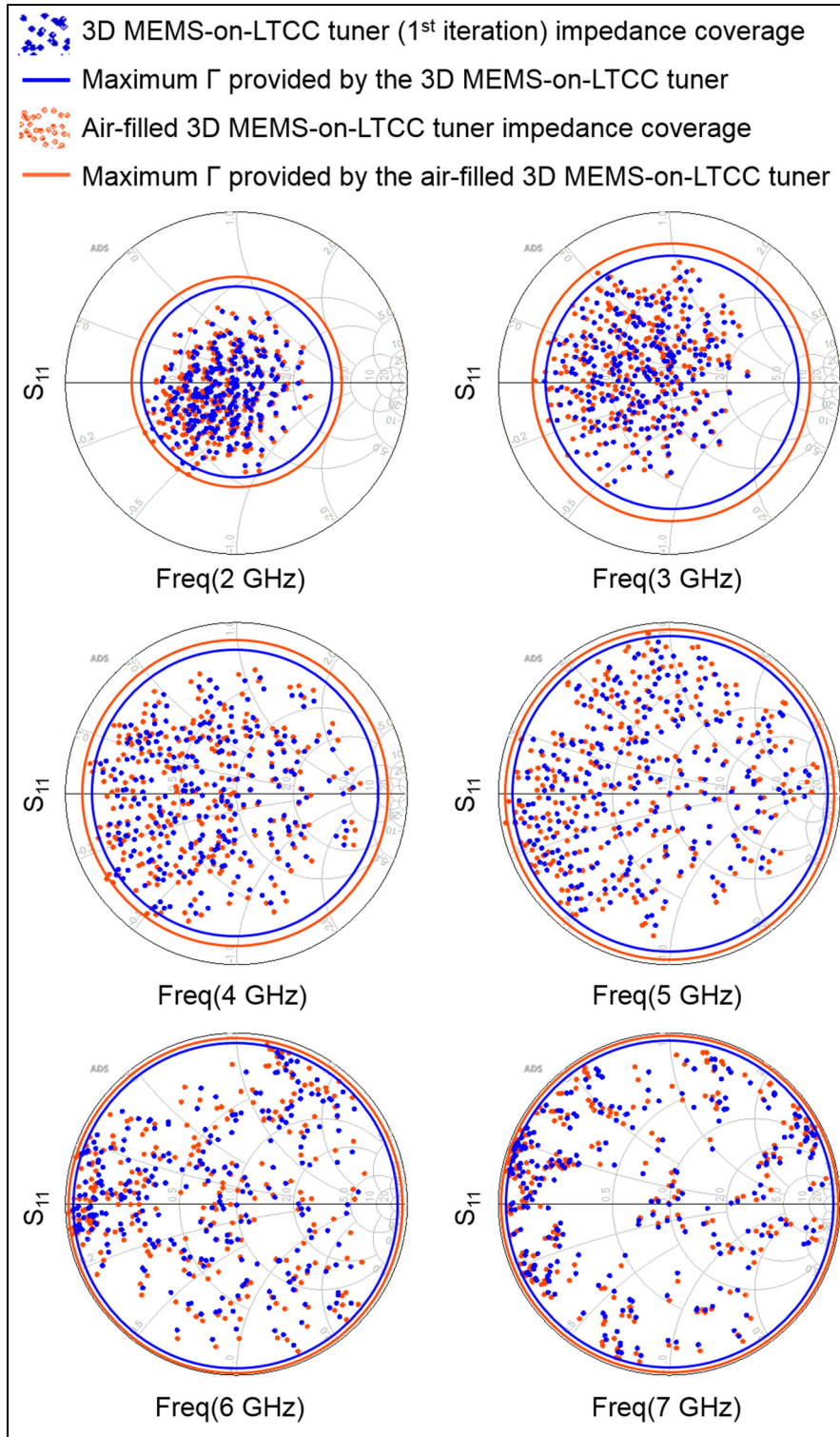


Figure 6.10 Air-filled and dielectric-filled 3DMEMS-on-LTCC tuners simulated Smith chart coverage and maximum Γ at different frequencies between 2 GHz and 7 GHz

6.3 LTCC based liquid metal RF tuner

A dielectric fluidic based RF tuner with good Smith chart coverage from 0.9 GHz to 2.2 GHz has been introduced in chapter 3. However, as explained, this tuner is not recommended to be used at higher frequencies since DI-water, the fluid used to fill the cavities, has higher loss as frequency goes higher. In fact, based on equation 3.13, its loss tangent varies from 0.13 to 0.38 between 2.4 GHz and 7 GHz under ambient temperature. In this case, the gain obtained through providing the required impedance to a particular device may not be reached due to such losses. Most dielectric liquids are known to have high loss tangents at RF and microwave frequencies due to the ions mobility and interactions (Warnagiris & Antonio, 2000). They have either low dielectric constants and/or high losses (Gabriel, Gabriel, Grant, Halstead, & P.Mingos, 1998). Therefore, they are not suitable to be used in our LTCC tuner. Recently, liquid metals with good electrical conductivity and remodeling capability have gained attention in the RF field (Bo, Ren, Xu, Du, & Dou, 2018; Watson et al., 2019) and seems to be good candidates as filling liquid of our LTCC tuner.

6.3.1 Liquid metal choice

Metals are abundant materials on earth. Most of them are present in solid state at room temperature. Only few metals are liquids under ambient temperature. Francium (Fr), caesium (Cs), rubidium (Rb), mercury (Hg) and gallium (Ga) based metals are the only known liquid metals (Bo et al., 2018). Cs, Fr, Rb and Hg can not be manipulated easily and should be used under extremely controlled conditions due to their radioactivity, instability or toxicity. Ga is a risk free metal, but it melts at 29.7 °C, which is slightly higher than room temperature. However, the melting points of Ga-alloys based metals such as EGaIn (Ga–In), EGaSn (Ga–Sn) and galinstan (Ga–In–Sn) are lower and they are around 15 °C, 21°C and –19 °C respectively (S. Liu, Sweatman, McDonald, & Nogita1, 2018). Characterised with its attractive electrical properties (conductivity: $3.46 \cdot 10^6$ s/m), large temperature operating range (melting point: –19 °C, boiling point: 2000 °C), commercial availability, low cost and scientific

community recent interest, we picked galinstan as eutectic metal filling the cavities of the LTCC RF tuner instead of DI- water.

6.3.2 Liquid metal RF cell

Here, we introduce a minor change in the design of the fluidic RF cell shown in figure 3.2-a. We simply added a thin dielectric layer (green color) between the coplanar plane and the cavity as depicted in figures 6.11-a and b. This way, we prevent contact between the coplanar plane and the metal filling the cavity, avoiding thereby a short circuit.

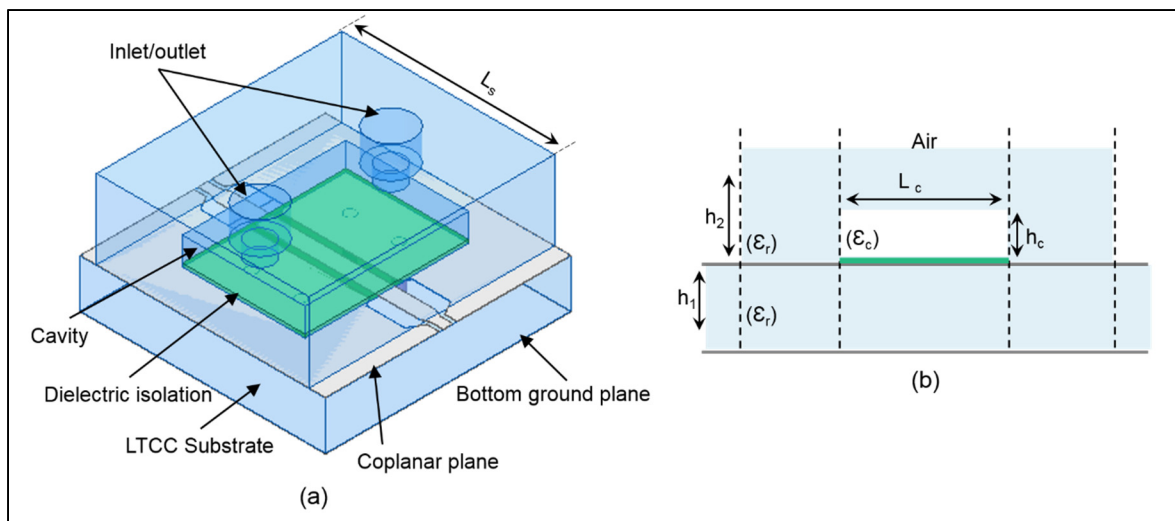


Figure 6.11 Two-state RF liquid metal cell: a) 3D view and b) cross section view

We kept the physical dimensions of the RF dielectric fluid cell and we used a 2-mil DuPont951 sheet as a protection layer. Therefore, if the cavity is empty, the cell presents a 50Ω impedance as the effect of the thin protection layer in the variation of the characteristic impedances is minimum. If galinstan is injected into the cavity, S3 presents a low impedance transmission line. Figure 6.11 shows the insertion loss and the complex reflection coefficient of this structure resulting from HFSS 3D field simulation between 2 GHz and 7 GHz for both states. While the empty cell is perfectly matched to 50Ω , the galinstan full cavity cell shows a variation of the reflection coefficient.

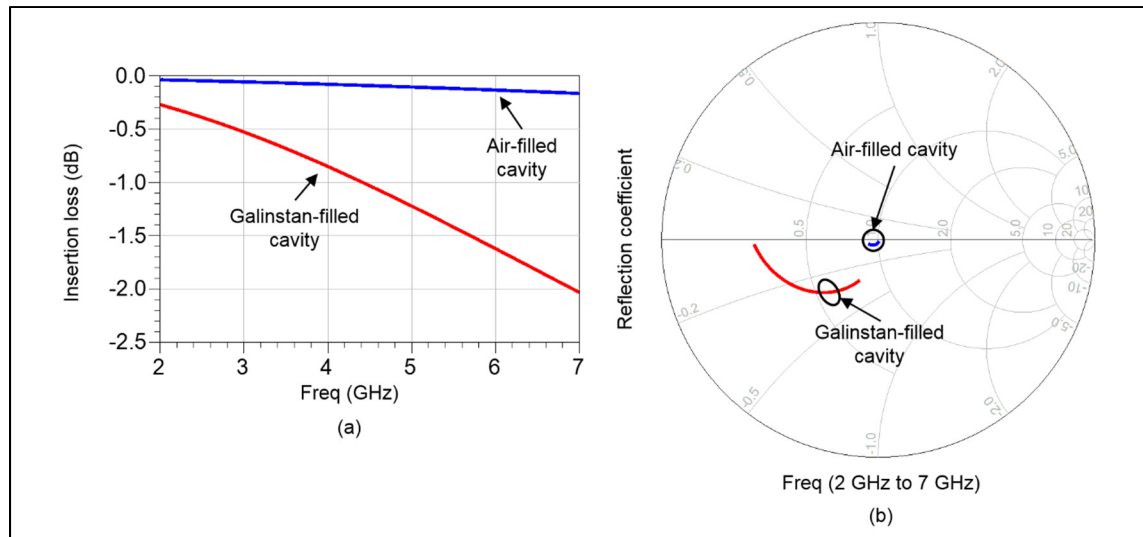


Figure 6.12 RF liquid metal cell simulated: a) Insertion loss and b) reflection coefficient

6.3.3 Liquid metal RF tuner

Similarly to the dielectric fluidic tuner, eight liquid metal cells were cascaded as shown in figure 6.13. Two $50\ \Omega$ vertical CPW transitions to upper CPWG lines were also added at the input and output for interconnection and measurement purpose. The final tuner has the same dimension as the fluidic one, i.e., $26\ \text{mm} \times 10\ \text{mm} \times 1.5\ \text{mm}$.

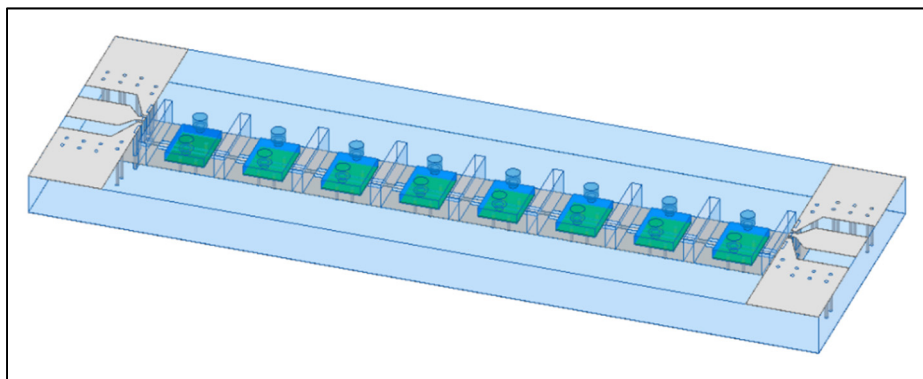


Figure 6.13 Liquid metal tuner 3D view

Figure 6.14 shows the obtained Smith chart coverage when the output port is terminated by a $50\ \Omega$ load. Good impedance distributions are obtained at different frequency points in the frequency range [2GHz, 7 GHz], particularly at higher frequencies. Like the fluidic and the

MEMS based RF tuners, a well distributed and uniform coverage cannot be obtained for all the frequencies for the same reasons discussed above (frequency dependant impedances and lengths).

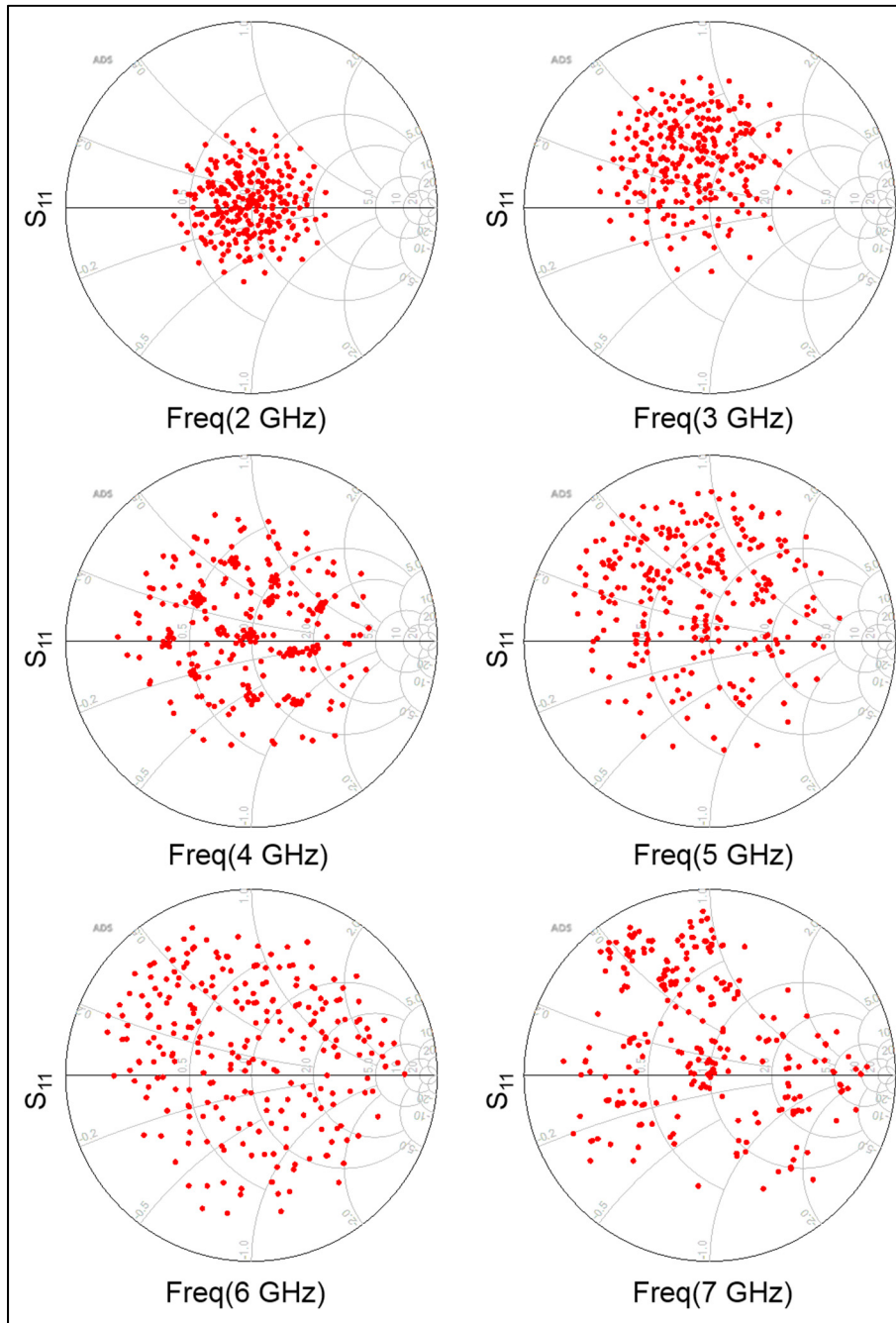


Figure 6.14 Liquid metal tuner simulated Smith chart coverage at different frequencies between 2 GHz and 7 GHz

Aside from its exceptional electrical and physical characteristics, which may offer such good RF tuner coverage, manipulation of galinstan is challenging (Watson et al., 2019). It is known as a gluey liquid that may sticks to most materials, including probably LTCC. Moreover, its exposure to air leads to the formation of an oxide layer on the surface, changing thereby its electrical characteristics. Consequently, a deep investigation about the experimental handling (condition, environment, procedure, etc.) of this metal is required if one want to take advantage from its benefits.

6.4 LTCC based RF tuners adaptive control

In this project, as we sought to prove the concept of reconfigurable amplifiers, we were limited to manual manipulation for both fluidic and MEMS based tuners and RF amplifiers, i.e., manual fluid injection/extraction and manual polarisation respectively. To be exploited in real circuits, this should be automated. Here, we propose a model for a smart RF amplifier (figure 6.15). It is composed of the transistor, biasing and stability circuits, tuners, sensing and control modules and input and output ports. At each iteration, the control module interrogates the sensing module to measure and calculate the transistor input and output gammas. Then, for a particular figure of merit (FOM) (frequency, gain, power, efficiency, etc.) and based on a smart algorithm, the control module calculates the adequate source and load impedances, search for the closest impedances provided by the tuner, and activates the correspondent tuners' cells.

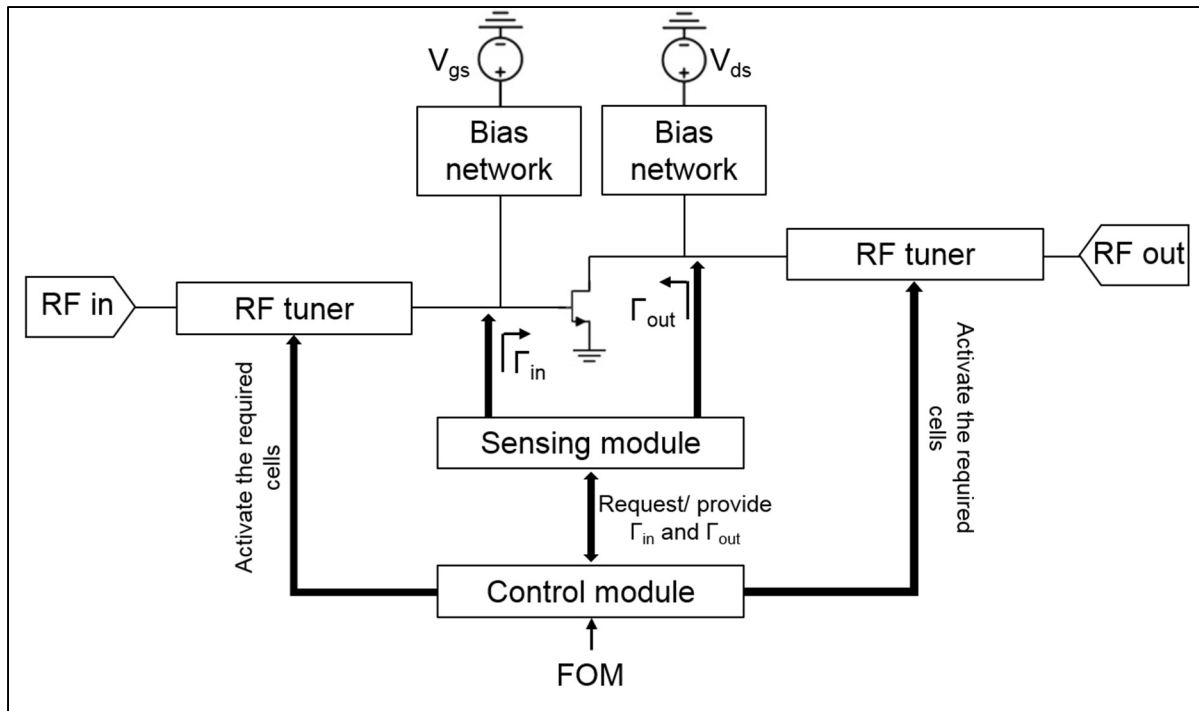


Figure 6.15 RF amplifier smart model

6.4.1 Sensing module

As indicated in the previous section, a non-destructive embedded structure is required to measure the transistor's input and output impedances. Mohamed et Kouki (2019) proposed an in-situ vector measurement structure and technique. It is formed basically from non-directional sniffers which can be built inside the LTCC substrate at the appropriate location to measure the complex reflection coefficients. In our case they can be placed under the transistor input and output. They can sample the transmitted and forwarded waves with little to no impact on the signal. This way, the gammas can be determined easily without the need of external equipment or connections. This tool can be used for both fluidic and MEMS circuits.

6.4.2 Control modules

Two computer-controlled modules shown in figure 6.16 and figure 6.17 were designed to manage the operation of the fluidic and the MEMS tuners respectively. They are formed from

a microcontroller and a fluid dispensing sub-module or a DC voltage supply sub-module. The microcontroller communicates with the sensing module, performs the required calculation and manages the operation of the sub-modules.

6.4.2.1 Fluid dispensing sub-module

The role of the fluidic dispensing sub-module is to inject/extract liquids to/ from the fluidic cavities. It was realized based on in-house 3D printed plastic block, where inner channels are connected through commercial solenoid electro-pumps and electro-valves (figure 6.16). If activated through a DC control circuit, injecting and extracting pumps allow spreading the fluid (DI-water) between the tank and the valves' input ports. Then, depending on the activated pump, precise liquids amounts may be circulated between the independently controlled valves and the corresponding RF circuit's cavities through thin metallic tubes. Therefore, this module allows filling or extracting the desired RF fluidic circuit cavities by a simple algorithm. This module was already fabricated and an algorithm controlling the fluid dispensing sub-module was developed. For a fully automated operation, a smart algorithm enabling the communication between the different modules should be implemented.

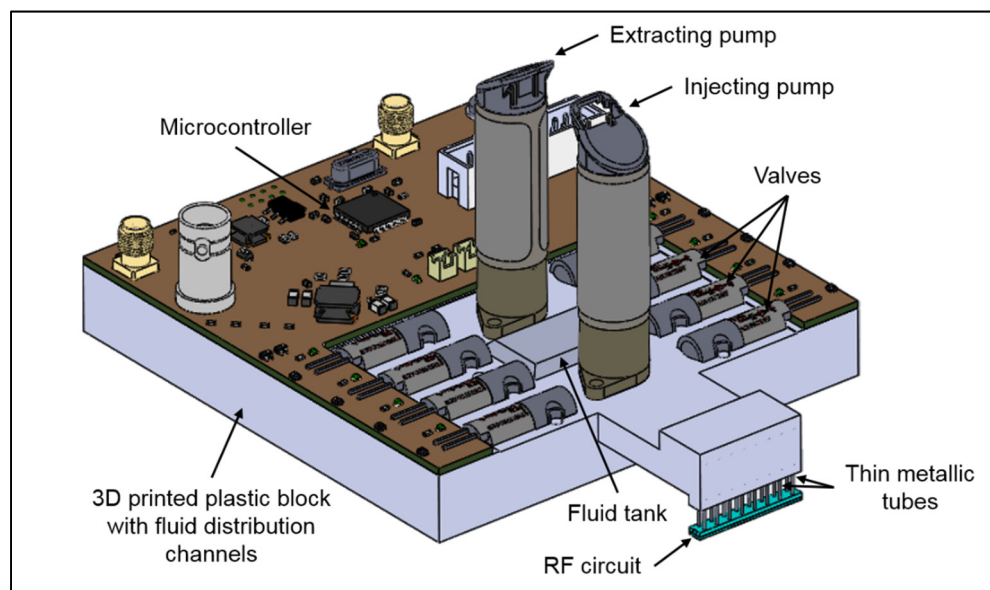


Figure 6.16 Fluidic circuits control module 3 D view

6.4.2.2 DC voltages supply sub-module

The DC voltage supply sub-module provides eight identical DC voltage supplies if connected to a DC voltage source as shown in figure 6.17. A reference was also added for verification purpose. DC circuits (potentiometer, capacitances and resistances) were added to bring the voltage in the required range i.e., around the biasing voltage of the MEMS-on-LTCC switch. All the voltage supplies are controlled through the microcontroller, enabling thus the activation of the required tuner's switches. This module was also fabricated and it is ready to deliver up to eight independent DC sources. Communication and control algorithms with the other modules still need to be developed.

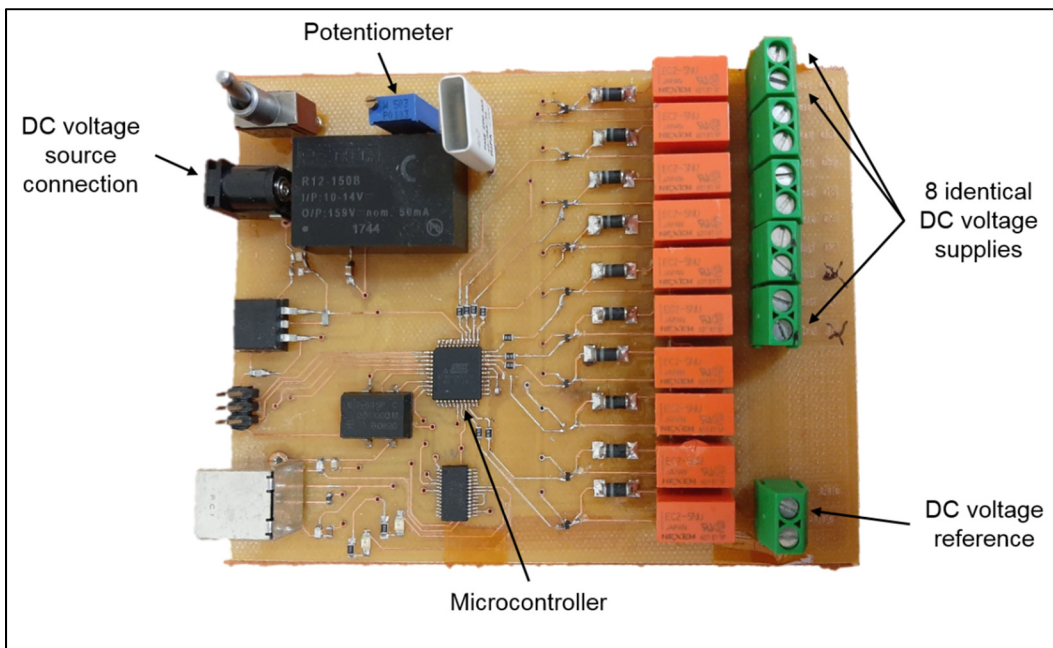


Figure 6.17 MEMS circuits' fabricated control module

6.5 Conclusion

Losses and manual manipulation are among the concerns that we would like to avoid in the exploitation of the tuners and reconfigurable RF circuits that we proposed. In fact, while losses lead to a shrunk coverage or prevent the operation at some frequencies, manual manipulation limits the potential of the proposed circuits. Loss reduction solutions as the integration of air-

filled transmission lines or the use of liquid metals have been proposed and studied. Designs and simulations were performed and demonstrated potential performance improvement. Modules for automated smart manipulation of the reconfigurable RF circuits have been also proposed. Further experimental investigations and algorithm implementation are required for the realisation of such findings.

CONCLUSION AND RECOMMENDATIONS

We are moving toward a fully connected world where communication systems, homes and cars are intelligently manipulated and controlled. Efficiency, miniaturisation, and cost reduction are therefore among the key challenges for future RF chains. Reconfigurability of RF products can help meet these challenges but is still an emerging research field. In this thesis, we proposed novel frequency reconfigurable impedance matching networks developed using LTCC technology where we integrated fluidic or MEMS elements and demonstrated their potential for enabling reconfigurability of low and high frequency circuits.

In the first part, we reviewed the works done in the scope of this project. We were interested basically to four parts: frequency reconfigurable RF amplifiers, reconfigurable impedance matching networks, MEMS-on-LTCC substrates and low loss guiding structures.

In the second part of this research, we studied the LTCC features as a fabrication technology. We focused on its potential to be combined with other technologies, like fluidics and MEMS, to produce reconfigurable RF circuits. We ensured, thereafter, its capability to be employed as a 3D substrate in our work to make novel RF impedance tuners and reconfigurable amplifiers.

In the third part, we proposed an approach to build RF impedance tuners in LTCC technology based on a periodic arrangement of 8 identical cells. Then, using this architecture, we developed two types of impedance tuners: coplanar waveguide structures combined (i) with air/ DI water fillable cavities and (ii) RF MEMS switches. Closed form equations for impedances and effective dielectric constants calculation for single cells, i.e., fluidic and MEMS based cells, were derived and used in the tuners' design. High changes in impedances and electrical lengths, of the fluidic and MEMS based cells were achieved even at low microwave frequencies, thanks to the constraint-free cells' physical lengths, offered by LTCC technology. Indeed, HFSS and ADS co-simulation demonstrated good coverage of the Smith chart below 2.4 GHz and 7 GHz for the fluidic and MEMS tuners, respectively. Leveraging LTCC 3D capability, 3D miniaturised MEMS-on- LTCC tuners were also proposed.

The fourth part introduced the development procedure of the MEMS-on-LTCC process, required for the manufacturing of the MEMS based circuits. An overview about the various steps and the used materials were first introduced. The most important challenges encountered during the process development were enumerated. Then, as application, we proposed a capacitive RF MEMS-on-LTCC switch: electromechanical analysis was detailed and fabrication steps were performed. Here, further fabrication iterations are recommended for characterisation purposes.

In the fifth part, we focused on the measurement of the fabricated fluidic circuits. Using custom measurement setups, measured results of the single cell and the impedance tuner were found to be close to the simulations results and a good impedance coverage was obtained between 0.9GHz and 2.4 GHz. Then, the fluidic and MEMS based tuners were used to demonstrate the reconfigurability of RF amplifiers in a single integrated design using only one LTCC substrate.

In the last part, we proposed methods to improve the performance of the presented RF tuners. For instance, we demonstrated that the integration of air-filled striplines in the MEMS-on-LTCC tuner may widen the Smith chart coverage. As for the fluidic tuner, we showed that the use of liquid metal instead of DI-water offers higher frequency coverage as dielectric losses are suppressed. We also proposed a schematic for an automatic control of the RF tuners when they are integrated in an RF amplifier design. Here, we concluded that the manual manipulation was hard and we suggested the use of sensing and control modules for both fluidic and MEMS solutions.

To pursue this work, we propose two different axes: some current issues can be addressed and further development and integration can be performed. Mainly, as future work to extend this thesis, we can define the following research opportunities:

- The improvement of the MEMS-on-LTCC process. Here, further fabrication iterations are required to obtain functional switches. Subsequently, circuits' parameters (design, layers

- thicknesses, etc.) may be altered to optimize the overall performance as increasing the power handling, decreasing the switching time and reducing the biasing voltage;
- The development of impedance tuners with novel algorithms offering wider coverages. For instance, we aim to synthesize uniformly spread impedances with less limits on the Smith chart edge at any target frequency. To do so, we may consider combining the fluidic and the MEMS technologies in a single tuner design. We may also think about novel distributions of the reconfigurable elements like a matrix configuration where each element is activated through a well-defined algorithm to perform a specific movement in the Smith chart;
 - The integration of the impedance tuners in an automated single fabrication bloc. This bloc would contain the frequency reconfigurable RF components (RF amplifier) with the tuners, the sensing and the control modules. Here, a single fabrication run should be made and sensing and control algorithms have to be developed.

JOURNAL AND CONFERENCES ARTICLES

Bahloul, D., Ben Amar, A., & Kouki, A.B. (2016). MEMS fabrication on LTCC substrates for RF applications : challenges and perspectives. *12th International conference and exhibition on ceramic interconnect and ceramic microsystems technologies (CICMT)*, 89-94.

Bahloul, D., & Kouki, A. B. (2019). Low loss air-filled transmission lines in LTCC technology. *IEEE Canadian Conference of Electrical and Computer Engineering (CCECE)*, 1-4.

Bahloul, D., & Kouki, A.B. (2020). LTCC-based fluidic tuners for low microwave frequency reconfigurable circuits. *IEEE Transaction and Microwave Theory and Techniques*, 60(8).

Ben Amor, I., Bahloul, D., & Kouki, A. B. Liquid metal investigation for LTCC based reconfigurable impedance tuner. To be submitted to *IEEE Microwave and Wireless Components Letters*.

Bahloul, D., Ben Amor, I., & Kouki, A. B. MEMS-on-LTCC process development for RF applications. To be submitted to *Microsystem Technologies*.

Bahloul, D., & Kouki, A. B. MEMS-on-LTCC reconfigurable RF matching networks for adaptive circuits. To be submitted to *IEEE Transaction and Microwave Theory and Techniques*.

APPENDIX I

ADS SCHEMATIC FOR RF TUNERS SIMULATIONS

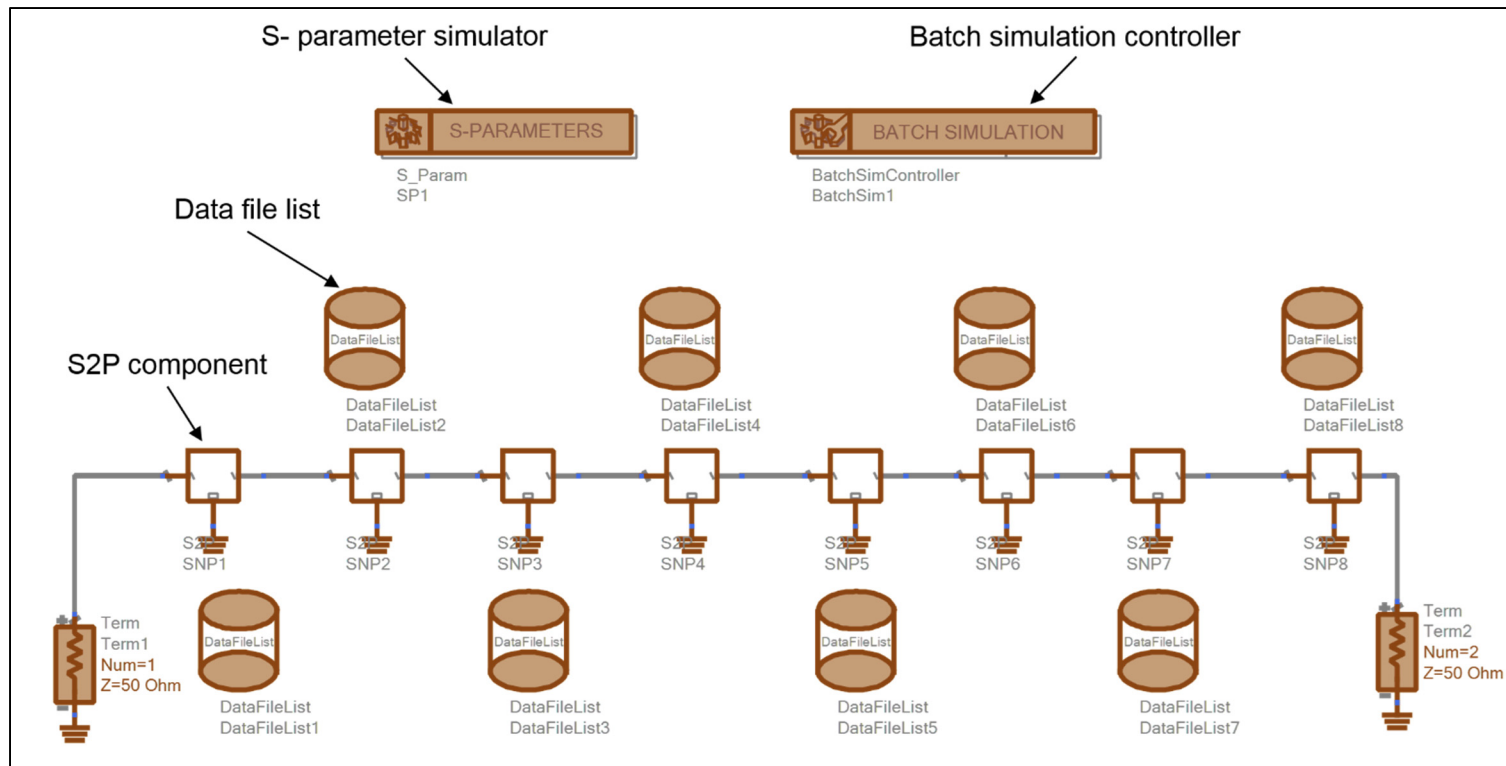


Figure-A I- 1 ADS schematic for RF tuners simulation

- **S2P component:** refer to Data File List

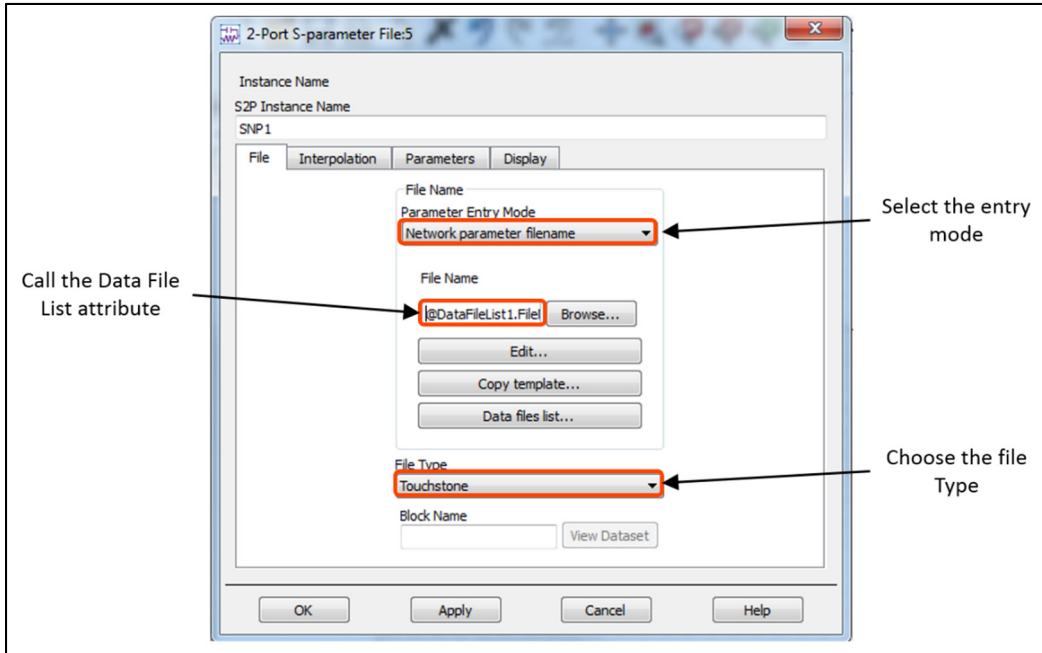


Figure-A I- 2 S2P component parameters

- **Data File List:** access to the s2p files containing the S-parameters of the reconfigurable cell's states simulated with HFSS

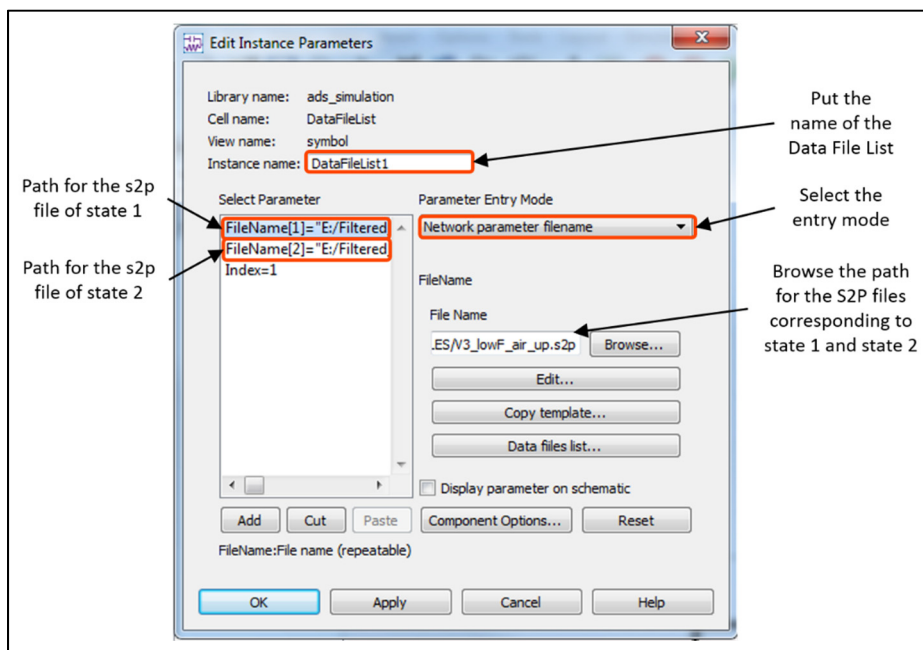


Figure-A I- 3 Data File List parameters

- **Batch simulation controller:** Sweep the states for all the Data File Lists

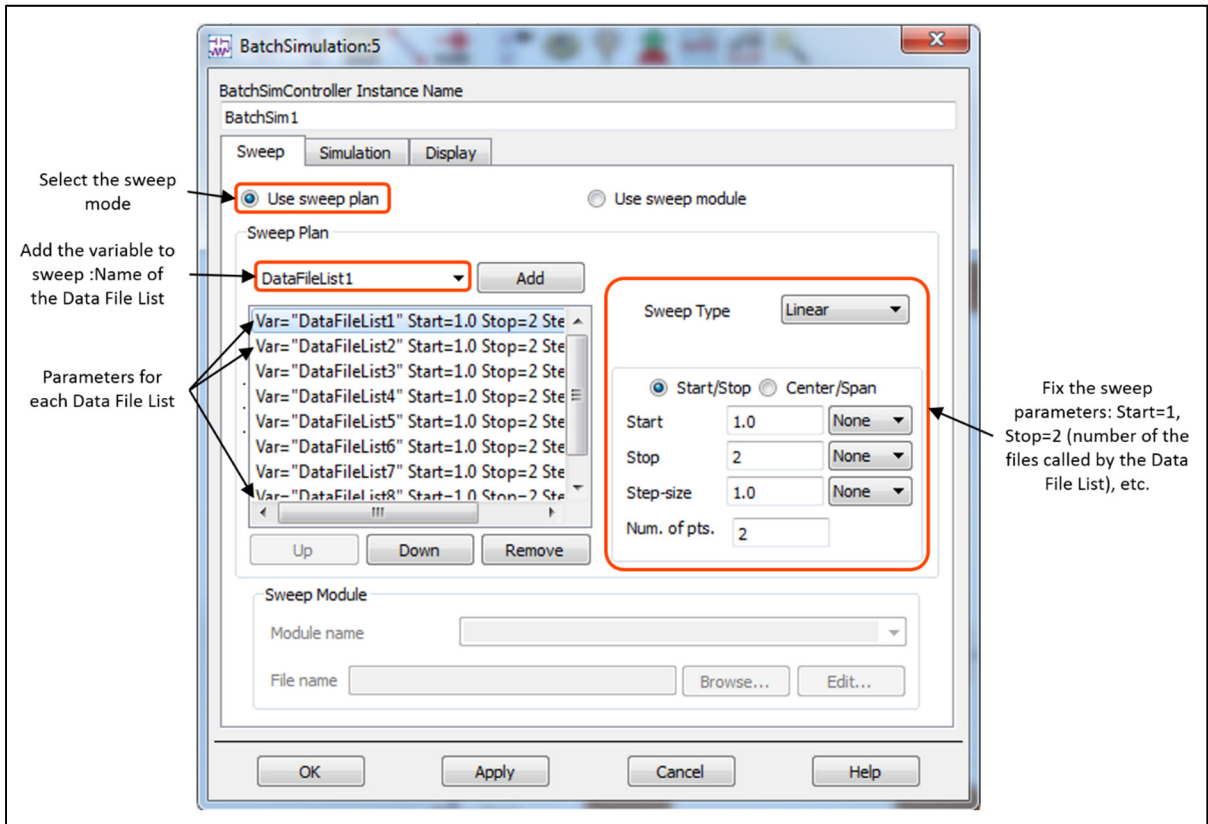


Figure-A I- 4 Batch simulation controller configuration

APPENDIX II

MEMS-ON-LTCC PROCESS

Table-A II- 1 Repetitive steps

| | |
|---|--|
| <p>LTCC surface polishing</p> <p>System: CMP: BT-380C:</p> <ul style="list-style-type: none"> • Polishing pad • Slurry Ultra-Sol Diamond • Slurry Ultra-sol 556 Colloidal Silica | <p>Substrate cleaning</p> <ul style="list-style-type: none"> • Acetone: 5 min/ ultrasonic bath • Iso-propanol: 5 min/ ultrasonic bath • DI water: 5 min/ ultrasonic bath • Hot plate: 5 min/150 oC |
| <p>Photoresist (AZ 5214E-IR) positive patterning</p> <p>Spin Coating:</p> <ul style="list-style-type: none"> • Step1: 300 rpm/ 3 s • Step2: 1000rpm/ 20s <p>Soft bake:</p> <ul style="list-style-type: none"> • Hot plate:1 min/ 100 °C <p>Soft mask exposure:</p> <ul style="list-style-type: none"> • System: Intelligent Micro patterning SF100 • Lens: 4X • UV wavelength: 365 nm • Focus: -250 μm • Time: 3s <p>Development:</p> <ul style="list-style-type: none"> • Developer: AZ 726 MIF • Time: 1 min | <p>Photoresist (AZ 5214E-IR) negative patterning (image reversal)</p> <p>Spin Coating:</p> <ul style="list-style-type: none"> • Step1: 300 rpm/ 3 s • Step2: 1000rpm/ 20s <p>Soft bake: Hot plate:1 min/ 100 °C</p> <p>Soft mask exposure:</p> <ul style="list-style-type: none"> • System: Intelligent Micro patterning SF100 • Lens: 4X • Filter:10X • UV wavelength: 365 nm • Focus: -250 μm • Time: 5s <p>Soft bake: Hot plate:2 min/ 120 °C</p> <p>Flood exposure:</p> <ul style="list-style-type: none"> • System: OAI 800MBA • Without mask • UV light • Power: 500W • Time: 4 min <p>Development:</p> <ul style="list-style-type: none"> • Developer: AZ 726 MIF • Time: 1 min |
| <p>Al DC sputtering</p> <p>System: Plasmionique SPT-330H:</p> <ul style="list-style-type: none"> • Pressure: 10 mtorr • Ar flow: 25 sccm • Rate: 8 nm/min | |

Table-A II- 1 Repetitive steps (continued)

| | |
|---|---|
| <p>Al etching</p> <p>Al etchant:</p> <ul style="list-style-type: none"> • Temperature: 45°C • Rate: 100 nm/min | <p>SiO₂ RF sputtering</p> <p>System: Plasmionique SPT-330H:</p> <ul style="list-style-type: none"> • RF Power: 200 W • Pressure: 10 mtorr • Ar flow: 25 sccm • Rate: 9 nm/min |
| <p>Cr DC sputtering</p> <p>System: Plasmionique SPT-330H:</p> <ul style="list-style-type: none"> • DC Power: 200 W • Pressure: 10 mtorr • Ar flow: 25 sccm • Rate: 14 nm/min | <p>SiO₂ anisotropic etching</p> <p>System: IBE: Intelvac Nanoquest I:</p> <ul style="list-style-type: none"> • Initialisation: O₂ flow: 5 sccm; Ar flow :25 sccm; LFN Ar flow: 10 sccm; LFN current: 2 A; Power: 250 W; Warmup: 2min • Etching: beam voltage: 400V; Beam current: 150 mA; Acceleration voltage: 60 V; Emission current: 0.2 A; O₂ flow : 5 sccm; Ar flow :25 sccm; stage angle: 90 deg • Rate: 12 nm/min |
| <p>Cr etching</p> <p>Cr etchant:</p> <ul style="list-style-type: none"> • Temperature: 45°C • Rate: 50 nm/min | <p>Polyimide (PI-2545) coating</p> <p>Spin Coating:</p> <ul style="list-style-type: none"> • Step1: 500 rpm/ 5 s • Step2: 4000 rpm/ 40s <p>Soft bake:</p> <ul style="list-style-type: none"> • Hot plate:4 min/ 140 °C |
| <p>Photoresist stripping 1</p> <p>Stripper: AZ 400T</p> | |
| <p>Photoresist stripping 2</p> <p>Stripper: Remover 1162</p> <p>Time: 20 s</p> | |
| <p>Critical Point Dryer</p> <p>System: Autosamdri-815B</p> | |

Table-A II- 2 Process

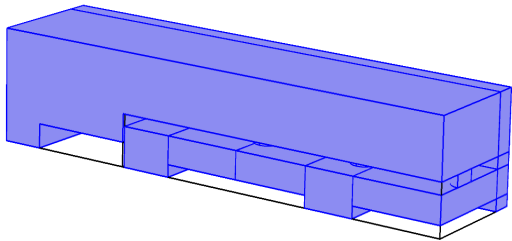
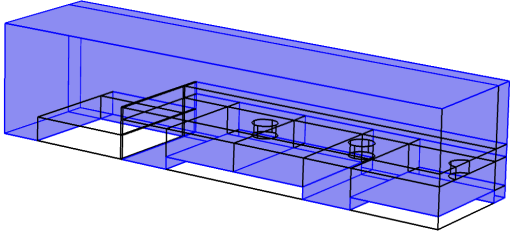
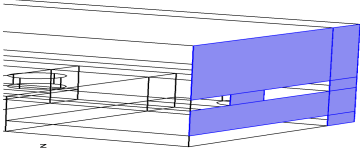
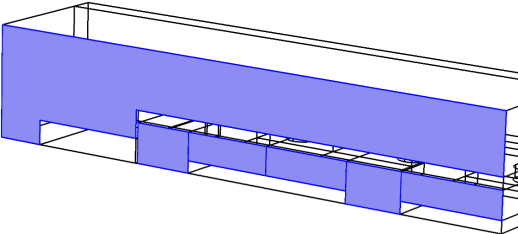
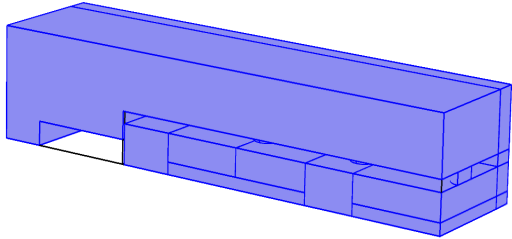
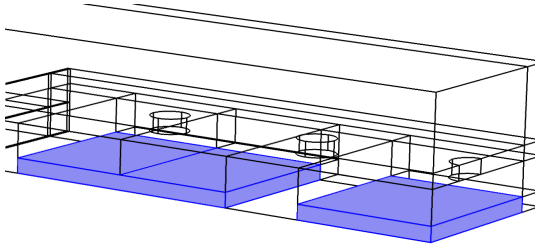
| | |
|--|--|
| <ol style="list-style-type: none"> 1. Masks generation 2. LTCC surface polishing 3. Substrate cleaning 4. Photoresist (AZ 5214E-IR) negative patterning (image reversal) 5. Al DC sputtering: <ul style="list-style-type: none"> • Time: 2 h • Thickness: 1 μm 6. Photoresist stripping 1 <ul style="list-style-type: none"> • Temperature: room temperature 7. Substrate cleaning 8. SiO₂ RF sputtering: <ul style="list-style-type: none"> • Time: 40 min • Thickness: 350 nm 9. Photoresist (AZ 5214E-IR) positive patterning 10. SiO₂ anisotropic etching: <ul style="list-style-type: none"> • Time: 30 min 11. Photoresist stripping 1: <ul style="list-style-type: none"> • Temperature: 80 °C 12. Substrate cleaning 13. Photoresist (AZ 5214E-IR) negative patterning (image reversal) 14. Al DC sputtering: <ul style="list-style-type: none"> • Time: 2 h • Thickness: 1 μm 15. Photoresist stripping 1 <ul style="list-style-type: none"> • Temperature: room temperature 16. Substrate cleaning 17. SiO₂ RF sputtering: <ul style="list-style-type: none"> • Time: 40 min • Thickness: 350 nm | <ol style="list-style-type: none"> 18. Photoresist (AZ 5214E-IR) positive patterning 19. SiO₂ anisotropic etching: <ul style="list-style-type: none"> • Time: 30 min 20. Photoresist stripping 1: <ul style="list-style-type: none"> • Temperature: 80 °C 21. Polyimide (PI-2545) coating 22. Photoresist (AZ 5214E-IR) negative patterning (image reversal) 23. Photoresist stripping 2 24. Al DC sputtering: <ul style="list-style-type: none"> • Time: 30 min • Thickness: 250 nm 25. Photoresist (AZ 5214E-IR) negative patterning (image reversal) 26. Cr DC sputtering: <ul style="list-style-type: none"> • Time: 1 h • Thickness: 900 nm 27. Photoresist stripping 1 <ul style="list-style-type: none"> • Temperature: room temperature 28. Al etching <ul style="list-style-type: none"> • Time: 3 min 29. Photoresist stripping 2 <ul style="list-style-type: none"> • Temperature: 80 °C • Time: 30min 30. Photoresist stripping 2 <ul style="list-style-type: none"> • Temperature: room temperature • Time: more than 12h 31. Critical point dryer |
|--|--|

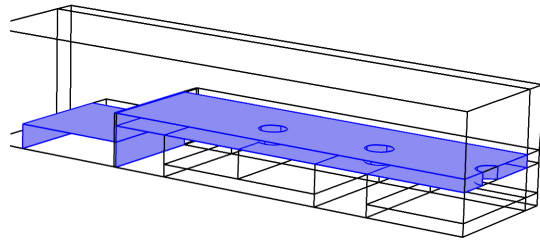
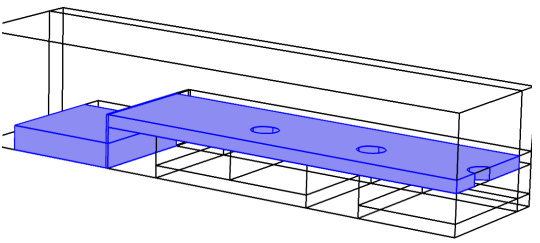
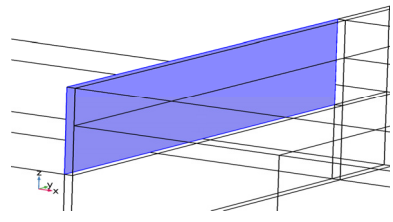
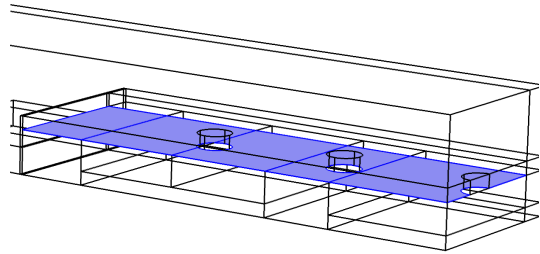
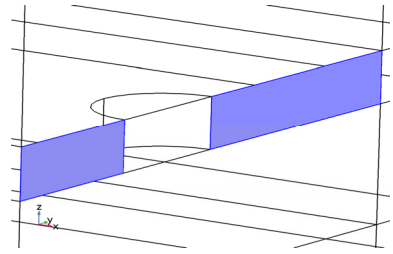
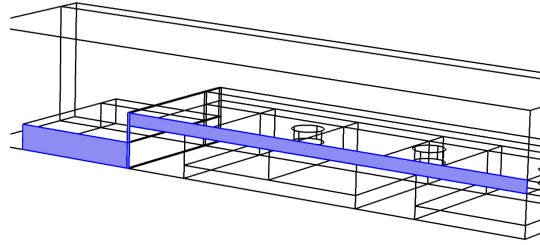
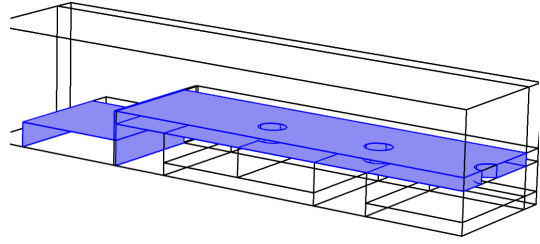
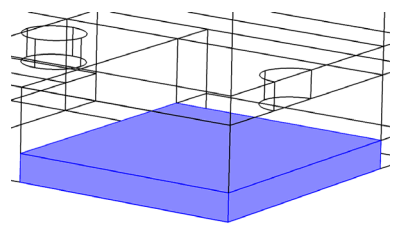
APPENDIX III

COMSOL SETUP

This appendix details the electro-mechanics boundaries used in the simulation of the MEMS switch with COMSOL Multiphysics. Only the structure quadrant is shown here.

Table-A III- 1 COMSOL electro-mechanics boundaries

| | |
|---|---|
| <ul style="list-style-type: none">• Free Deformation  | <p>Prescribed Mesh Displacement</p>    |
| <ul style="list-style-type: none">• Electrical Material Model  | <ul style="list-style-type: none">• Fixed Mesh  |

| | |
|---|---|
| <ul style="list-style-type: none">• Electromechanical Interface  | <ul style="list-style-type: none">• Linear Elastic Material  |
| <ul style="list-style-type: none">• Fixed Constraint  | <ul style="list-style-type: none">• Boundary Load  |
| <ul style="list-style-type: none">• Symmetry   | <ul style="list-style-type: none">• Terminal   |

BIBLIOGRAPHY

- Added, M., & Boulejfen, N. (2015). Variable impedance matching network based on varactor diodes. *IEEE 15th Mediterranean Microwave Symposium (MMS)*, 1-4.
- Al-masha'al, A., Mastropaolo, E., Bunting, A., Dunare, C., & Cheung, R. (2017). Fabrication and characterisation of suspended microstructures of tantalum. *Journal of Micromechanics and Microengineering*, 27, 1-9.
- Andryieuski, A., Kuznetsova, S. M., Zhukovsky, S. V., Kivshar, Y. S., & Lavrinenko, A. V. (2015). Water: promising opportunities for tunable all-dielectric electromagnetic metamaterials. *Scientific Reports*, 5.
- Bahloul, D., & Kouki, A. B. (2020). LTCC-based fluidic tuners for low microwave frequency reconfigurable circuits. *IEEE Transaction and Microwave Theory and Techniques*, 60(8).
- Bahloul, D., Ben Amar, A., & Kouki, A. B. (2016). MEMS fabrication on LTCC substrates for RF applications : challenges and perspectives. *12th International conference and exhibition on ceramic interconnect and ceramic microsystems technologies (CICMT)*, 89-94.
- Bahloul, D., & Kouki, A. B. (2019). Low loss air-filled transmission lines in LTCC technology. *IEEE Canadian Conference of Electrical and Computer Engineering (CCECE)*, 1-4.
- Belambri, N., Dubouil, D., Talbot, C., Kouki, A. B., & Gagnon, F. (2011). Design of a buried hybrid coupler for wideband applications using LTCC technology. *Canadian Conference on Electrical and Computer Engineering (CCECE)*.
- Bo, G., Ren, L., Xu, X., Du, Y., & Dou, S. (2018). Recent progress on liquid metals and their applications. *Advances in Physics: X*, 3(1), 412-442.
- Brown, M., Goode, I., & Saavedra, C. (2018). Lumped-element circuit modelling of microfluidic channels in microstrip transmission lines. *IEEE NEWCAS*, 1-5.
- Chen, K., & Peroulis, D. (2012). Design of adaptive highly efficient GaN power amplifier for octave-bandwidth application and dynamic load modulation. *IEEE Transactions on Microwave Theory and Techniques*, 60(6), 1829-1839.
- Chlieh, O. L., & Papapolymerou, J. (2017). Hybrid integrated microfluidic channels on multilayer organic substrate and on copper for tuning and cooling an RF reconfigurable S-/C-band GaN-based power amplifier. *IEEE Transactions on Microwave Theory and Techniques*, 65(1), 156-164.

- Chung, H.-W., Hsu, C.-Y., Yang, C.-Y., Wei, K.-F., & Chuang, H.-R. (2008). A 6-10-GHz CMOS power amplifier with an inter-stage wideband impedance transformer For UWB transmitters *38th European Microwave Conference*, 305-308.
- Cianci, E., Coppa, A., Foglietti, V., Dispenza, M., Buttiglione, R., Fiorello, A. M., . . . Pochesci, D. (2007). Fabrication of RF-MEMS switches on LTCC substrates using PECVD a-Si as sacrificial layer. *Microelectronic Engineering*, 84, 1401-1404.
- D'Auria, M., Sunday, A., Hazell, J., Robertson, I. D., & Lucyszyn, S. (2014). Enabling technology for ultralow-cost RF MEMS switches on LTCC. *ARMMS RF & Microwave Society Conference*.
- Deslandes, D., & Wu, K. (2006). Accurate modeling, wave mechanisms, and design considerations of a substrate integrated waveguide. *IEEE Transactions on Microwave Theory and Techniques*, 54(6), 2516-2526.
- Domingue, F., Fouladi, S., Kouki, A. B., & Mansour, R. R. (2009). Design Methodology and Optimization of Distributed MEMS Matching Networks for Low-Microwave-Frequency Applications. *IEEE Transactions on Microwave Theory and Techniques*, 57(12), 3030-3041.
- Domingue, F., Kouki, A. B., & Mansour, R. R. (2009). Tunable microwave amplifier using a compact MEMS impedance matching network. *Proceedings of the 39th European Microwave Conference*.
- Entesari, K., & Saghati, A. P. (2016). Fluidics in microwave components. *IEEE Microwave Magazine*, 17(6), 50-57.
- Franssila, S. (2010). *Introduction to microfabrication* (2nd éd.). Chichester, UK.
- Fukuda, A., Okazaki, H., & Narahashi, S. (2006). A novel compact reconfigurable quad-band power amplifier employing RF-MEMS switches *Proceedings of the 36th European Microwave Conference*, 344-347.
- Gabriel, C., Gabriel, S., Grant, E. H., Halstead, B. S. J., & P.Mingos, D. M. (1998). Dielectric parameters relevant to microwave dielectric heating. *Chemical Society Reviews*, 27, 213-223.
- Gough, R. C., Morishita, A. M., Dang, J. H., Hu, W., Shiroma, W. A., & Ohta, A. T. (2014). Continuous electrowetting of non-toxic liquid metal for RF applications. *IEEE Access*, 2, 874-882.
- Haghshenas, A., Ghobadi, C., Nourinia, J., Ahmadian, D., & Soltani, S. (2011). A novel approach in RF-MEMS switch analysis using time domain TLM method *Journal of Electromagnetic Analysis and Applications*, 3, 395-398.

- Hary, S., Barton, T., & Ebel, J. (2016). Reconfigurable RF components for multifunction RF systems. *IEEE Compound Semiconductor Integrated Circuit Symposium (CSICS)*.
- Heinen, S., & Wunderlich, R. (2011). High dynamic range RF frontends from multiband multistandard to Cognitive Radio. *Semiconductor Conference Dresden*, 1-8.
- Hsu, H. C., Wang, Z. W., & Ma, G. K. (2005). A low power CMOS full-band UWB power amplifier using wideband RLC matching Method. *IEEE Conference on Electron Devices and Solid-State Circuits*, 233-236.
- Isapour, A., & Kouki, A. B. (2017). Empty LTCC integrated waveguide with compact transitions for ultra-low loss millimeter-wave applications. *IEEE Microwave And Wireless Components Letters*, 27(2), 144-146.
- Jeong, I., Shin, S.-H., Go, J.-H., Lee, J.-S., Nam, C.-M., Kim, D.-W., & Kwon, Y.-S. (2002). High-performance air-gap transmission lines and inductors for millimeter-wave applications. *IEEE Transactions on Microwave Theory and Techniques*, 50(2), 2850-2855.
- Jondral, F. K. (2005). Software defined radio—basics and evolution to cognitive radio. *EURASIP Journal on Wireless Communications and Networking*, 3, 275-283.
- Khodor, H. R. (2013). *Packaging of microwave integrated circuits in LTCC technology* (Telecom Bretagne).
- Kim, H.-T., Jung, S., Kang, K., Jae-Hyoung Park, Kim, Y.-K., & Kwon, Y. (2001). Low-loss analog and digital micromachined impedance tuners at the Ka-band. *IEEE Transactions on Microwave Theory and Techniques*, 49(12), 2394-2400.
- Kim, H. J., Choi, J. K., Hong, M. K., Lee, K., & Ko, Y. (2012). Contact behavior and chemical mechanical polishing (CMP) performance of hole-type polishing pad. *ECS Journal of Solid State Science and Technology*, 1(4), 204-209.
- Lee, C.-H., Chang, J. J., Yang, K. S., An, K. H., Lee, I., Kim, K., . . . Kim, H. (2009). A highly efficient GSM/GPRS quad-band CMOS PA module. *IEEE Radio Frequency Integrated Circuits Symposium*, 229-232.
- Lee, M., & Lim, S. (2018). Planar inverted-F antenna (PIFA) using microfluidic impedance tuner. *Sensors*, 18(10), 1-9.
- Lei, B. J., Hu, W., Ohta, A. T., & Shiroma, W. A. (2012). A liquid-metal reconfigurable double-stub tuner. *IEEE MTT-S International Microwave Symposium Digest (MTT)*, 1-3.

- Liu, R., Schreurs, D., Raedt, W. D., Vanaverbeke, F., & Mertens, R. (2011). RF-MEMS based tri-band GaN power amplifier. *Electronics Letters*, 47(13), 762-763.
- Liu, S., Sweatman, K., McDonald, S., & Nogita, K. (2018). Ga-based alloys in microelectronic interconnects: a review. *Materials (Basel)*, 11(8).
- LTCC@ÉTS. (2018). LTCC@ÉTS process & Capabilities Repéré à <https://www.etsmtl.ca/Unites-de-recherche/LTCC/Services-offerts/processV2.pdf>
- Lucibello, A., Marcelli, R., Di Paola, E., Di Nardo, S., Pochesci, D., Croci, R., & Germani, C. (2018). Fabrication and test of RF MEMS in LTCC technology. *Microsystem Technologies*, 24(1), 511-518.
- Marcelli, R., Lucibello, A., Angelis, G. D., Proietti, E., & Comastri, D. (2010). Mechanical modelling of capacitive RF MEMS shunt switches. *Microsystem Technologies*, 16, 1057–1064.
- Marcelli, R., Lucibello, A., Lucibello, A., Angelis, G. D., Proietti, E., & Bartolucci, G. (2012). Dynamics of RF micro-mechanical capacitive shunt switches in coplanar waveguide configuration. Dans InTech (Éd.), *Microelectromechanical systems and devices* (pp. 193-232). New York.
- McClung, S. N., Saeedi, S., & Sigmarsson, H. H. (2018). Band-reconfigurable filter with liquid metal actuation. *IEEE Transaction and Microwave Theory and Techniques*, 66(6), 3073-3080.
- Mingo, J. d., Valdovinos, A., Crespo, A., Navarro, D., & García, P. (2004). An RF electronically controlled impedance tuning network design and its application to an antenna input impedance automatic matching system. *IEEE Transactions on Microwave Theory and Techniques*, 52(2), 489-497.
- Mohamed, H. S., & Kouki, A. B. (2019). 3D reflectometer design for embedded RF vector measurement. *92nd ARFTG Microwave Measurement Conference (ARFTG)*, 1-4.
- Morishita, A. M., Dang, J. H., Gough, R. C., Ohta, A. T., & Shiroma, W. A. (2015). A tunable amplifier using reconfigurable liquid-metal double-stub tuners. *Texas Symposium on Wireless and Microwave Circuits and Systems (WMCS)*.
- Murad, S. A. Z., Pokharel, R. K., Galal, A. I. A., Sapawi, R., Kanaya, H., & Yoshida, K. (2010). An excellent gain flatness 3.0–7.0 GHz CMOS PA for UWB applications. *IEEE Microwave And Wireless Components Letters*, 20(9), 510-512.
- Okazaki, H., Fukuda, A., & Nar, S. (2005). Band- reconfigurable high-efficiency power amplifier- 900MHz/ 1900 MHz dual band PA using MEMS switches *NTT DoCoMo Technical Journal*, 7, 11-18.

- Papapolymerou, J., Lange, K. L., Goldsmith, C. L., Malczewski, A., & Kleber, J. (2003). Reconfigurable double-stub tuners using MEMS switches for intelligent RF front-ends. *IEEE Transactions on Microwave Theory and Techniques*, 51(1).
- Pinon, S., Diedhiou, D. L., Gue, A.-M., Fabre, N., Prigent, G., Conedera, V., . . . Boukabache, A. (2012). Development of a microsystem based on a microfluidic network to tune and reconfigure RF circuits. *Journal of Micromechanics and Microengineering*, 22(7), 1-7.
- Pozar, D. M. (2012). *Microwave engineering*. John Wiley & Sons, Inc.
- Rao, K. S., Thalluri, L. N., Guha, K., & Sravani, K. G. (2018). Fabrication and characterization of capacitive RF MEMS perforated switch. *IEEE Access*, 6, 77519-77528.
- Rebeiz, G. M. (2004). *RF MEMS: theory, design, and technology*. Hoboken, New Jersey: John Wiley & Sons, Inc.
- Rodriguez, E. G. (2015). *Reconfigurable transceiver architecture for multiband RF-frontends* (Vol. 17). Berlin: Springer.
- Rodriguez, E. G., Maune, H., Shen, L., Shah, I. A., Dahlhaus, D., Hofmann, K., & Jakoby, R. (2013). Reconfigurable radio frontends for cooperative sensor networks: tasks and challenges. *14th Workshop on Signal Processing Advances in Wireless Communications (SPAWC)*, 515-519.
- Scheele, P., Goelden, F., Giere, A., Mueller, S., & Jakoby, R. (2005). Continuously tunable impedance matching network using ferroelectric varactors. *IEEE MTT-S International Microwave Symposium Digest*, 1-4.
- Simons, R. N. (2001). *Coplanar waveguide circuits, components, and systems*. John Wiley & Sons, Inc.
- Tang, H., & Chen, J.-X. (2017). Microfluidically frequency-reconfigurable microstrip patch antenna and array. *IEEE Access*, 5, 20470-20476.
- Teixeira, F. L., Radhakrishnan, K., & Chew, W. C. (2005). High-frequency transmission lines. Dans *Encyclopedia of RF and Microwave Engineering*. John Wiley & Sons, Inc.
- Vähä-Heikkilä, T., & Rebeiz, G. M. (2004). A 20–50 GHz reconfigurable matching network for power amplifier applications. *IEEE MTT-S International Microwave Symposium Digest (MTT)*, 717–721.

- Vähä-Heikkilä, T., Van Caekenberghe, K., Varis, J., Tuovinen, J., & Rebeiz, G. M. (2007). RF MEMS impedance tuners for 6–24 GHz applications. *International Journal of RF and Microwave Computer-Aided Engineering*, 17(3), 265-278.
- Vaha-Heikkila, T., Varis, J., Tuovinen, J., & Rebeiz, G. M. (2004). A reconfigurable 6-20 GHz RF MEMS impedance tuner. *2004 IEEE MTT-S International Microwave Symposium Digest*.
- Vanhille, K., Lukic, M., Rondineau, S., Filipovic, D., & Popovic, Z. (2007). Integrated micro-coaxial passive components for millimeter-wave antenna front ends. *4th, International conference on antennas, radar, and wave propagation*.
- Warnagiris, T. J., & Antonio, S. (2000). Liquid sensing at radio frequencies. *Microwave Journal*.
- Watson, A. M., Leary, T. F., Elassy, K. S., Mattamana, A. G., Rahman, M. A., Shiroma, W. A., . . . Tabor, C. E. (2019). Physically reconfigurable RF liquid electronics via Laplace barriers. *IEEE Transaction on Microwave Theory and Techniques*, 67(12), 4881-4889.
- Xiaoyu, M., Osamu, T., & Satoshi, U. (2010). MEMS tunable bandpass filters on high-k LTCC. *IEEE 23rd International Conference on Micro Electro Mechanical Systems (MEMS)*, 787 - 790.